

Electronic Theses and Dissertations

2016

Heat Transfer and Pressure Measurements from Jet Array Impingement onto a Large Radius Curved Surface

John Harrington
University of Central Florida

 Part of the [Mechanical Engineering Commons](#)
Find similar works at: <https://stars.library.ucf.edu/etd>
University of Central Florida Libraries <http://library.ucf.edu>

This Masters Thesis (Open Access) is brought to you for free and open access by STARS. It has been accepted for inclusion in Electronic Theses and Dissertations by an authorized administrator of STARS. For more information, please contact STARS@ucf.edu.

STARS Citation

Harrington, John, "Heat Transfer and Pressure Measurements from Jet Array Impingement onto a Large Radius Curved Surface" (2016). *Electronic Theses and Dissertations*. 5226.
<https://stars.library.ucf.edu/etd/5226>

HEAT TRANSFER AND PRESSURE MEASUREMENTS OF JET ARRAY IMPINGEMENT
ONTO A LARGE-RADIUS CURVED SURFACE

by

JOHN HARRINGTON
B.S. University of Central Florida, 2014

A thesis submitted in partial fulfilment of the requirements
for the degree of Master of Science
in the Department of Mechanical and Aerospace Engineering
in the College of Engineering and Computer Science
at the University of Central Florida
Orlando, Florida

Summer Term
2016

Major Professor: Jayanta Kapat

© 2016 John Harrington

ABSTRACT

This study investigates the heat transfer and pressure drop characteristics of jet array impingement in two distinct parts. In the first part, the performance of a uniform array of jets on both a flat and a large radius curved target surface are compared. This comparison was done at average jet Reynolds number ranging from 55,000 to 125,000. In the second part, the characteristics of a non-uniform array of jets, more typical of geometries used in actual gas turbine combustors, are investigated, including the effects of the removal of downstream rows and the placement of rib features onto the target surface. The non-uniform configurations studied have varying hole diameters and geometric spacing for spatial tuning of the heat transfer behavior. First row jet Reynolds numbers ranging from 50,000 to 160,000 are reported. For all configurations, spent air is drawn out in a single direction which is tangential to the target plate curvature. Alongside the experimental work, CFD simulations were performed utilizing the $v^2 - f$ eddy viscosity turbulence model.

The results from the uniform array impingement onto a curved surface comparison show that the large radius curvature of the current geometry has little to no effect on the flow distribution and heat transfer of the array.

The non-uniform array results illustrate the applicability of tuning a jet impingement array using varying jet diameters and spacing. However, there are some difficulties in obtaining streamwise pitch resolved heat transfer predictions for non-uniform arrays as current open literature correlations for uniform arrays are shown to be not applicable. The computational results from this study show that simulations can be used to obtain initial predictions, with streamwise pitch averaged Nu values found to be within 20% of experimental results. The use of ribs downstream in place of several jet rows was shown to yield similar heat transfer results at lower pressure drop levels.

This paper is dedicated to my family, including my wife Sharka, my brother Michael, and my parents, Bob and Teresa.

ACKNOWLEDGMENTS

I would like to acknowledge the support of my advisor, Dr. Jayanta Kapat, as well as the many other members of CATER. Without their insightful discussions and useful advice, the current work would not have been completed.

TABLE OF CONTENTS

LIST OF FIGURES	vii
LIST OF TABLES	viii
CHAPTER 1: INTRODUCTION	1
Gas Turbine Thermodynamics	2
Gas Turbine Cooling	3
CHAPTER 2: LITERATURE REVIEW	6
Single Jet Impingement Heat Transfer	6
Jet Array Impingement Heat Transfer	9
Numerical Works on Jet Impingement	13
Impingement onto a Curved Surface	15
Crossflow Management in Jet Array Impingement	16
Impingement onto Target Surface with Features	17
Görtler Vortices	19
CHAPTER 3: PURPOSE AND PROBLEM STATEMENT	21
CHAPTER 4: EXPERIMENTAL SETUP AND DATA REDUCTION	22
Uniform Array	22
Non-Uniform Array	24
Wind Tunnel	28
Measurands and Measurement Instruments	28
Temperature Sensitive Paint	30
Heaters	35

Data Reduction	36
Heat Transfer	36
Pressure and Flow Distribution	42
Uniform Array	42
Non-Uniform Array	44
Uncertainty	46
 CHAPTER 5: COMPUTATIONAL SETUP	 50
Domain and Grid	50
Boundary Conditions	53
 CHAPTER 6: UNIFORM ARRAY RESULTS	 54
Flow Distribution	54
Heat Transfer	58
Computational Results	64
 CHAPTER 7: NON-UNIFORM ARRAY RESULTS	 69
Flow Distribution	69
Heat Transfer	74
Computational Results	84
 CHAPTER 8: CONCLUSION	 87
 LIST OF REFERENCES	 88

LIST OF FIGURES

Figure 1.1: Electricity generation and consumption in the U.S. (10^{15} BTU)	1
Figure 1.2: Brayton cycle illustration and diagrams	3
Figure 1.3: Modern gas turbine blade showing (Left) external surface with film cooling holes and (Right) cross-section with internal turbulated channels, trailing edge pin-fins and leading edge jet impingement. [4]	4
Figure 2.1: Nozzle geometries from Lee and Lee [1]. A: Square-edge B: Standard edge C: Sharp-edge	8
Figure 2.2: Crossflow schemes from Obot and Trabold [2]	12
Figure 4.1: Uniform array test section cross-sectional view of (a) curved configuration and (b) flat configuration	22
Figure 4.2: (a) Detailed sideview of curved configuration (b) Detailed sideview of flat configuration (c) Detailed streamwise-oriented view (d) composite view normal to jet plate	23
Figure 4.3: Cross-sectional view of non-uniform jet plate and test section	26
Figure 4.4: CAD model of rib turbulators on target surface	27
Figure 4.5: Top down view of CAD model of test section and wind tunnel setup	29
Figure 4.6: Static pressure tap locations on non-uniform jet plate	29
Figure 4.7: Camera arrangement and target plate cross-section	30
Figure 4.8: Jablonski energy level diagram showing luminescence processes of a typical luminophore	31
Figure 4.9: Processing of TSP from intensities to temperature	32
Figure 4.10 Curvature correction and TSP post-processing for curved test section	33
Figure 4.11 Typical calibration curve for temperature sensitive paint	34

Figure 4.12	In-house manufactured LEDs (Left); ISSI light source (Right)	34
Figure 4.13	Cross-section showing the different layers of material on the target plate	35
Figure 4.14	Initial (Right) and final (Left) layout of heaters for non-uniform array	36
Figure 4.15	1-Dimensional conduction loss diagram	38
Figure 4.16	Conduction loss test setup (Top); Conduction loss test data (Bottom)	39
Figure 4.17	Radiation loss test setup (Top); Radiation loss test data (Bottom)	40
Figure 4.18	Nusselt number uncertainty tree	47
Figure 4.19	Reynolds number uncertainty tree	48
Figure 4.20	Laterally averaged Nusselt numbers from repeatability tests	49
Figure 4.21	Standard deviation of Nusselt numbers in repeatability test	49
Figure 5.1:	Grid convergence study at $Re_1=50,000$	51
Figure 5.2:	Side-view of computational domain	52
Figure 5.3:	Structured mesh on jet plate	52
Figure 5.4:	Structured mesh in and around a jet hole	53
Figure 6.1:	Local $G_j/G_{j,avg}$ distribution for uniform array flat target plate case	55
Figure 6.2:	Local $G_j/G_{j,avg}$ distribution for uniform array curved target plate case	55
Figure 6.3:	Local G_c/G_j distribution for uniform array flat target plate case	56
Figure 6.4:	Local G_c/G_j distribution for uniform array curved target plate case	56
Figure 6.5:	Array average discharge coefficients as a function of Reynolds number for uniform array case	57
Figure 6.6:	Nusselt number profiles for uniform array flat target plate case	58
Figure 6.7:	Nusselt number profiles for uniform array curved target plate case	59
Figure 6.8:	Laterally averaged Nusselt numbers for uniform array flat target plate case	60
Figure 6.9:	Laterally averaged Nusselt numbers for uniform array curved target plate case	61
Figure 6.10	Row averaged Nusselt number comparison for uniform array at $Re_{j,avg}=55,000$	62

Figure 6.11	Row averaged Nusselt number comparison for uniform array at $Re_{j,avg}=100,000$	63
Figure 6.12	Area averaged Nusselt number comparison for uniform array	64
Figure 6.13	Comparison of experimental and computational results for laterally averaged Nusselt number at $Re_{j,avg}=55,000$ and $Re_{j,avg}=76,000$	65
Figure 6.14	Comparison of experimental and computational results for laterally averaged Nusselt number at $Re_{j,avg}=102,000$ and $Re_{j,avg}=126,000$	66
Figure 6.15	Comparison of experimental and computational results for row averaged Nus- selt number at $Re_{j,avg}=55,000$ and $Re_{j,avg}=76,000$	67
Figure 6.16	Comparison of experimental and computational results for row averaged Nus- selt number at $Re_{j,avg}=102,000$ and $Re_{j,avg}=126,000$	68
Figure 7.1:	Pressure ratio profile for non-uniform array cases 1 to 3	70
Figure 7.2:	Local G_c/G_j distribution for non-uniform array cases 1 to 3	71
Figure 7.3:	Local $G_j/G_{j,avg}$ distribution for non-uniform array cases 1 to 3	71
Figure 7.4:	Local jet Reynolds number distribution for non-uniform array cases 1 to 3 . .	72
Figure 7.5:	Local jet Reynolds number distribution for non-uniform array cases 1 and 4 to 6	73
Figure 7.6:	Local jet Reynolds number distribution for non-uniform array cases 1 and 4 to 6	73
Figure 7.7:	Nusselt number profiles for non-uniform array cases 1 to 3	75
Figure 7.8:	Laterally averaged Nusselt numbers for non-uniform array cases 1 to 3	76
Figure 7.9:	Row averaged Nusselt numbers for non-uniform array cases 1 to 3	77
Figure 7.10	Row averaged Nusselt numbers comparison of case 2 with correlations from Florschuetz et al. and Bailey and Bunker	78
Figure 7.11	Row averaged Nusselt numbers comparison of case 3 with correlations from Florschuetz et al. and Bailey and Bunker	79

Figure 7.12	Reynolds number sensitivity of area averaged Nusselt number	80
Figure 7.13	Reynolds number sensitivity of local row averaged Nusselt numbers	80
Figure 7.14	Nusselt number profiles for non-uniform array cases 1 and 4	81
Figure 7.15	Downstream Nusselt number profiles for non-uniform array cases 4 to 6	82
Figure 7.16	Downstream laterally averaged Nusselt numbers for non-uniform array cases 1 and 4 to 6	83
Figure 7.17	Downstream rib pitch averaged Nusselt numbers for non-uniform array cases 4 to 6	84
Figure 7.18	Laterally averaged Nusselt numbers comparison with CFD for non-uniform array cases 1 to 3	85
Figure 7.19	Row averaged Nusselt numbers comparison with CFD for non-uniform array cases 1 to 3	86
Figure 7.20	Local crossflow to jet mass flux ratio comparison between experiment and CFD for case 1	86

LIST OF TABLES

Table 4.1: Uniform Array Test Matrix	24
Table 4.2: Non-Uniform Array Jet Plate Geometry	25
Table 4.3: Rib Turbulator Parameters	26
Table 4.4: Non-Uniform Array Test Matrix	27
Table 7.1: Friction factor augmentation for cases 4 to 6	74

CHAPTER 1: INTRODUCTION

In 2014, the U.S. alone consumed 40.04 quadrillion BTUs of energy to produce 14.82 quadrillion BTUs of usable energy. This shows an average conversion rate of 37%. Of that 40.04 quadrillion BTUs, 8.05 quadrillion BTUs are generated from natural gas which is the primary fuel used by gas turbines for power generation. Figure 1.1 shows a flow chart which displays the sources and final uses of electricity generated in the U.S. Gas turbines also are used for nearly all commercial and military aircraft. At 1.43 million barrels being used per day, jet fuel comprises almost 8% of all petroleum use [3]. With the ever-increasing financial, political, and environmental pressures associated with the use of fossil fuels, and the staggering amounts of energy produced by them, it is clear how valuable even the smallest improvements in efficiency can be.

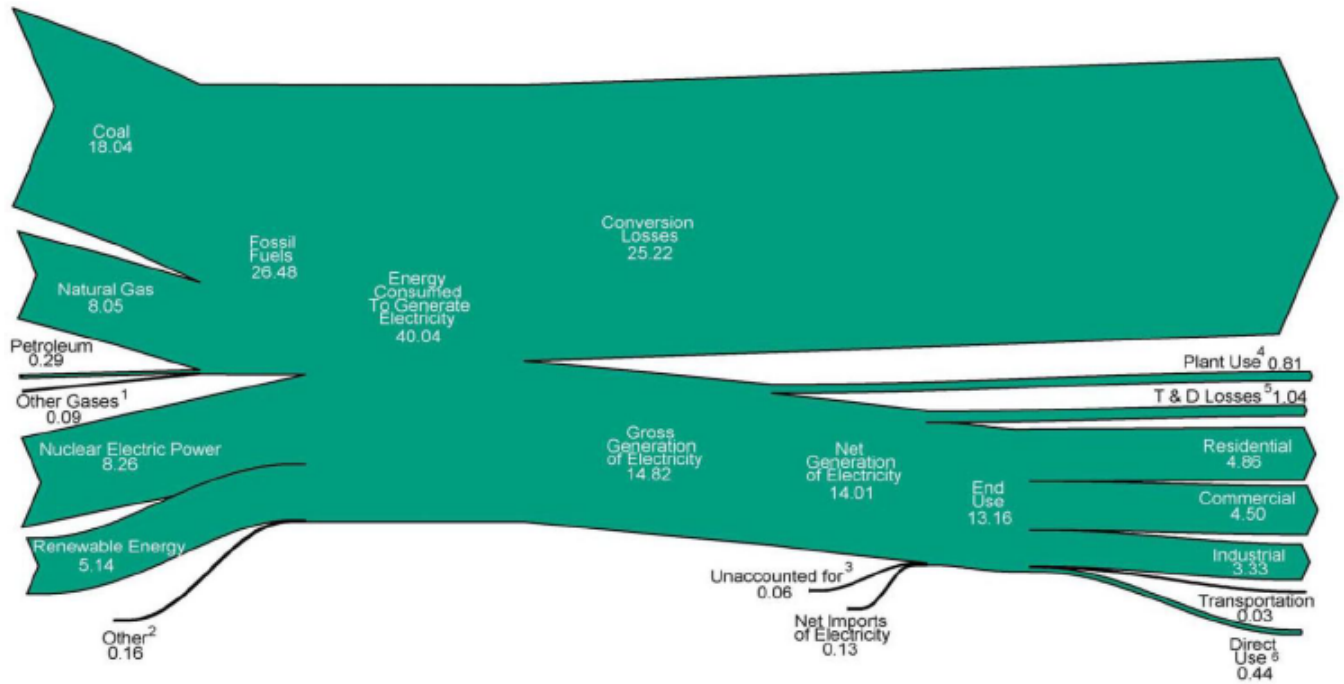


Figure 1.1: Electricity generation and consumption in the U.S. (10¹⁵ BTU)

Gas Turbine Thermodynamics

Gas turbines are heat engines. The thermodynamic cycle which describes the processes which the working fluid goes through in a gas turbine is called the Brayton cycle. In an ideal Brayton cycle, the working fluid goes through four distinct processes. These ideal processes are displayed in a Pressure-Volume graph as well as a Temperature-Entropy graph in Figure 1.2. The first process (1-2) is adiabatic compression, second (2-3) is isobaric heat addition, third (3-4) is adiabatic expansion, and the final process (4-1) is isobaric heat rejection. In a real engine, it is not possible to have an entirely adiabatic and loss-free process, and therefore there is some entropy gain in the compression and expansion stages. Additionally, real engines do not work in a close loop thus the heat rejection process does not exist. Instead the expanded fluid is exhausted to the atmosphere and fresh fluid is taken in for compression. In some cases, the waste heat from location 4 is extracted via a heat exchanger for heating of steam in a Rankine cycle. For turbines used as jet engines for aircraft, the fluid is only expanded enough to power the compressor in the process from 3 to 4, and is after accelerated through a nozzle to produce thrust for the aircraft. If it is assumed that the mass flows and specific heats of the fluid remain constant through the compressor and turbine, the isentropic efficiency of a gas turbine can be calculated using the following equation.

$$\eta_{isent} = 1 - \frac{T_1}{T_2} = 1 - \left(\frac{P_1}{P_2} \right)^{\frac{\gamma-1}{\gamma}} \quad (1.1)$$

Although it is not possible for a real process to be isentropic, real efficiencies will still reflect the principles displayed by this equation. From this equation, it can be seen that the efficiency of the engine can be improved by increasing the pressure ratio of the turbine. This equation shows us that having the highest pressure ratio possible will give the maximum efficiency.

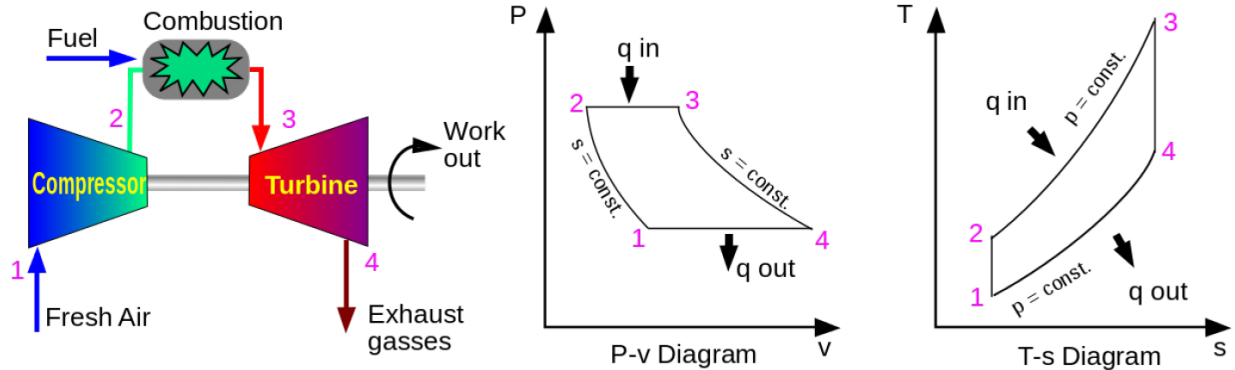


Figure 1.2: Brayton cycle illustration and diagrams

However, a further analysis shows that increasing this pressure ratio without increasing the combustion exit temperature will lead to zero work being produced by the turbine since the exit temperature of the compressor will continuously increase as the pressure ratio is increased. Therefore, in order to increase the specific power generated by the turbine, the combustion firing temperature must be raised as well. Having known this, engineers have continuously raised the firing temperature for modern gas turbines, and in fact, the temperatures seen in gas turbines have been substantially higher than the melting point of the metals used to construct them. The only possible way that these machines survive is through the use of advanced superalloys, ceramic thermal barrier coatings, and highly-advanced cooling schemes.

Gas Turbine Cooling

As mentioned in the previous section, one of the primary ways that the parts in a gas turbine survive the extreme temperatures is through the use of complex cooling schemes. This cooling air is bled from the compressor or midframe at various stages, thus the work done unto this air by the compressor is forfeited since it cannot be used in the combustion process.

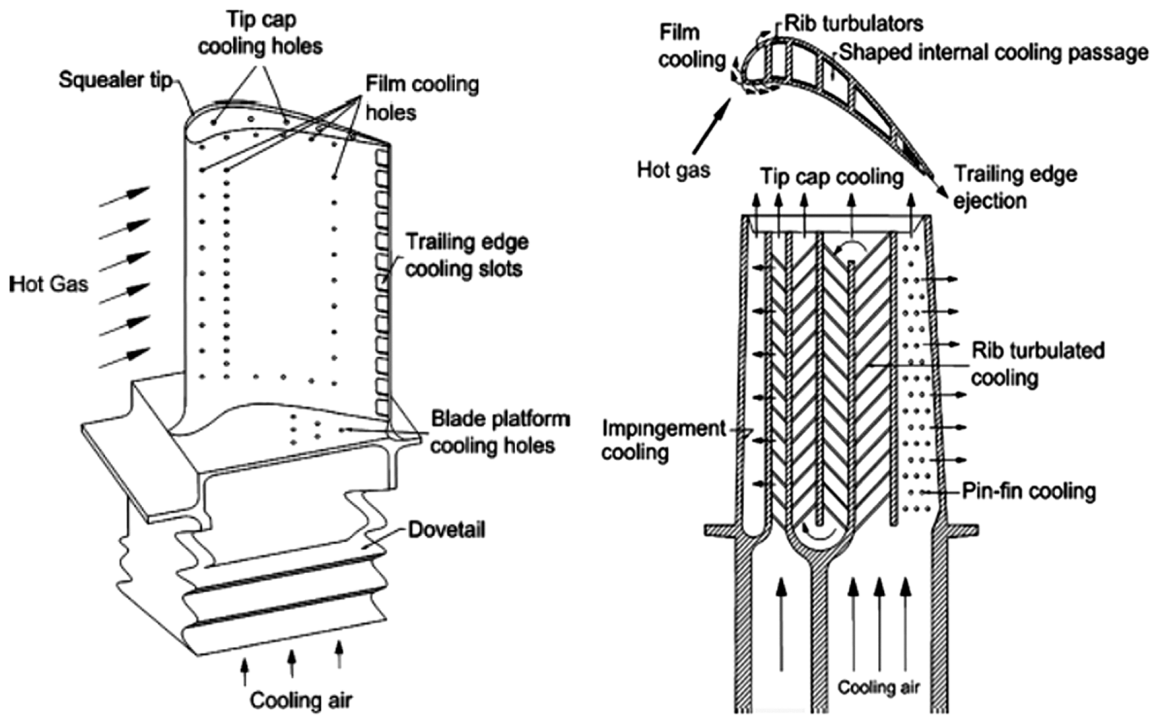


Figure 1.3: Modern gas turbine blade showing (Left) external surface with film cooling holes and (Right) cross-section with internal turbulated channels, trailing edge pin-fins and leading edge jet impingement. [4]

For this reason, it is the goal of the designer to optimize the cooling scheme such that it uses the minimum amount of cooling air to meet the target lifetime hours for the engine. These schemes generally contain one or more of three cooling methods; film cooling, internal turbulated channel cooling, and jet impingement cooling. Each of these methods is shown on a modern gas turbine blade in Figure 1.3. Film cooling can be described as the injection of a protective "cushion" of cool air surrounding a part by holes or slots. This "cushion" of cool air effectively reduces the incident heat flux onto a part by thickening the temperature boundary layer of the hot gas surrounding the part. However, by injecting this air into the mainstream, severe aerodynamic losses occur so it is only applied when absolutely necessary. Internal turbulated channel cooling is a broad term to cover use of any features on the surface of an internal channel of a part which improve the

heat transfer; such as ribs, dimples, or pin-fins. These features create local flow separation and reattachment zones as well as promote mixing of the flow to improve the rate at which heat is pulled from the part. Jet impingement is the last method used to cool parts in gas turbines. By forcing air through a perforated surface, jets are formed which impinge on the opposing surface, often called target surface, creating a thin boundary layer at the stagnation region which promotes high heat transfer rates. However, due to their localized nature, high thermal stresses can also be produced by impingement cooling. Therefore jet impingement heat transfer is well-suited for cooling localized areas which have very high thermal load, thus it is often implemented for cooling of combustor liners as well as first stage stator vanes and blades [4].

CHAPTER 2: LITERATURE REVIEW

Extensive research on the heat transfer performance of various impingement cooling schemes has been performed, starting in the 1960s.

Single Jet Impingement Heat Transfer

Goldstein et al. [5] studied an axisymmetric jet at jet-to-target wall spacings, Z/D , from 2 to 12 with jet Reynolds numbers ranging from 6.1×10^4 to 1.24×10^5 . For their testing, stainless steel heaters attached to the target surface were used to create the constant heat flux boundary condition, while 63 thermocouples embedded in the surface placed at radial distances, R/D , of 0 to 58 were used to measure surface temperature data. They found that the local Nusselt number dependence on Reynolds number could be approximated by a power-law dependence, $Nu \sim Re^m$, with the value of m being somewhat dependent on R/D . A constant m value of 0.76 was found to collapse their data reasonably well at all R/D values. A correlation for average Nusselt numbers at different integrally averaged radial distances was developed for the range of $R/D=0.5, 1, 2, 3, 6, 18$ and 32 and $Z/D \geq 6$.

$$\frac{\overline{Nu}}{Re^{0.76}} = \frac{A - |\frac{Z}{D} - 7.75|}{B + C(\frac{R}{D})^n} \quad (2.1)$$

For this equation, A , B , C and n are all constants. From this, it can be noted that the Nusselt number varies linearly with Z/D and that the Nusselt number is a maximum at $Z/D=7.75$. The distribution of the recovery factor on the target wall was also investigated. It was found that the recovery factor is independent of Reynolds number but is dependent on the jet-to-target wall spacing, Z/D , and radial distance from the jet, R/D .

One of the first pieces of literature to visualize the heat transfer from a single impinging jet was Goldstein and Timmers [6]. By placing a coating of thermochromic liquid crystals onto

the target plate, Nusselt number contours were obtained. The liquid crystals are calibrated such that only a small range of temperature can be measured, therefore in order to obtain these profiles the heat flux supplied to the surface via metal heaters was varied in order to get multiple lines of constant Nusselt number which were then plotted together. These data were obtained for a jet at a Reynolds number of 40,000 and jet-to-target plate distances of 2 and 6 jet diameters. From this data, a local minimum in Nu was observed near the stagnation point at a small jet-to-target plate distance and that higher stagnation heat transfer was seen at a jet-to-target plate distance of 6D. Baughn and Shimizu [7] also used liquid crystals to obtain heat transfer results for a single jet. Results are presented at a jet Reynolds number of 23,000 for a fully-developed jet at jet-to-target plate distances of 2, 6, 10 and 14 jet diameters. Area average and radial profiles of Nusselt number are presented. At $Z/D=2$, a secondary peak in the radial Nu profile was observed at a radial distance of approximately 2 diameters from the stagnation point. Like Goldstein and Timmers [6], a maximum stagnation Nu value was measured at $Z/D=6$.

Obot et al. [8], Pan et al. [9], Oyakawa et al. [10], and Lee et al. [1] all studied the effects of different nozzle configurations on the flow characteristics and heat transfer from a single impinging jet. Obot et al. [8] compared a contoured and sharp-edged nozzle at multiple nozzle lengths ranging from 1 to 50 diameters. The contoured nozzle had the shape of a quarter ellipse with a 2/3 to 1 diameter ratio. The Z/D values and jet Re values measured ranged from 2-16 and 15,000-60,000 respectively. Radial velocity and turbulence profiles are also presented. It was found that at nozzle lengths greater than 40D, the effect of nozzle inlet shape was negligible. Additionally, the heat transfer at Z/D values greater than 12 were seen to be independent of both nozzle shape and length. At nozzle lengths from 1 to 10 diameters, the sharp-edged nozzle showed both higher stagnation and area averaged Nusselt numbers. Pan et al. [9] also analyzed and compared a contoured and sharp-edged nozzle, although at only one jet-to-target plate distance of 1 diameter. To a radial distance of 2 diameters from the stagnation point, the sharp-edged geometry showed consistently higher heat transfer than the contoured, with some regions showing 40% higher Nu.

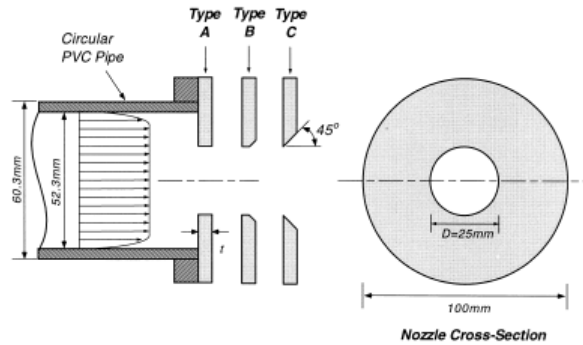


Figure 2.1: Nozzle geometries from Lee and Lee [1]. A: Square-edge B: Standard edge C: Sharp-edge

Oyakawa et al. [10] compared different nozzle shapes including circular, elliptic and cross-shaped. Jet-to-target plate distances of 1 to 12 diameters at jet Reynolds numbers from 15,000 to 35,000 were measured. Velocity and turbulence intensity profiles are reported at multiple distances from the jet plate as well as radial Nusselt number profiles on the target surface. As seen by other single jet studies, a secondary peak in the Nu was observed at low jet-to-target plate distances. Average Nusselt numbers within a radius of 5 diameters were found to be highest for the cross-shaped nozzle. Lee et al. [1] used the thermochromic liquid crystal technique to evaluate orifice plate-style nozzles when used for impingement. These included square-edge, standard edge, and sharp-edge nozzle geometries, as shown in Figure 2.1.

These nozzle geometries were evaluated at Z/D values of 2, 4, 6, and 10 while jet Reynolds numbers ranged from 5,000 to 30,000. The sharp-edged nozzle proved to give the highest heat transfer within the stagnation region, with this increase being more pronounced at lower jet-to-target plate distances.

Jet Array Impingement Heat Transfer

One of the earliest pieces of literature to study arrays of impinging jets is that by Kercher and Tabakoff [11]. The arrays studied for this work were all square, in that the streamwise and spanwise spacing between jets were equal ($X/D=Y/D$), with spacings between 3.1 to 12.5 diameters. Jet-to-target plate distances were 1 to 4.8 diameters with average jet Reynolds numbers ranging from 300 to 37,000. In this study, the spent air from the jets was forced to flow out in only one direction parallel to the target surface. Thus, the spent air from upstream jet rows forms a crossflow which affects the downstream rows of jets. Pressure, flow distributions and measured jet discharge coefficients are presented along with row averaged Nusselt numbers. A correlation for these Nu values is developed with graphically evaluated constants. It is noted that the Reynolds number exponent, m , in the correlation is a strong function of the streamwise jet spacing and that the crossflow at downstream rows causes a detriment in the heat transfer.

Metzger et al. [12] is another of the early array impingement works. Both inline and staggered arrays were studied at streamwise spacings of 5 and 10 diameters and spanwise spacings of 4 to 8 diameters. Z/D values of 1-3 were tested. As in the study by Kercher and Tabakoff [11], the spent air from the jets was forced to flow out in only a single direction. From their results, they noted that, at a constant Re, the upstream row averaged Nusselt numbers increased with Z/D , while the inverse was seen at the downstream rows. With a jet-to-target plate spacing of 1 diameter and spanwise spacings at 4 diameters, the heat transfer was measured to increase by a factor of 2 from the upstream to downstream rows. This was important because all previous studies had only stated that crossflow was detrimental to the heat transfer at the downstream rows. Finally, the heat transfer from inline arrays was found to give higher values than that from staggered arrays.

Among the most well-known and relevant literature related to impingement array heat transfer is the work performed by Florschuetz et al. for NASA [13] [14]. The work completed by Florschuetz et al. was performed with the goal of finding the optimum lateral and streamwise

jet spacing, Y/D and X/D , in order to maximize the target wall heat transfer. For their studies, streamwise spacings of $X/D=5, 10$ and 15 , along with spanwise spacings of $Y/D=4, 6$ and 8 were tested at jet-to-target wall spacings ranging from $Z/D=1$ to 3 . Additionally, jet average Reynolds numbers tested ranged from $5,000$ to $50,000$. This work's major contribution comes in the form of a correlation for pitch averaged Nusselt numbers as a function of the flow and geometric parameters of the channel.

$$Nu = ARe_j^m \left\{ 1 - B \left[\frac{Z}{D} \frac{G_c}{G_j} \right]^n \right\} Pr^{1/3} \quad (2.2)$$

Where $A, m, B,$ and n are all dependent on the geometric spacing of the jets in the channel and whether the jets are inline or staggered. Furthermore, a one dimensional analytical flow model was also developed, which gives the local jet mass flux to average jet mass flux ratio as well as the cross flow mass flux to local jet mass flux ratio.

$$\beta = \frac{C_D \sqrt{2\pi}/4}{\frac{Y}{D} \frac{Z}{D}} \quad (2.3)$$

$$\frac{G_j}{G_{j,avg}} = \frac{\beta N_c \cosh\left(\beta \frac{x}{x_n}\right)}{\sinh(\beta N_c)} \quad (2.4)$$

$$\frac{G_c}{G_j} = \frac{1}{\sqrt{2}C_D} \frac{\sinh\left(\beta \left(\frac{x}{x_n} - \frac{1}{2}\right)\right)}{\sinh\left(\beta \frac{x}{x_n}\right)} \quad (2.5)$$

In these equations, the term C_D is the discharge coefficient calculated using the isentropic flow relations. These equations are useful for trying to understand the varying flow distribution in the channel as well as the relative strength of the crossflow compared to the mass flux of the jet.

Obot and Trabold [2] were the first to suggest the concept of different jet-induced crossflow schemes in relation to jet array impingement. Three different schemes are presented,

referred to as minimum, intermediate, and maximum crossflow.

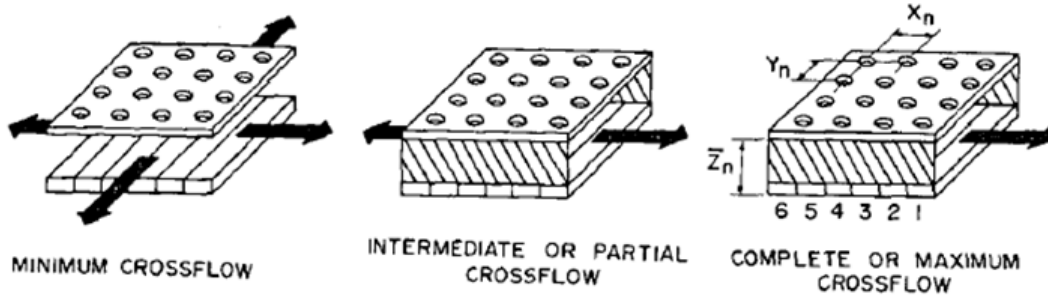


Figure 2.2: Crossflow schemes from Obot and Trabold [2]

These schemes, shown in Figure 2.2, refer respectively to unrestricted flow of spent air away from the target surface, restriction of the flow to leave through two opposite sides, and through one side of a rectangular impingement area.

After studying these various schemes at jet Reynolds numbers from 1000 to 21,000 and jet-to-surface spacings of 2 to 16 jet diameters, it was determined that the minimum crossflow scheme provided the highest magnitude and most uniform heat transfer results. Other conclusions were that, for a given massflow, a greater number of jets will give more pronounced heat transfer coefficient degradation, and that for a given Re , a larger open area equates to overall higher heat transfer coefficients.

The work by Bailey and Bunker [15] sought to create a correlation for streamwise pitch averaged Nusselt numbers, similar to that by Florschuetz et al. [14], which expanded the geometric limits of the correlation to include streamwise and spanwise jet spacings from 3 to 9 diameters. The jet Reynolds numbers studied ranged from 14,000 to 65,000. The correlation developed was of the following form.

$$Nu = 47.1 - 5.5 \frac{X}{D} + \frac{Z}{D} (7.3 - 2.3 \frac{Z}{D}) + Re_j (4 \times 10^{-3} - 1.3 \times 10^{-4} \frac{Z}{D} - 1.5 \times 10^{-8} Re_j) + \frac{G_c}{G_j} (61.2 - 13.7 \frac{X}{D} - 28 \frac{Z}{D}) \quad (2.6)$$

Park et al. [16] and Goodro et al. [17] analyzed the effect of jet Mach number on the heat transfer performance of a staggered impingement array. Park et al. [16] analyzed an array with streamwise and spanwise spacings of 8D. To study the effects of Mach number, a constant jet Reynolds number of 30,000 was run at Mach numbers ranging from 0.2 to 0.6. Alongside this, a constant jet Mach number of 0.2 was run at Reynolds numbers ranging from 11,100 to 59,700. The investigation showed that spatially averaged Nusselt numbers in the channel increased with increasing Mach number. With this data, the authors provide a Mach number correlation which corrects the aforementioned Florschuetz et al. [14] for flow at higher Mach numbers.

Numerical Works on Jet Impingement

As with many other engineering problems, computational methods have been employed heavily in the study of jet impingement heat transfer.

El-Gabry and Kaminski [18] performed a CFD study on an impingement channel containing 8 streamwise jet holes with the objective of comparing the Nusselt number predictions from the Yang-Shih and $k-\epsilon$ turbulence models. The geometry was ran at jet-to-target plate distances of 1 and 2 diameters, and jet inclination angles of 30, 60, and 90 degrees from the target plate normal. The computational results were compared against previous experimental data. It was found that, at low Reynolds numbers, the area average Nusselt number was better predicted by the Yang-Shih model with an error of 5% compared to that of $k-\epsilon$ at 9.4%. However, at higher Reynolds numbers this reversed with the Yang-Shih model error growing to 7.6% and that of $k-\epsilon$ dropping to 3.9%. Laterally averaged profiles for Nu were also presented for the experiment and both computational models. This showed that stagnation point Nu values were highly over-predicted by both models and that the fluctuations in the profile were much larger than the experiment. This is notable because although the area average Nusselt numbers were predicted quite well, local values varied by up to 20%.

The work by Mushatat [19] presents results for a 2-D slot impingement case with initial crossflow. In this study, multiple numbers of slot jets and rib features on the target wall were considered. Nusselt number predictions are compared against previous experimental studies. The results showed an increase in target wall heat transfer with an increase in the jet velocity to cross-flow velocity ratio. Additionally it was noted that an increase in the ratio of slot jet width to rib thickness yielded an increase in Nusselt number.

Zuckerman and Lior [20] performed a comprehensive review study on the ability of the various computational methods and models used for jet impingement to accurately predict the heat transfer and flow characteristics. For the comparison, the $k-\epsilon$, $k-\omega$, Reynolds Stress Model, Algebraic Stress Model, Shear Stress Transport, and $v^2 - f$ turbulence models were all analyzed, as well as Large Eddy Simulations as the only time-dependent model. Direct Numerical Simulation is also noted, however the extreme computational costs associated with it restricted its use at the time of publishing of the paper to only laminar jets in which the DNS approach offers little improvement in accuracy relative to other models. Each model is discussed in detail and also tabulated and given a rating on a scale of 1 to 4 for each models respective computational cost, Nusselt number prediction, and ability to predict the secondary Nu peak. Based off of this study, the $v^2 - f$ and SST models are recommended as a compromise between computational costs and Nu accuracy while LES produces the highest accuracy predictions.

Jefferson-Loveday and Tucker [21] presents a more recent study of Large Eddy Simulation used to model a single impinging jet. In this study, the sub-grid scale modeling of turbulence is omitted and the numerical dissipation of the scheme is used in place of this model. This technique is known as Numerical Large Eddy Simulation, or NLES. This study compares a zonal NLES model, and a wall-resolved NLES model with previous experimental works. The zonal NLES model uses a RANS turbulence model near the walls in an attempt to reduce the high computational cost associated with the dense near wall meshes that are required for LES. Velocity profiles, RMS turbulent velocity profiles and radial Nusselt number profiles are presented and compared with

experimental values. It was found that both the wall-resolved and zonal LES produced promising results. The wall-resolved model was also able to capture the secondary peak in the radial Nusselt number profile.

Impingement onto a Curved Surface

Most impingement literature has focused on jets which impinge perpendicular to a flat surface. However, due to the complex geometries in actual gas turbine applications this is not often the case. Most impingement occurs onto a curved surface. Some research has been done to observe how curvature affects the performance of impinging jets, but this has been primarily focused on leading-edge type geometries with small r/D values.

Metzger et al. [22] studied a single row of circular jets impinging onto a concave surface with a curvature of $r/D=1$. The authors state that the maximum measured heat transfer coefficients were observed at nozzle-target spacings of $Z/D=1$ for all center-to-center hole spacings. It is also noted that the heat transfer coefficients are higher than what is seen for similar impingement setups onto a plane surface.

Bunker and Metzger [23] investigate a leading-edge geometry at multiple values of leading-edge sharpness and jet pitch-to-diameter ratios, C/D . Overall heat transfer performance is a maximum at $C/D=3.33$ at close nozzle-to-apex spacings, however spanwise Nusselt number gradients are also shown to be a maximum with this geometry. The heat transfer in the leading-edge is also shown to be proportional to Reynolds number to the power 0.6 to 0.7. Metzger and Bunker [24] analyzes the same geometry as [23] but with the addition of showerhead film-cooling extraction holes. It is seen that the presence of the extraction holes increases the heat transfer levels when the extraction holes are in-line with the jet holes, and decreases the heat transfer levels when the extractions are staggered.

Taslim et al. [25] [26] [27] have performed several studies investigating various cooling ge-

ometries for turbine vane and/or blade leading edges. Taslim et al. [25] performed an experimental and numerical investigation on a leading-edge geometry with nozzle to target plate distances of 5.2D and 6.2D, which contained features on concave target surface. These features included a sandpaper rough geometry, conical bumps, and longitudinal ribs. The conical bumps were seen to increase heat transfer coefficients by about 8%, with overall heat transfer levels increased by 40% with the area enhancement taken into account. Taslim et al. [26] studied a similar geometry to [25] except that tangential horseshoe ribs and notched horseshoe ribs were placed as features on the target surface. Additionally, small longitudinal ribs were added to the target surface as well to see their effect. Also varied were the in-flow and out-flow conditions. The smooth wall case produced the highest heat transfer coefficients, however the notched horseshoe ribs were able to increase the overall heat transfer rate by up to 27%. Taslim and Bethka [27] once again studied a similar leading edge geometry to [25] and [26], however racetrack shaped holes were used in place of round holes. The novelty in this piece of literature came in that varying levels of initial crossflow in the leading edge region, and various inlet flow conditions were tested.

Crossflow Management in Jet Array Impingement

As previously mentioned, the spent air from upstream jets, termed crossflow, is generally detrimental to the heat transfer performance of jet array impingement. Because of this, particular attention has been given to methods which can mitigate this effect, thus allowing for a more uniform heat transfer profile and lower thermal stresses in the cooled surface.

Florschuetz and Tseng [28] studied non-uniform arrays which contained two distinct regions of jet spacings and/or diameters. The results were compared against data and correlations from previous work performed by Florschuetz et al. [14]. It was found that the correlations were able to predict the flow distribution and heat transfer for the rows, with the exception of one or two rows at the transition between the two differing regions.

Gao et al. [29] and Hebert et al. [30] performed a two-part study to analyze crossflow alteration methods. Gao et al. [29] studied a linearly stretched array for constant and varying jet diameter cases. The varying diameter case was found to provide higher heat transfer except at the first few upstream rows. Both a converging and diverging channel were studied by Hebert et al. [30] to see the effects of streamwise pressure gradient. The results showed that the streamwise pressure gradient had little effect and that the heat transfer at each row matched that of a parallel channel with the same jet-to-target plate spacing.

The work done by Uysal et al. [31] compared the heat transfer of a constant diameter line of impinging jets with a line of increasing diameter jets. Heat transfer profiles were obtained for all surfaces of the channel, including the jet plate. The conclusion notes the potential for non-uniform jet diameters seeing as how the heat transfer profiles for the increasing diameter case were relatively unaffected by the crossflow.

Esposito et al. [32] studied novel jet plate geometries that included corrugated, extended port, and variable extended port geometries. Tens rows of jets were used at Reynolds numbers from 20,000 to 60,000. All geometries showed increases in heat transfer over a baseline array, however the extended port geometry was able to achieve 40-50% increases in heat transfer at the tenth jet row. The authors also suggest that dense staggered arrays could be used with these arrays for further improvements.

Impingement onto Target Surface with Features

In order to increase the heat transfer achieved from jet impingement, features such as pins or ribs can be placed onto the target surface. Many studies have been performed which analyze how various feature shapes, sizes and orientations relative to the impinging jets influence the heat transfer and pressure drop characteristics of the array.

The study by Mhetras [33] investigated two different jet plate geometries at jet Reynolds

numbers up to 450,000. Both jet plates were non-regular with one plate having increasing jet diameters to negate the effects of crossflow, while the other plate had decreasing jet diameters in order to maintain constant mass injection through each row. Different variations of a turbulated target plate, including streamwise riblets, dimples, and short pins, were also tested. The decreasing diameter jet plate was seen to achieve higher magnitudes of heat transfer with a more uniform profile. The target surface with short pins achieved the highest Nusselt numbers of all cases with up to 2.1 times higher surface average Nu values than the smooth wall case.

Annerfeldt et al. [34] studied a staggered impingement array with features placed in the locations in-between jets. The features tested included triangle, wing, cylinder, and dashed rib shaped geometries at heights ranging from $1/3$ to the complete channel height. Increases in Nu values are seen in the range of 1-1.3 when compared to a smooth target wall, however large increases in required pumping power are also observed. With this in mind, it is noted that features which traverse the full channel height should be avoided and that the circular and rib geometries provide the best results in terms of cooling efficiency. Additionally, the authors note that these geometries are more suited for use in regions where high-crossflow is present.

Haiping et al. [35] studied the use of 90 degree ribs on the target surface at jet Reynolds numbers ranging from 7,000 to 15,000 with initial crossflow. The channel height varied from 1.5 to 5 jet diameters while the rib height was varied from 0.75 to 1.5 jet diameters. It was found that, at small channel heights and large spanwise jet spacings, row-averaged Nusselt numbers increased with increasing crossflow, with the opposite occurring for small spanwise spacings. Additionally, lower rib heights showed more uniform heat transfer.

The work done by Andrews et al. [36] presents results for impingement onto a surface with rectangular pin fins. Results for jets both inline and offset with the pin fins were obtained. Overall, the heat transfer coefficient values were not affected significantly by the pin fins, with a maximum increase of 15% seen. Like previously mentioned studies, the authors noted that these features were only useful with significant levels of crossflow. The inline case was found to produce higher

heat transfer due to better protection of the jets from the crossflow. Furthermore, an upstream deterioration in heat transfer coefficients compared to flat was noticed and was attributed to the increased pressure drop causing a significant redistribution of flow in the channel.

Woei et al. [37] performed a study using convex dimples on the target surface. The location of the dimples was shifted from directly under each jet to of the jet spacing. Jet Reynolds numbers ranged from 5,000 to 15,000 and separation distances ranged from 0.5 to 11 diameters. It was found that the dimples caused an increase in Nu and better uniformity at larger Z/D values and lower Reynolds numbers when compared to a smooth surface. The highest heat transfer was obtained when the dimples were shifted of a jet spacing.

Brakmann et al. [38] investigated the effects of cubic micro pin fins on the target surface of a narrow wall impingement channel. The pin fins were 0.22 diameters in side length and had spacings of 0.625 diameters. Minimum, intermediate, and maximum crossflow schemes were all tested. For each case, the average Nusselt number on the target plate was found to decrease by approximately 10% relative to the smooth wall case. However, the 50% increase in area given by the pin fins led to increases in overall heat transfer rate in the range of 35 to 42%, with only a maximum of 14% increase in pressure drop.

Görtler Vortices

In the present study, the crossflow is forced to flow tangentially to a concave surface with the maximum crossflow scheme as in [8]. It has been seen that wall curvature can induce boundary-layer instabilities in the form of streamwise-oriented counter-rotating vortex pairs, or so-called Taylor-Görtler vortices. A prediction of the on-set of these vortices can be made utilizing a parameter known as the Görtler number, G , where the presence of these vortices is seen above a critical value of this parameter [39]. These vortices act to convect streamwise momentum normal to the wall. This action can lead to a thinning of the boundary-layer in the downwash section of the vor-

tex. This local thinning of the boundary-layer, along with bulk mixing of the flow caused by the vortex structure, has been shown to increase heat transfer on the curved surface by a considerable amount [40]. While this phenomenon has been shown to increase heat transfer in a relatively simple flow-field, such as the pressure side of a turbine blade [41], it is the goal of the present work to recognize any possible influences of these vortex structures in the considerably more complex flow-field of jet array impingement. A prediction of the presence of these structures based off of the Görtler number also serves to be difficult due to problems relating to the estimation of boundary-layer thickness. The complex flow-field, consisting of stagnation, wall-jet and fountain regions, causes extreme variations in the boundary-layer. However, based off a simple knowledge of this array flow-field, one could expect to potentially see an affect from these Taylor-Görtler vortices at downstream locations in the lateral regions in-between jets, where crossflow is at a maximum and there is no jet stagnation.

CHAPTER 3: PURPOSE AND PROBLEM STATEMENT

The main goal of the present work was to determine if the large-radius curvature of the target plate in the current study has an effect on the pressure distribution or heat transfer characteristics of a uniform array of impinging jets. In order to test this, two experimental rigs were created with identical jet spacings; one with jets impinging onto a flat target plate and another with the jets impinging onto a curved target plate. The spacings were chosen such that they fell within the bounds of established correlations for jet array impingement heat transfer and flow distributions.

Alongside this, a geometry representative of an actual array used in a gas turbine engine with impingement onto a large-radius curvature target plate was also evaluated in terms of flow and heat transfer distributions. This geometry contains multiple jet diameters and varying jet spacings. Another of the goals of the tests was to analyze how the heat transfer and pressure drop in the channel changed with the removal of downstream rows of jets and to test the possibility of using turbulators in place of these removed downstream rows. In high crossflow scenarios, the heat transfer of the jets can be severely diminished even though there is still a high cost in terms of mass flow and pressure drop.

CHAPTER 4: EXPERIMENTAL SETUP AND DATA REDUCTION

Uniform Array

To test the effects of a large-radius curvature on jet array impingement, a uniform array with identical spacings was tested on both a curved and flat target surface. For the curved and flat impingement cases, separate test sections were fabricated. Both channels consisted of an aluminum jet plate 6 mm thick containing holes with diameter of 28mm, a target wall and two side walls. One of these sidewalls is instrumented with pressure taps located between jet rows. The jet plate holes are sharp-edged and have an $L/D=0.21$. The target plate is machined from a 24 mm thick acrylic plate. For the curved case, the target plate was thermo-formed to the correct radius and the jet plate was fabricated to maintain a constant radial gap of 84 mm. The curved target plate was set to a radius of 884 mm giving a r/D value of 31.57 for the uniform array cases. A plenum was used to guide quiescent ambient air through the jet plate. For the curved case, the crossflow is forced to flow tangential to the plate curvature. A cross-sectional view of the test sections can be seen in Figure 4.1. The spacings of the jets were chosen as $S/D=X/D=5.79$, $Y/D=4.49$, and $Z/D=3$.

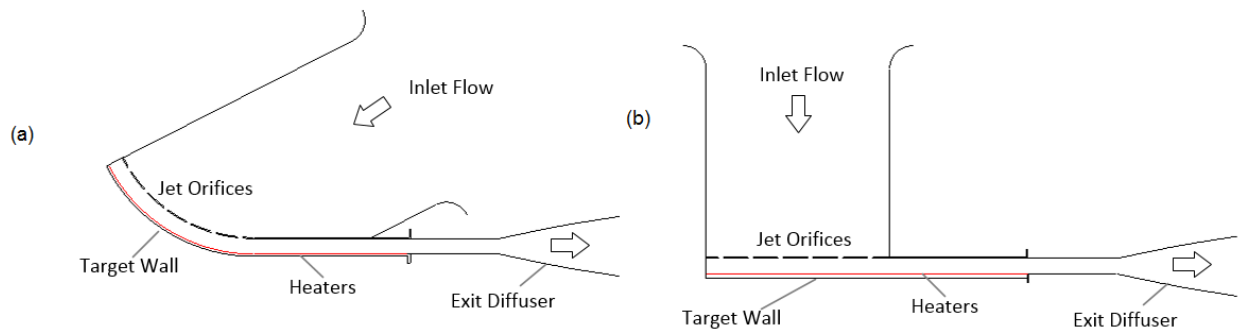


Figure 4.1: Uniform array test section cross-sectional view of (a) curved configuration and (b) flat configuration

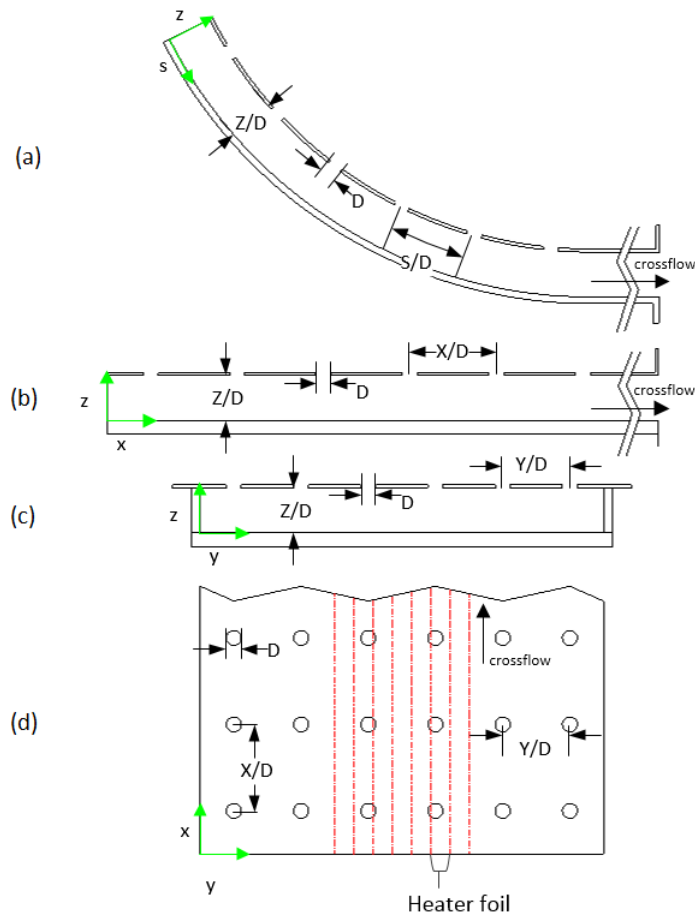


Figure 4.2: (a) Detailed sideview of curved configuration (b) Detailed sideview of flat configuration (c) Detailed streamwise-oriented view (d) composite view normal to jet plate

These spacings were chosen as they utilized the full curvature and fell within the bounds of the correlation developed by Florschuetz et al. [14]. A detailed cross-section of the jet and target plates is provided in Figure 4.2. Both the streamwise and spanwise spacing is kept constant throughout the array. The streamwise spacings for the curved case were maintained such that the heat transfer areas for both the curved and flat case were identical. After the flow impinges on the target wall, it moves downstream through a constant cross-section rectangular duct of $24.5D$ length without any impingement holes. After this, it exits the channel into transition which converts the rectangular profile of the channel into a circular profile while acting as a diffuser. For the comparison

between the curved and flat uniform array geometries, average jet Reynolds numbers from 55,000 to 125,000 were tested. The test matrix for the comparison is displayed in Table 4.1.

Table 4.1: Uniform Array Test Matrix

Plate Case	r/D	X/D or S/D	Y/D	Z/D	$Re_{j,avg} \times 10^3$
Curved	31.57	5.79	4.49	3	55, 75, 100, 125
Flat	N/A				

Non-Uniform Array

For the non-uniform array tests, the same test section was used as with the curved uniform array tests, except for a different jet plate. The impingement channel consists of an acrylic jet plate containing the jet holes, a target wall and two side walls. The jet plate was thermoformed from 6 mm acrylic in an effort to reduce costs. The high pressures during testing required reinforcement ribs along the straight section of the jet plate which are 12.2 mm thick and 50.8 mm tall. The jet plate holes are sharp-edged and have an $L/D=0.16-0.29$. The same target plate used for the curved uniform array tests was used. A plenum was used to guide quiescent ambient air through the jet plate. The diameters and geometric spacings for each of the jet rows are presented in Table 4.2 and an illustration of the jet placements is in Figure. The first 9 jet rows impinge onto the curved surface, where the crossflow is dictated to flow in one direction, tangential to the curvature. The downstream rows 10-14 impinge onto a flat surface. Jets are in-line in the stream-wise and span-wise direction, with the exception of the final row where there are four jets instead of the seven in the previous rows. The non-uniform array was run at first row Reynolds numbers of 50,000, 125,000 and 160,000. For this study, the geometry containing all 14 rows was considered the "Original" geometry. The cases which were run using only rows 1 to 9 are termed the "Restricted" geometry.

Table 4.2: Non-Uniform Array Jet Plate Geometry

Curved Section					
Row #	θ (Degrees)	D/D ₁	S/D	Y/D	Z/D
1	3.8	1	3.2	2.6	2.29
2	11.4	1	3.2	2.6	2.29
3	18.8	1	3.12	2.6	2.29
4	25.4	1	2.78	2.6	2.29
5	31.9	1	2.74	2.6	2.29
6	39.1	1	3.03	2.6	2.29
7	46.8	0.71	4.58	2.6	3.24
8	54.6	0.64	5.11	2.6	3.57
9	62.8	0.64	5.37	2.6	3.57
Straight Section					
Row #	-	D/D ₁	X/D	Y/D	Z/D
10	-	0.55	5.72	4.8	4.2
11	-	0.55	5.76	4.8	4.2
12	-	0.57	5.5	4.6	4
13	-	0.57	5.52	4.6	4
14	-	0.64	4.92	8	3.57

The first row Reynolds number was used to characterize the flow for the non-uniform cases for comparison between the cases with the Original and Restricted geometries. The only geometry run with downstream turbulators was the Restricted geometry, and all Restricted geometry cases were run at a first row Reynolds number of 125,000.

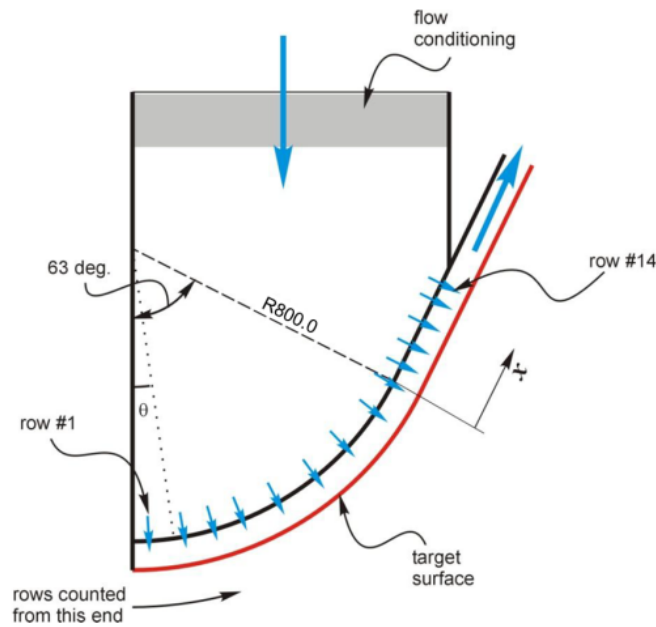


Figure 4.3: Cross-sectional view of non-uniform jet plate and test section

Two designs of turbulators were tested: 1) 90° ribs and 2) W-Shaped ribs, as shown in Figure 4.4. These turbulators were made of a PVC rod material. A rod shape was used since it is representative of the brazing of a thin wire onto a part, a typical practice for creating turbulators on real engine parts. Additionally, the bends of the W-shaped ribs were slightly rounded to be more representative of an engine geometry as well. The rib configurations are shown in Table 4.3. All cases run using the non-uniform array can be seen in Table 4.4.

Table 4.3: Rib Turbulator Parameters

Rib Type	P/e	e/Z	w/Z	Rib Angle of Attack	Number of Ribs
Design1/90°	15	0.0476	N/A	90°	9
Design2/W-shaped	15	0.0476	1	45°	9

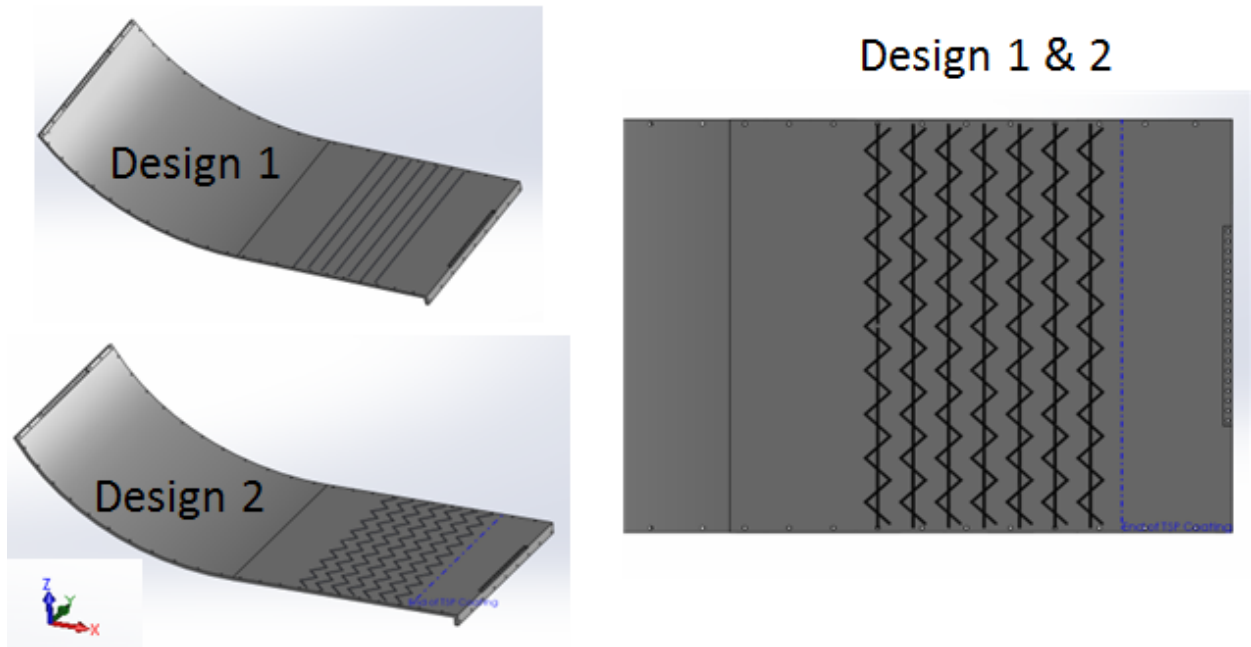


Figure 4.4: CAD model of rib turbulators on target surface

Table 4.4: Non-Uniform Array Test Matrix

Test Case	Geometry	First Row Jet Re	Turbulators
1	Original (All Jets)	125,000	None
2		50,000	
3		160,000	
4	Restricted (Rows 10-14 Blocked)	125,000	Design 1
5			
6			

Wind Tunnel

A wind tunnel was designed and constructed to accommodate the large test section and to allow for detailed analysis of the unique geometry and dimensions of the test section. Due to space constraints in the lab (5.36 m \times 12.19 m) and the required upstream length for the orifice plate, the tunnel could not be constructed as a simple straight apparatus. Bends in the piping were introduced to fit the wind tunnel into the given space. The wind tunnel consists of three straight pipes, two elbows, one diffuser, one rectangular pipe, orifice plate and plenum on which the test section is connected. The pipe diameter is 347.675 mm, and the rectangular pipe has a cross-section of 84 mm \times 755 mm. Figure 4.5 displays a CAD model of the wind tunnel. All pipes were constructed from stainless steel 304 due to its strength and corrosion resistance. The orifice plate was used to measure total mass flow rate and follows ASME PTC 19.5 [42]. The orifice plate is located between the 1.78 m and 3.55 m straight pipes, and has a diameter of 260.48mm. This gives the orifice plate a diameter ratio of 0.75. The orifice plate has a large diameter ratio to limit the pressure loss so that the high mass flow rates required for the tests could be reached with the available blower. The flow is pulled by a blower connected to a 250-hp electric motor. Just prior to the blower is a butterfly valve which is used to control the flow through the channel.

Measurands and Measurement Instruments

The major measurands in the experiment are pressure in the impingement channel and temperature on the target plate. Heat transfer coefficients, and thus Nusselt numbers, are derived from the temperature and the constant heat flux boundary condition applied on the target plate. Temperature Sensitive Paint (TSP) is used to measure the temperature on the target surface. As shown in Figure 4.6, static pressure taps are located on the flow side of the jet plate along two streamwise lines between streamwise columns of jets: in-line with the jet rows and staggered between jet rows.

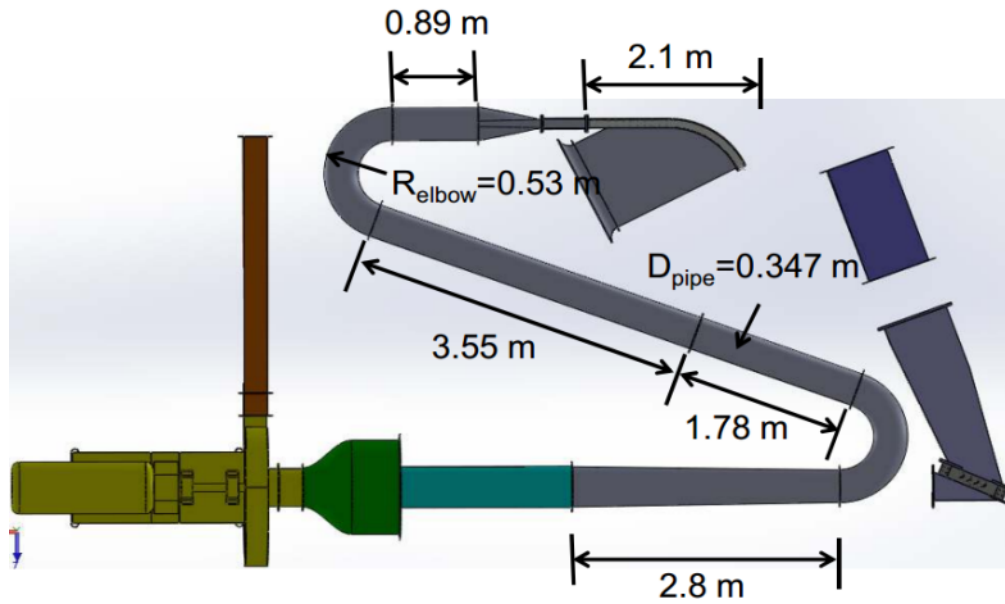


Figure 4.5: Top down view of CAD model of test section and wind tunnel setup

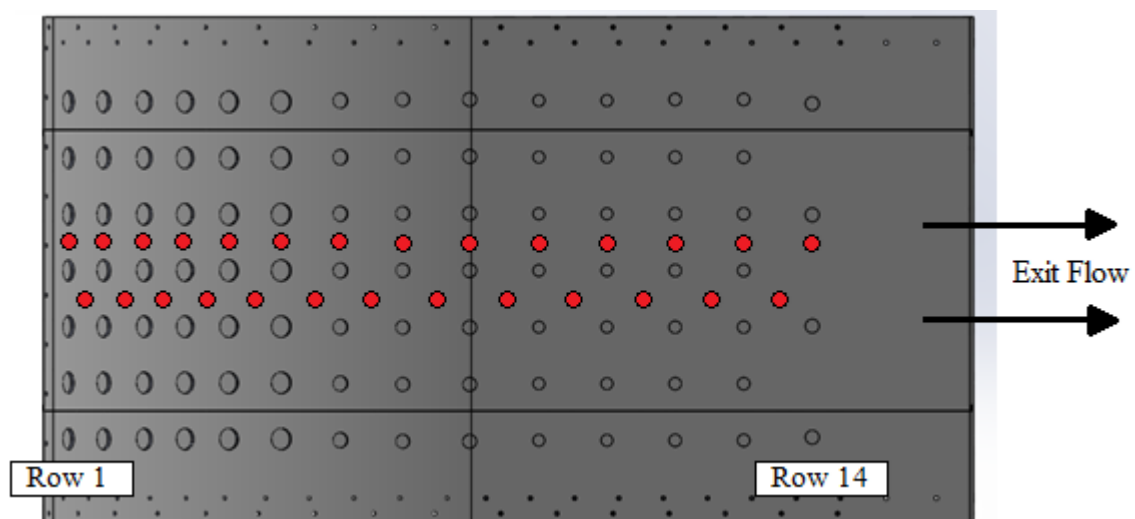


Figure 4.6: Static pressure tap locations on non-uniform jet plate

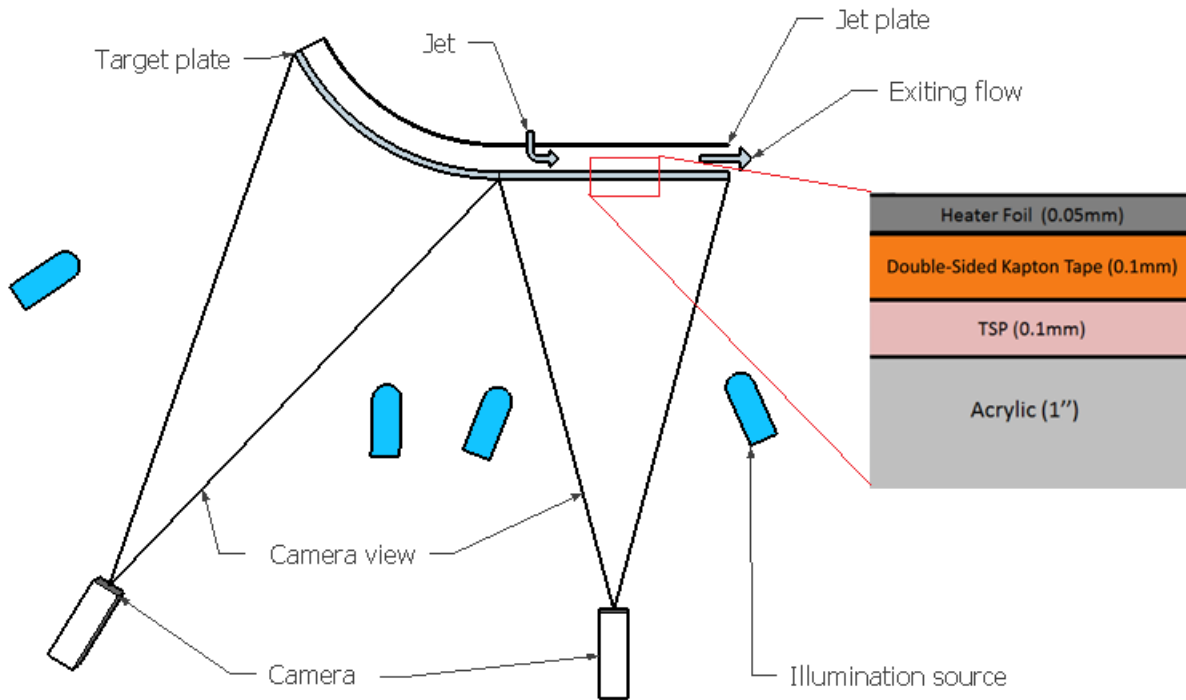


Figure 4.7: Camera arrangement and target plate cross-section

Temperature Sensitive Paint (TSP) is a surface measuring method and is the primary tool used in this experiment. Due to the size and aspect ratio of the testing surface, a multi-camera setup had to be utilized, as shown in Figure 4.7, to obtain the data from the temperature sensitive paint.

Temperature Sensitive Paint

Temperature Sensitive Paint (TSP) is a combination of luminescent molecules and a polymer binder. Any desired surface, such as the impingement target plate for this experiment, can be coated with this paint to obtain a temperature distribution on that surface. In order to obtain this temperature distribution, the surface must be illuminated with 460 nm wavelength light, which excites the luminescent molecule.

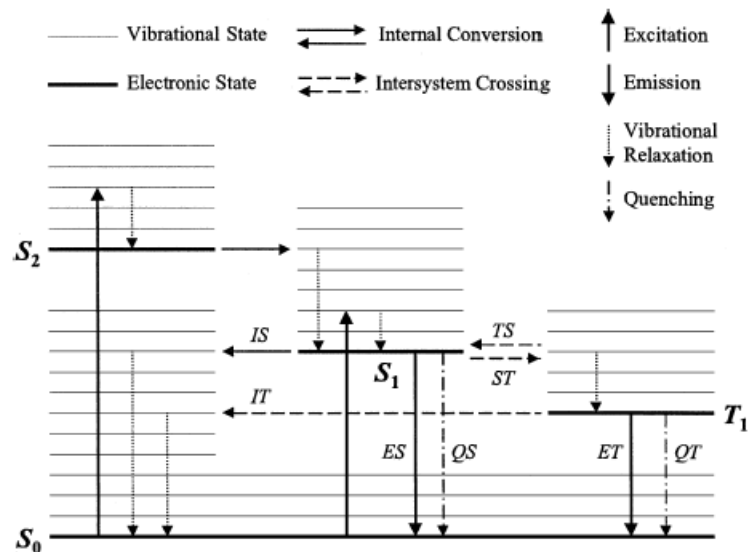


Figure 4.8: Jablonski energy level diagram showing luminescence processes of a typical lumiphore

The molecule returns to its original energy state through the competing effects of emission of the longer wavelength light and thermal quenching, with the probability that the energy will be dissipated through thermal quenching increasing with temperature, thus the intensity is inversely proportional to the temperature. This process is graphically represented in the Jablonski diagram in Figure 4.8. The intensity distribution of the fluorescence from the luminophores is captured with a PCO CCD camera with a high-pass filter at a resolution of 16001200 pixels. The calibration curve for TSP is based off of an intensity ratio as a function of a temperature difference. The process by which a temperature distribution is obtained from the intensity distribution requires two pictures: one reference picture, the cold picture, taken when the entire surface is at a known uniform temperature, and another, the hot picture, of the unknown temperature distribution at steady state. This ratio of intensities from hot image to cold image is the value fed into the TSP calibration to obtain a temperature at each pixel. This method of taking intensity ratios, shown in Figure 4.9, leads to a technique which is rather insensitive to lighting and paint variations.

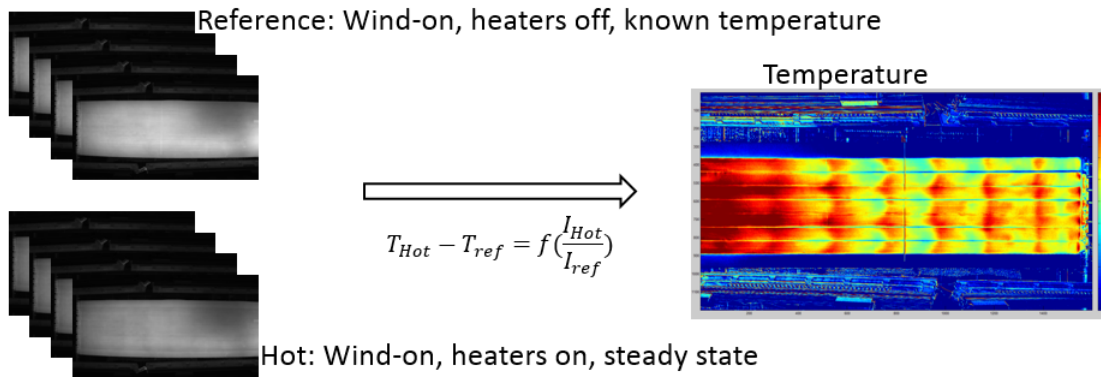


Figure 4.9: Processing of TSP from intensities to temperature

For each of these pictures, sets of 8 are taken and averaged in order to reduce the noise of the pictures. This entire process of averaging pictures to obtaining temperatures from the TSP calibration curve and then later heat transfer coefficients is performed by means of in-house developed MATLAB codes. On the curved section of the target plate, a two-step transformation process is done to process the heat transfer data. First, the averaged TSP images are lens corrected using a polynomial transformation. This corrects the images so that all the stream-wise lines on the test surface become parallel. Next, 18 evenly spaced circumferential markers are used to map this surface to its correct curved shape. This process is shown in Figure 4.10.

The calibration curve for the TSP is obtained through experiment. A one inch (25.4 mm) by one inch acrylic coupon is painted with six to nine layers of TSP as the calibration piece. This coupon is placed with the TSP painted side onto a copper block which sits on top of a small electric heater. A thermistor is placed into the center of the copper block to accurately measure the temperature of the block and thus the TSP. The heater was used to heat the test piece to 10 different temperatures, and by monitoring the thermistor, steady state conditions were ensured. By measuring the intensity ratios of the TSP at each of these known temperatures, the calibration curve could be found, such as the one shown in Figure 4.11.

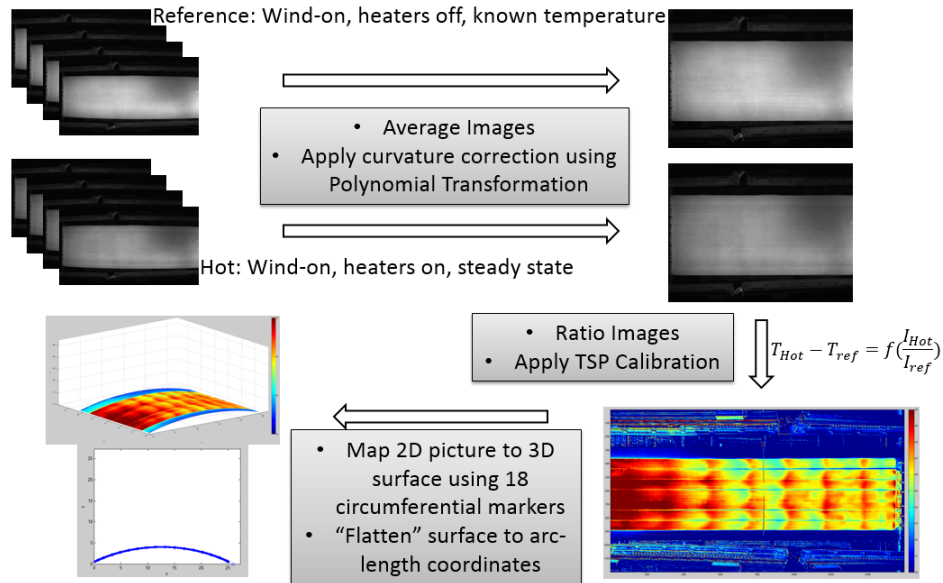


Figure 4.10: Curvature correction and TSP post-processing for curved test section

One difficulty encountered during the testing with TSP was with the excitation light source. As mentioned previously, the TSP requires excitation via a 460 nm light source. Due to the large surface area of the TSP covered test section and the high price of the light source when purchased from ISSI, the developer and supplier of TSP, custom in-house manufactured LEDs were attempted. Bread boards to mount the LEDs to were machined using acrylic, while 460 nm standard through hole LEDs with a diffusion angle of 3 and 33.2 ohm resistors were soldered onto copper tape placed onto the bread boards. Sanded acrylic panels were also mounted on top of these LEDs to act as diffusers in an attempt to achieve more uniform intensities on the TSP surface. After initial testing, it was found that the results obtained while using these LEDs were not repeatable. Thus a light source from ISSI was tested and proved to give reliable results. The ISSI light sources contain built-in air cooling and power source signal conditioning to ensure consistent emission. Both light sources are shown in Figure 4.12. However, due to the limited availability of the light source, only two ISSI light sources are in possession and thus only a limited portion of the TSP test section can be sufficiently illuminated for testing at once.

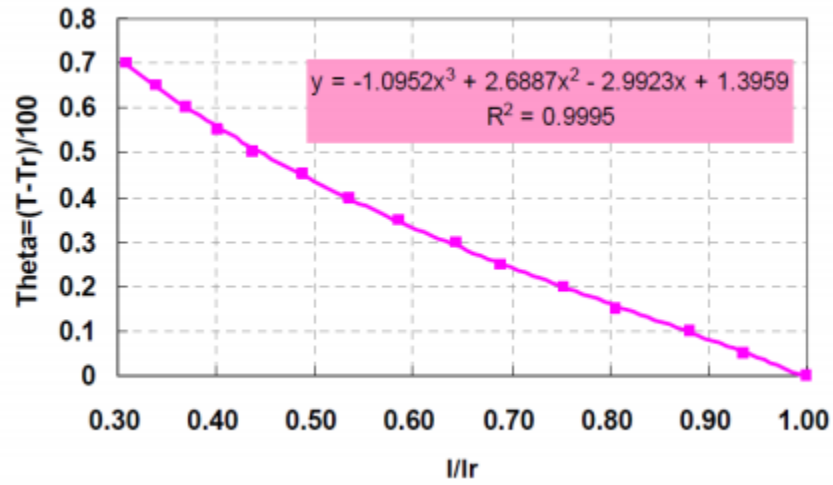


Figure 4.11: Typical calibration curve for temperature sensitive paint

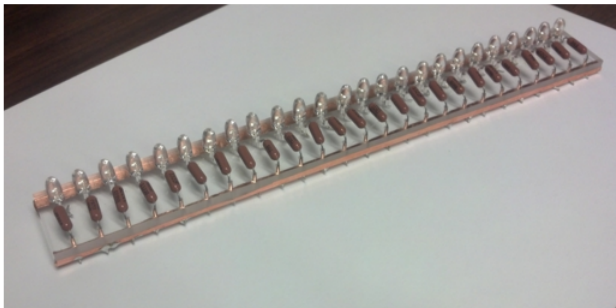


Figure 4.12: In-house manufactured LEDs (Left); ISSI light source (Right)

Therefore, testing is required to be done in two steps, with the curved portion of the test section illuminated and completed first and then the straight section.

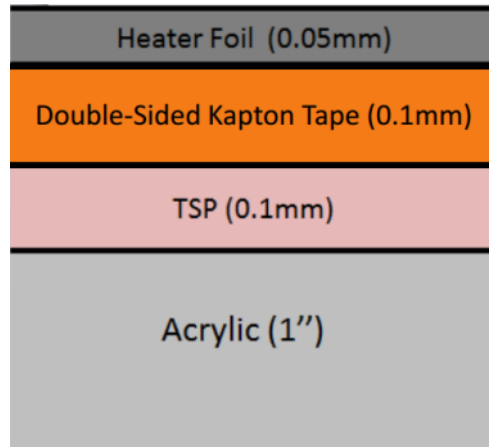


Figure 4.13: Cross-section showing the different layers of material on the target plate

Heaters

A constant heat flux boundary condition is used in these experiments. Heaters were cut and applied onto the target plate on the surface which TSP was applied. For the non-uniform array case, originally, in order to achieve the correct current and heat flux, 12 stainless steel type 321 foil heaters with an average resistance of 720×10^{-7} Ohm-m were applied with a width of 30 mm and a thickness of 5.06×10^{-5} m. The heaters spanned the length of the target plate. These heaters were connected using copper bus-bars and power was supplied using a four 120 V, 20A variable AC power supplies (VARIAC). In order to control the heat flux more closely and ensure less uncertainty through current, the layout of heaters was changed so that only seven heaters of 39mm width were needed, and power was supplied by one VARIAC. The uniform case also used seven heater strips, although these heaters only were placed under the two middle jets of each row. The heaters were adhered to the target plate using double-sided Kapton tape, which is electrically isolative and thermally conductive. With the initial heater layout for the non-uniform array, problems occurred. The heaters would lift off the surface due to air pockets that expanded when heated and airflow penetrating the underside of the heaters.

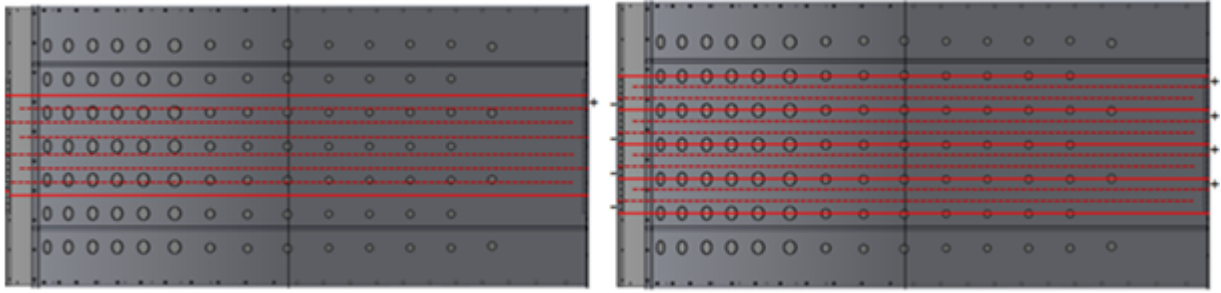


Figure 4.14: Initial (Right) and final (Left) layout of heaters for non-uniform array

An attempt to remedy this was made by laying a uniform sheet of single-sided Kapton tape over the heaters providing additional stability so that air could not penetrate the underside. However, this layout created additional opportunities for air pockets and so the heaters continued to buckle. The layout of the heaters was changed so that seven heaters of 39mm width were used, which covered the impingement area of the three middle jets for each row, with no single-sided Kapton tape placed on top. These heaters spanned a smaller part of the test section, but ensured more accurate data. Improved skill in application paired with less heaters lead to almost no buckling of the heaters during testing. The final layout is shown in Figure 4.13 and Figure 4.14.

Data Reduction

Heat Transfer

In order to determine the heat transfer coefficient distribution for the impingement array, the input heat flux generated by the metal heaters is calculated using the electrical current and heater electrical resistance. This can be seen in the following equation, where A_s represents the surface area of the heater exposed to the coolant flow.

$$q_{gen}'' = \frac{I^2 R_{el}}{A_s} \quad (4.1)$$

The heater resistance is calculated using the equation below, with the resistivity of the stainless steel being temperature dependent. The length (L) is the length of the heater in the stream direction, S or X, while the width (w) is measured in the span direction, Y, of a single heater strip. The thickness (t) is the thickness of the heater in the wall normal direction, Z. By using a temperature dependent resistivity, the effects of spatially varying heat flux generation are mostly accounted for; however, this method makes the small assumption that the current density remains constant through the width of the heater. This is shown to be a valid assumption since the resistivity across the width of any heater strip is seen to vary by a maximum of only 0.6%.

$$R_{el} = \frac{\rho_{el}(T)L}{wt} \quad (4.2)$$

Due to the nature of the test setup and the fact that the acrylic on which the heaters are attached is not a perfect insulator, some of the input heat is lost to conduction through the acrylic and radiation to the surroundings. In order to estimate this heat loss, a simple analytical one-dimensional conduction model was initially used. The temperature difference for this model is the heater temperature, assumed to be constant throughout its thickness, and the ambient temperature on the backside of the acrylic. The analytical model yielded the following thermal resistance equation.

$$q''_{cond} = 5.2[T_w(x, y) - T_\infty] \frac{W}{m^2} \quad (4.3)$$

This analytical model, however, does not take into account any contact resistances between the different materials, assumes a backside heat transfer coefficient, and also assumes constant material properties over the expected temperature range. Therefore, a heat loss experiment was setup with the actual test setup to accurately measure this conduction heat loss. For this test, the inside of the channel was filled with fiberglass insulation to ensure that all the heat generated by the heaters was lost through the acrylic.

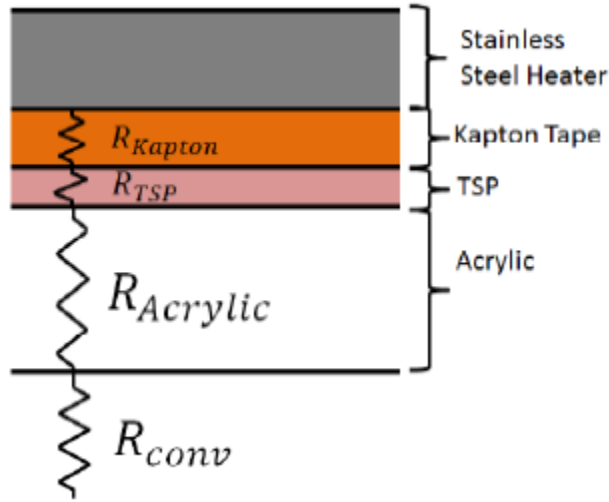


Figure 4.15: 1-Dimensional conduction loss diagram

Three different data points were measured at various heat inputs. To ensure steady state measurements, thermocouples on the test piece were monitored for any fluctuations. Typical times to reach steady state were approximately four hours. The test setup and the resulting data can be seen in Figure 4.16. From this data, the conduction loss term which is used in the MATLAB code is modified to the following equation.

$$q''_{cond} = 4.61[T_w(x, y) - T_\infty] \frac{W}{m^2} \quad (4.4)$$

Additional heat generated by the heaters is lost by radiation to its surroundings inside the test section. To evaluate this loss, another separate radiation loss test was performed. This test was similar to the conduction loss test, except that the fiberglass insulation in the test section was removed and instead the inlet and exit of the test section were covered in an attempt to limit the natural convection inside the channel. In order to evaluate the heat transfer from radiation, the conduction loss test data was used to subtract out the expected amount of heat lost through the acrylic.

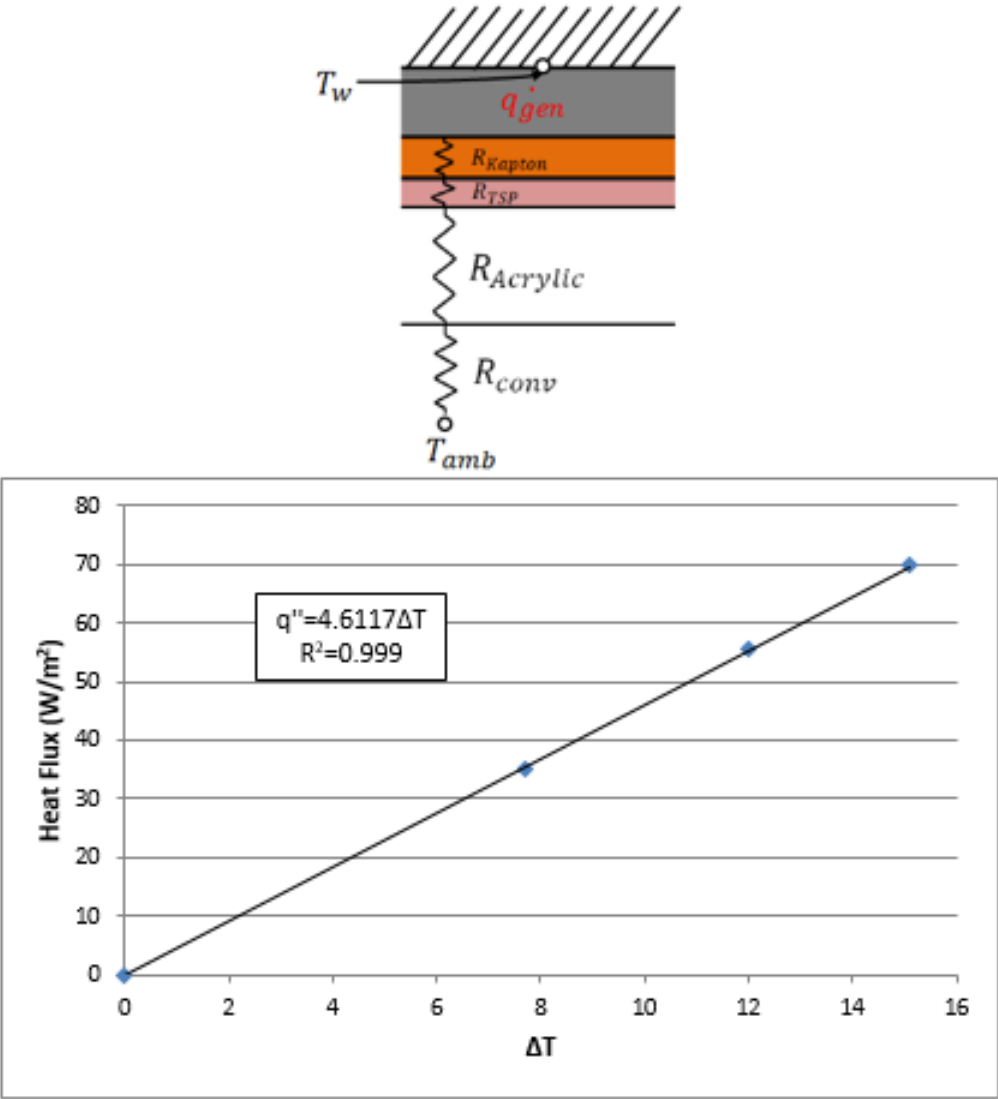


Figure 4.16: Conduction loss test setup (Top); Conduction loss test data (Bottom)

Three different heat input levels were evaluated to form a curve for the radiation heat loss, as shown in Figure 4.17. From this data, the following equation was used in the MATLAB post-processing code to account for the radiation loss at each point on the test surface.

$$q''_{rad} = 0.87\sigma[T_w^4(x, y) - T_{sur}^4] \frac{W}{m^2} \quad (4.5)$$

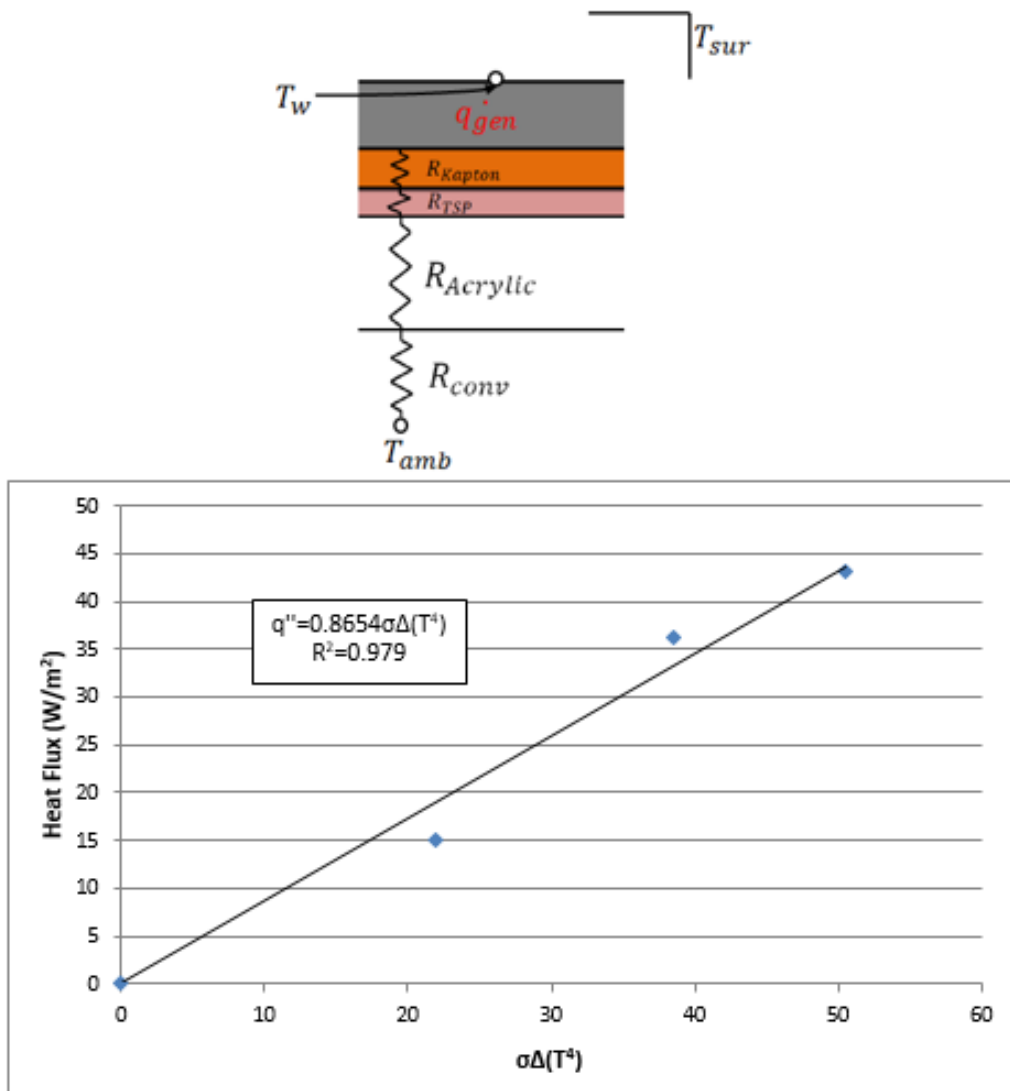


Figure 4.17: Radiation loss test setup (Top); Radiation loss test data (Bottom)

With this loss data, the heat transfer coefficient is then calculated using the equations below. The author understands that the equation for effective heat flux is technically not valid for the curved portion of the target plate, however due to the large curvature of the target plate the error in q'' is estimated to be $\pm 0.05\%$ which can be neglected.

$$q''_{eff} = q''_{gen} - q''_{cond} - q''_{rad} \quad (4.6)$$

$$h(x, y) = \frac{q_{eff}''}{T_w(x, y) - T_\infty} \quad (4.7)$$

For these tests, the measurement of T_w slightly varies from a pure definition of wall temperature at test conditions. This variation comes from the current testing method for taking the reference picture, as displayed in Figure 4.9, which is done with the wind-on. This causes the reference picture to capture some of the recovery temperature effects that occur at high Mach number flows. These effects come into play mainly for the highest Reynolds number case, in which these recovery temperature variations can see local changes of approximately 0.5 C. A more appropriate method for dealing with these Mach number effects would be to measure the recovery temperature distribution on the target plate itself under flow conditions with no heat input and use this as the driving temperature in the preceding equations in place of T_∞ . However, vibrations of the rig and the high signal to noise ratio when measuring such a small temperature change between the no flow reference picture and the recovery temperature cause implementation of this method to be difficult.

With the heat transfer coefficient, the Nusselt number can be easily calculated using the following equations. For the uniform array cases, only one jet diameter is present so the definition is straightforward.

$$Nu_{unif}(x, y) = \frac{h(x, y)D}{k_{air}} \quad (4.8)$$

For the non-uniform array cases, a definition for the characteristic length of the array is not so clear cut. It was decided that the diameter of the first six rows, which is constant, should be used as the characteristic length since this is the largest diameter in the array and these jets will dominate the heat transfer performance of the array.

$$Nu_{non-unif}(x, y) = \frac{h(x, y)D_1}{k_{air}} \quad (4.9)$$

Another point of interest was the region downstream of the impinging jets for both the uniform and non-uniform cases 4-6. For each case, it was important to note how the heat transfer in these regions compared to that of a fully-developed smooth channel at the same channel Reynolds numbers. For this comparison, the heat transfer correlation for turbulent flow in a smooth channel by Dittus-Boelter was used and is shown in the following equation.

$$Nu_{DB} = 0.023 Re_{D_h}^{4/5} Pr^{2/5} \quad (4.10)$$

Pressure and Flow Distribution

Pressure measurements at the orifice plate were used in the calculation of the total mass flow rate through the test section. The equations for the calculation of mass flow rate through an orifice plate can be found in ASME PTC 19.5 [42]. Additional pressure measurements were taken at each pressure tap, whose locations were described previously, with a Scanivalve pressure transducer and multiplexer system. At each of these locations, a set of 30 measurements were taken and averaged to get each data point. These measured pressures were used to calculate various quantities which will be discussed in the following sections.

Uniform Array

For the uniform array, the array average jet Reynolds number was used to characterize the flow through the system. This value was calculated using the following equation, with N being the total number of jets in the array.

$$Re_{j,avg} = \frac{4\dot{m}_{orifice}}{\pi N D \mu} \quad (4.11)$$

Using the pressure data at each jet row and the total temperature and pressure measurements in the plenum, the ideal jet velocity at each row was calculated using the following isentropic flow

relations.

$$T_i = \left(\frac{P_i}{P_{total}} \right)^{\frac{\gamma-1}{\gamma}} T_{total} \quad (4.12)$$

$$a = \sqrt{\gamma R_{air} T_i} \quad (4.13)$$

$$v_i = a \sqrt{\left[\left(\frac{P_{total}}{P_i} \right)^{\frac{\gamma-1}{\gamma}} - 1 \right] \frac{2}{\gamma-1}} \quad (4.14)$$

Using these velocities, calculated static temperatures, and measured static pressures, the ideal mass flow for each jet row could be calculated using the following equations. The factor of 6 is included in the calculation of area because of the 6 spanwise jets in each row.

$$\rho_i = \frac{P_i}{R_{air} T_i} \quad (4.15)$$

$$A = 6 \frac{\pi D^2}{4} \quad (4.16)$$

$$\dot{m}_i = \rho_i v_i A \quad (4.17)$$

Using these calculated mass flows for each row and the mass flow calculated through the orifice plate, an array averaged discharge coefficient was calculated.

$$C_d = \frac{\dot{m}_{orifice}}{\sum_{i=1}^6 \dot{m}_i} \quad (4.18)$$

With this discharge coefficient, an actual jet velocity could then be calculated for each row.

$$v_{i,actual} = C_d v_i \quad (4.19)$$

Finally, with the actual jet velocities calculated, the local jet to average jet mass flux and local crossflow to jet mass flux ratios for each row "n" could be calculated using the following equations.

$$\left. \frac{G_j}{G_{j,avg}} \right|_n = \frac{\rho_n v_{n,actual}}{\frac{1}{6} \sum_{i=1}^6 \rho_i v_{i,actual}} \quad (4.20)$$

$$\left. \frac{G_c}{G_j} \right|_n = \frac{\frac{\pi/4}{(Y/D)(Z/D)} \sum_{i=0}^{n-1} \rho_i v_{i,actual}}{\rho_n v_{n,actual}} \quad (4.21)$$

Non-Uniform Array

Similar quantities were calculated for the non-uniform array as with the uniform array, however with some slight differences to make the Original and Restricted geometries comparable. First, the characterization of flow through the array was chosen to be represented by the first row Reynolds number. Previous works using non-uniform arrays had chosen to use an average diameter of all jets as a characteristic length for Re and Nu definitions, however, this does not have any physical meaning. For this reason, and to be able to compare the different geometries at similar upstream flow rates, the first row Reynolds number was used. Using the same isentropic flow relations and definition of discharge coefficient as shown in the previous section, the first row Reynolds number was calculated as follows. The only difference in the calculations comes from the varying areas for each row, since each row has a different jet diameter or, for the 14th row, only four jets instead of seven.

$$Re_1 = \frac{4C_d \dot{m}_{orifice}}{\pi N_1 D_1 \mu} \quad (4.22)$$

For a similar reason as to why the first row Reynolds number was used, the local jet to

average jet mass flux ratio equation was modified to a local jet to first row jet mass flux ratio.

$$\left. \frac{G_j}{G_{j,1}} \right|_n = \frac{\rho_n v_{n,actual}}{\rho_1 v_{1,actual}} \quad (4.23)$$

The local crossflow to jet mass flux ratio equation provided in the previous section was used, unmodified, for the non-uniform array as well.

$$\left. \frac{G_c}{G_j} \right|_n = \frac{\frac{\pi/4}{(Y/D)(Z/D)} \sum_{i=0}^{n-1} \rho_i v_{i,actual}}{\rho_n v_{n,actual}} \quad (4.24)$$

To characterize the pressure loss in the channel for cases 4-6 the static pressure distribution just downstream of the jets, where the ribs are located, is measured and the friction factor is calculated. The experimental friction factor is defined according to the following equations, with v_b being the bulk velocity in the channel and dP/dx being the calculated pressure gradient.

$$v_b = \frac{\dot{m}_{orifice}}{\rho_{avg} A_c} \quad (4.25)$$

$$D_h = \frac{2HW}{(H + W)} \quad (4.26)$$

$$f = \frac{2 \frac{dP}{dx} D_h}{\rho_{avg} v_b^2} \quad (4.27)$$

For a comparison of these calculated friction factor values to that of a fully developed smooth pipe, a baseline friction factor value was calculated using the Blasius correlation. The ratio of the experimental values and this correlation value were then compared to obtain a friction factor augmentation value for each case.

$$f_0 = \frac{0.046}{Re^{1/5}} \quad (4.28)$$

$$\text{Friction factor augmentation} = \frac{f}{f_0} \quad (4.29)$$

Uncertainty

Uncertainty for the Nusselt and jet Reynolds number was calculated through an analysis of the governing equations and the measurands taken, with reference to [43], which favors ASNI/ASME PTC 19.1. Figure and Figure show the error sources in the Nu and Reynolds number calculations, respectively. Rather than use intermediate calculations (i.e. propagating error through the branches of the uncertainty tree), the absolute error of each measured variable can be multiplied by a sensitivity index and combined in a final root-sum-square step to simplify calculations. With the equations written as functions of only the measurands and constants used, a sensitivity index for each variable is obtained by taking the partial derivative of the governing equation with respect to the variable. The individual uncertainties are then combined via root-sum-squared calculations for a total uncertainty of the result.

The uncertainty for Nu, calculated using the analytical approach above along with precision data from five separate test runs, is reported as 9.4% of the result at a 95% confidence level, taking into account the student t-score factor. The actual data's standard deviation as shown in Figure 4.21 (with the test data plotted in Figure 4.20) validates the uncertainty analysis calculation. The downstream data for the straight section is believed to have lower standard deviation due to the limitations in the lighting of the TSP. Since there are limited sources of illumination, and the curved portion covers a larger area than the straight section, the achieved intensities for testing are greater for the straight section and thus a greater signal-to-noise ratio is achieved for these pictures. For the same test data, the uncertainty of the jet Reynolds number is reported as 2.5% of the result at a 95% confidence level, also reflective of student t-score inclusion.

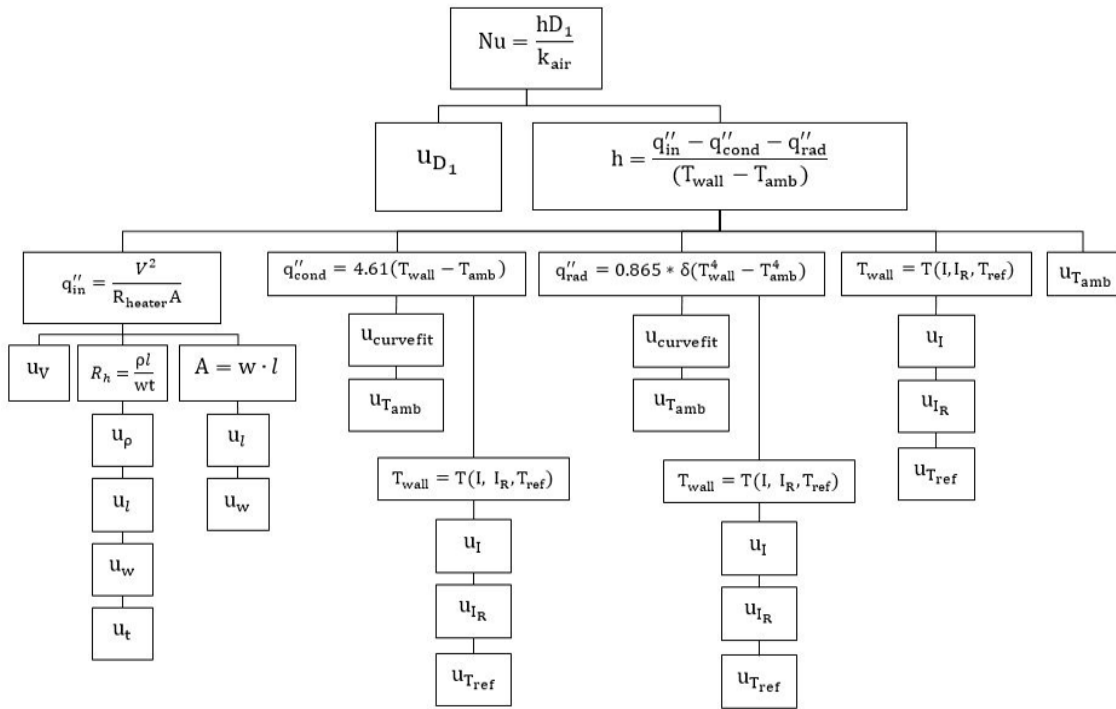


Figure 4.18: Nusselt number uncertainty tree

The standard deviation of the experimentally obtained Reynolds number is 0.71% of the average, again validating the uncertainty analysis calculation.

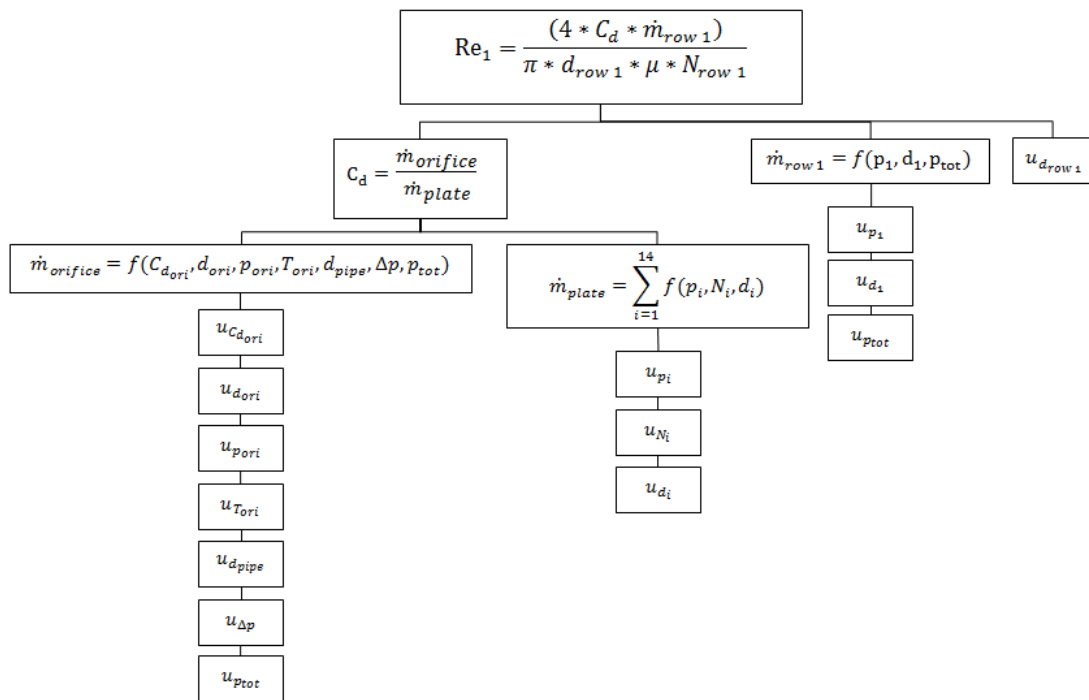


Figure 4.19: Reynolds number uncertainty tree

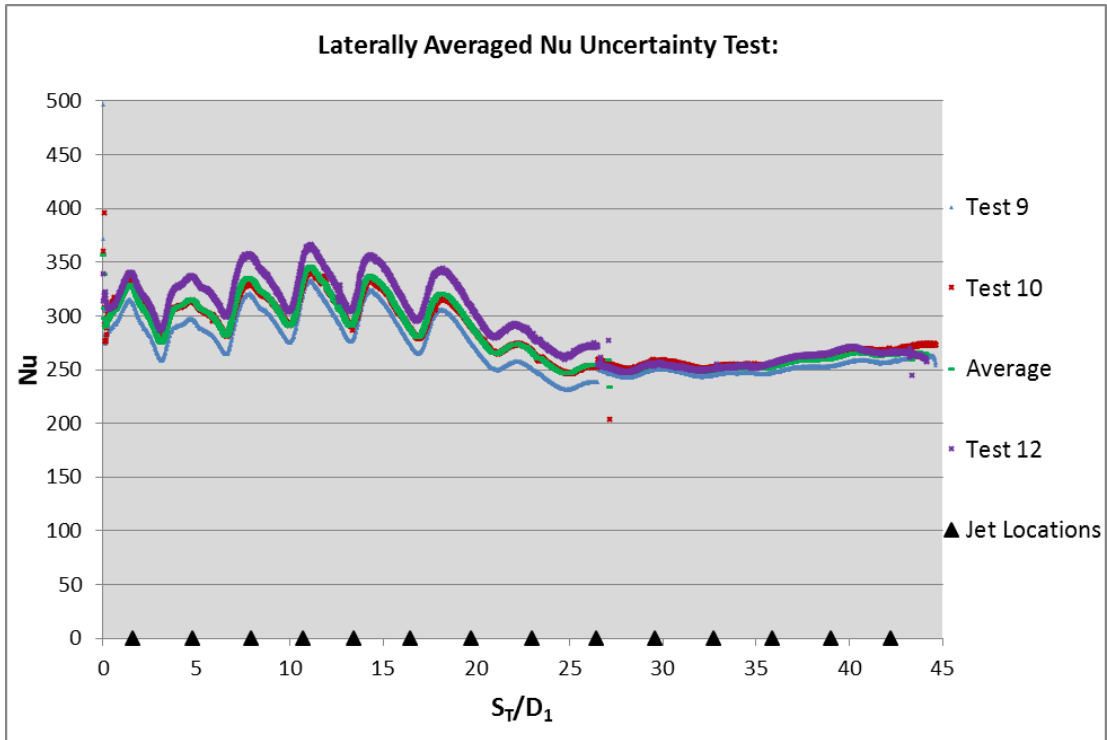


Figure 4.20: Laterally averaged Nusselt numbers from repeatability tests

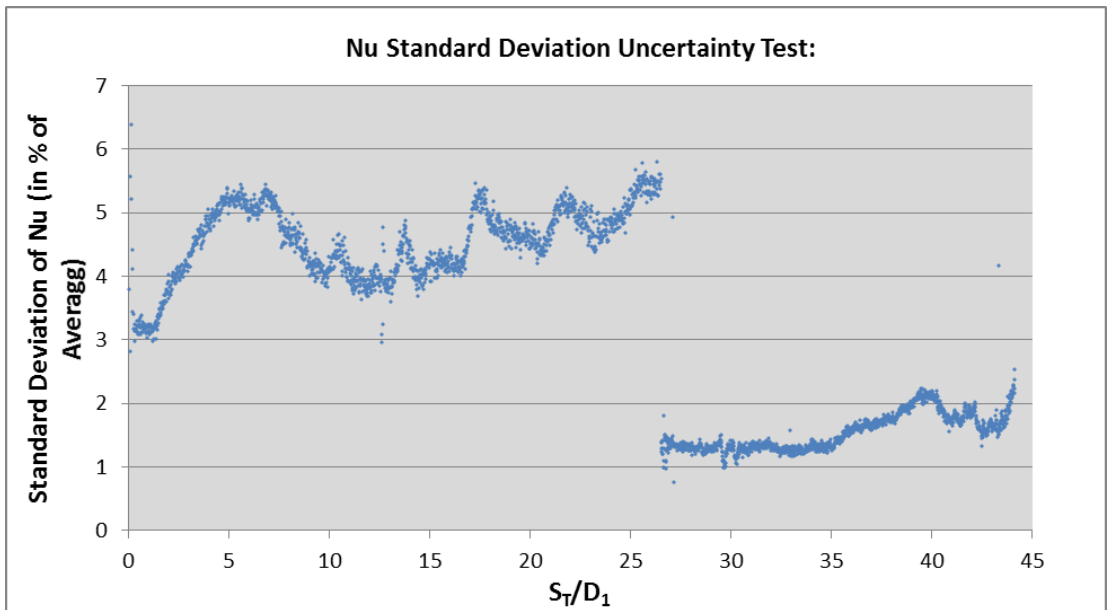


Figure 4.21: Standard deviation of Nusselt numbers in repeatability test

CHAPTER 5: COMPUTATIONAL SETUP

For engineering predictions of turbulent flows a fast, efficient, accurate solution is desirable. Most predictions of jet impingement heat transfer involve the use of standard or modified versions of the $k - \epsilon$ turbulence model, available in all existing CFD packages. These models have usually been developed, calibrated and validated using flows parallel to the wall. Physical phenomena involved in impinging flows on a solid surface are substantially different and have been considered as highly challenging test-cases for the validation of turbulence models. In an attempt to find the best numerical turbulence for predicting flow behavior in jet impingement, steady RANS models were preferred based on computational efforts required.

All the calculations were performed using a commercial CFD solver: Star-CCM+. Based off of the literature mentioned in the previous sections, the $k - \epsilon v^2 - f$ turbulence model was chosen for these calculations. A RANS type eddy viscosity model was selected for two reasons: first, they are less computational expensive than more advanced models such as Reynolds stress models (RSM) and large eddy simulation (LES) models; and second, the aim of the study was to investigate the time-averaged heat transfer in an impinging jet configuration, so instantaneous fluctuating values were not important to resolve. A second order discretization method was used in the simulations and a segregated flow and fluid temperature solver were used for all the calculations.

Domain and Grid

ANSYS ICEMCFD is used for mesh generation. The numerical domain is divided into three subsections; inlet and plenum chamber (Fluid 1), rectangular prism region above the jet plate, jet plate and target plate (Fluid 2) and outlet pipe (Fluid 3). Fluid 1 and 3 have unstructured grids with while fluid 2 has a structured grid. The rectangular prism region just above the jet plate is generated to have better control on the grid size near the jet plate.

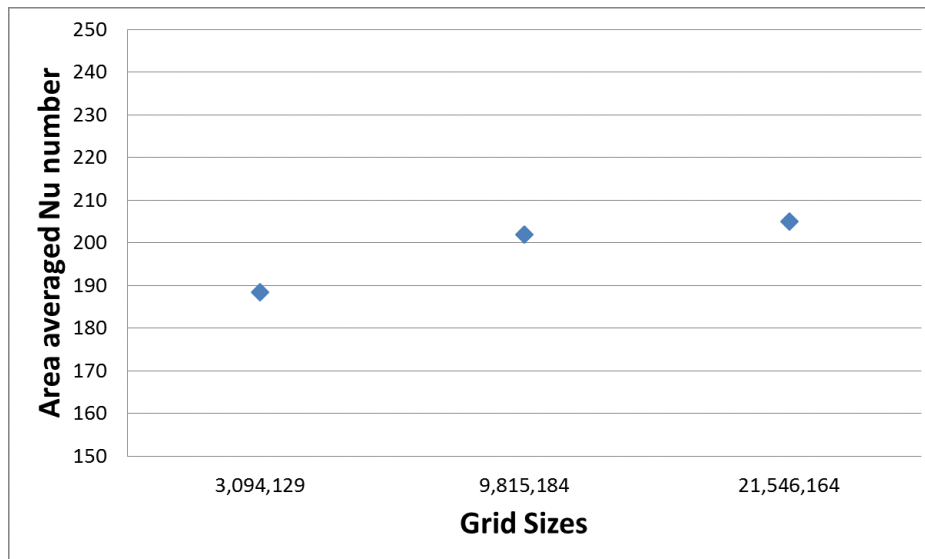


Figure 5.1: Grid convergence study at $Re_1=50,000$

To ensure the capability of precisely capturing fluid behavior and heat transfer, the grid is produced in a way that the first cell height is held $y^+=1$ on the heat transfer surface. Very fine grids were used near the jet shear layer, jet cores and near the target wall region. The meshing methodology is to mesh edges with proper expansion ratios, focusing resolution towards regions of large gradients in velocity and temperature, specifically the near wake region. Cell orthogonality was ensured by applying O-grid type blocks for all jets. The edge meshes were then mapped to faces which were extruded through the volumes.

For the non-uniform array case, three different grids were generated for the same computational domain. These grids contained ~ 3 million, ~ 10 million, and ~ 22 million cells. A grid convergence study was performed using these various grids and is shown in Figure 5.1. A final grid size of 9.8 million was chosen, as the variation in area averaged Nu from 9.8 million to 21.5 million was less than 2%. Of the final cell count of 9.8 million, about 9 million of these cells are used in the fluid 2 area. Figure 5.2 shows a side-view of the computational domain. The structured mesh on the jet plate is shown in Figure 5.3.

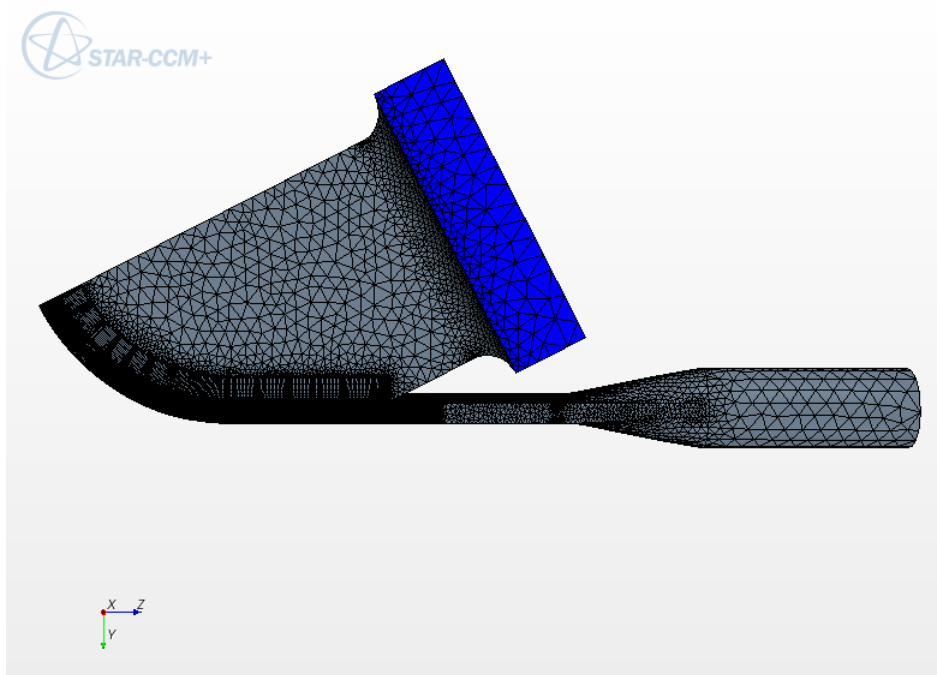


Figure 5.2: Side-view of computational domain

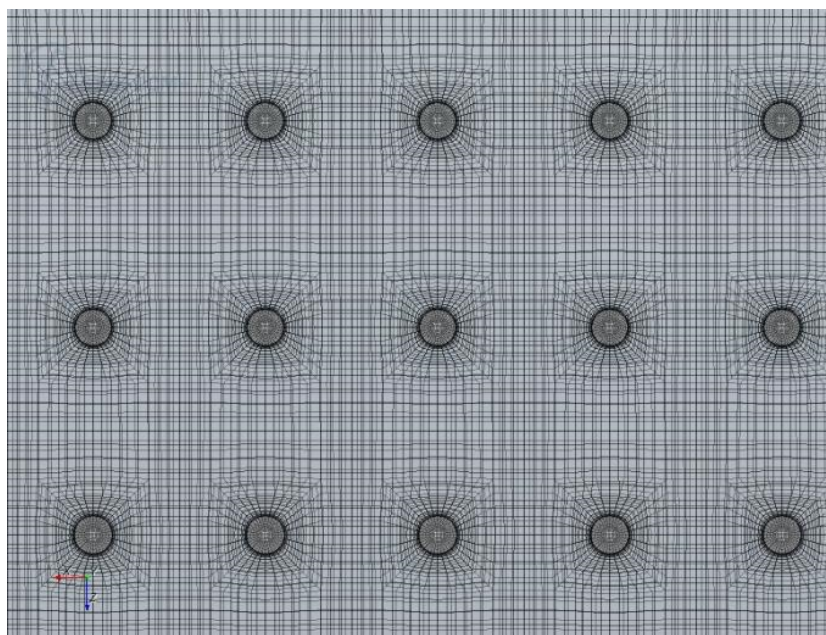


Figure 5.3: Structured mesh on jet plate

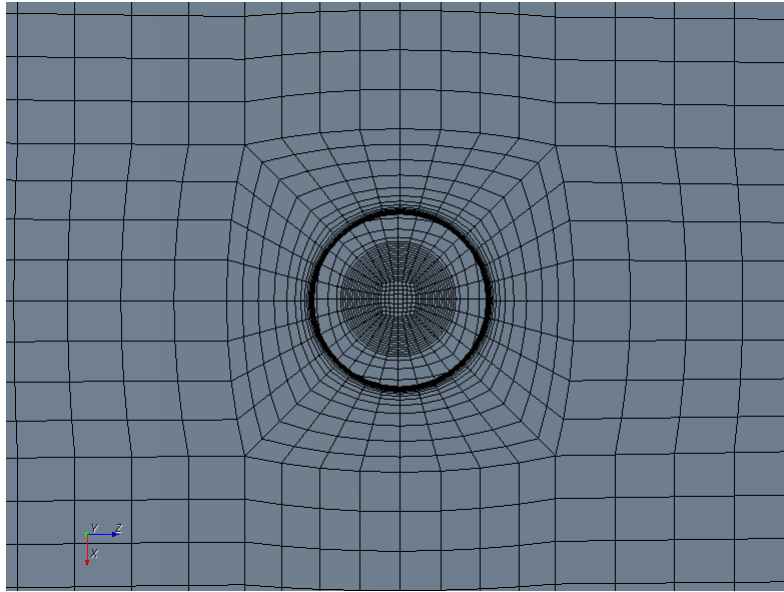


Figure 5.4: Structured mesh in and around a jet hole

Boundary Conditions

The test section inlet is considered as a stagnation inlet where known total temperature and total pressure are given. Plenum chamber walls, jet plate and outlet pipes are all considered as no slip, adiabatic, impermeable walls. The target plate is also simulated as a no slip, impermeable wall and, to account for the heat flux generated by the heaters, a constant heat flux boundary condition is applied to the TSP area on the target plate and the value of heat flux is updated in each case according to the experimental quantities. Pipe outlet is specified as a pressure outlet with a target mass flow. This allows for the model to adjust the pressure at the outlet until the desired mass flow is achieved, which is input into the software to match the experimental measurements.

CHAPTER 6: UNIFORM ARRAY RESULTS

The first results analyzed are the uniform array results. As stated previously, this study was performed to observe any potential effects that a large-radius test section and target plate could have on the flow distribution and heat transfer from an impingement array. Additionally, the geometrics of the array were chosen for comparison with previous work by Florschuetz et al. [14].

Flow Distribution

It is tested whether the curvature of the target plate has any effect on the pressure loss in the channel. One way to evaluate any possible effect is to look at the jet flow distribution. The sidewall pressure taps and aforementioned equations were used to evaluate any possible impact the curvature of the target plate has on the jet flow distribution in the channel. Figure 6.1 displays the local jet to average jet mass flux ratio distribution for the flat case while Figure 6.4 shows the local jet to average jet mass flux ratio distribution for the curved case. Figure 6.3 displays the local crossflow to jet mass flux ratio distribution for the flat case while Figure 6.4 shows the local crossflow to jet mass flux ratio distribution for the curved case. It is evident from these figures that the curvature does not have a significant effect in altering the pressure drop and thus the flow distribution in the channel. Both the plane and curved case vary from $\sim 98\%$ of the average jet mass flux at the first row to $\sim 103\%$ at the last row. This shows how the pressure gradient in the channel leads to higher jet Reynolds numbers in the streamwise direction. Due to their being only 6 rows of jets in the array and the geometric spacings of the channel, the crossflow levels remain fairly low with the maximum crossflow mass flux being only $\sim 28\%$ of the local jet mass flux. Additionally, as described in many other works, such as Florschuetz et al. [14], the Reynolds numbers is seen to have no effect on the flow distribution in the impingement channel for a constant geometry.

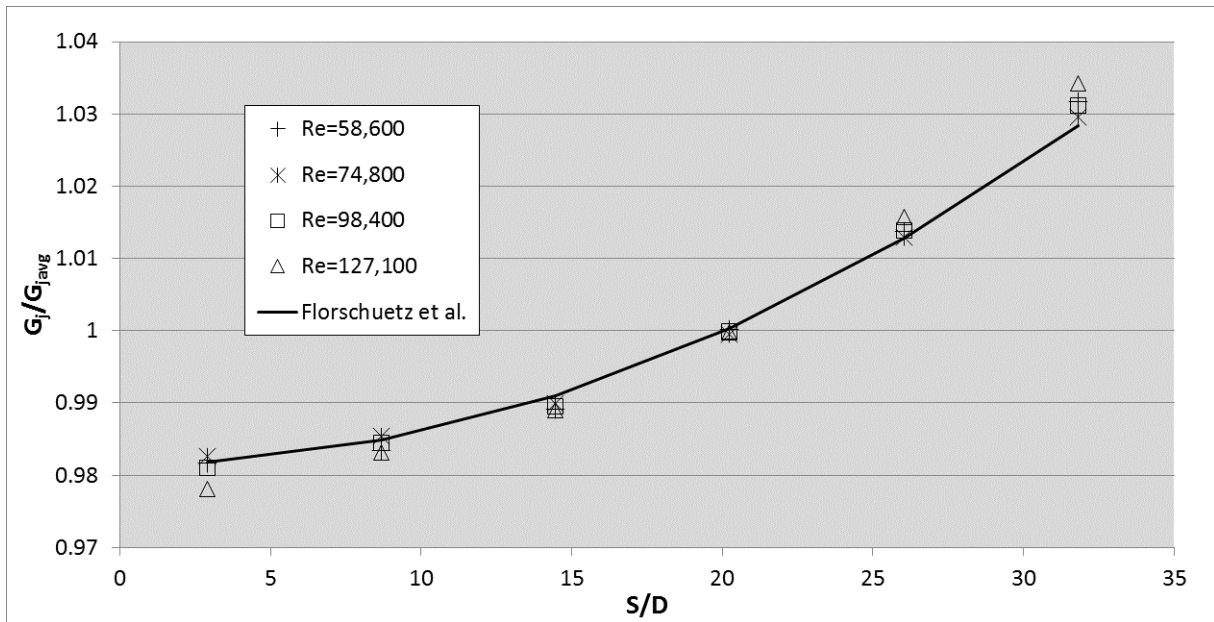


Figure 6.1: Local $G_j/G_{j,avg}$ distribution for uniform array flat target plate case

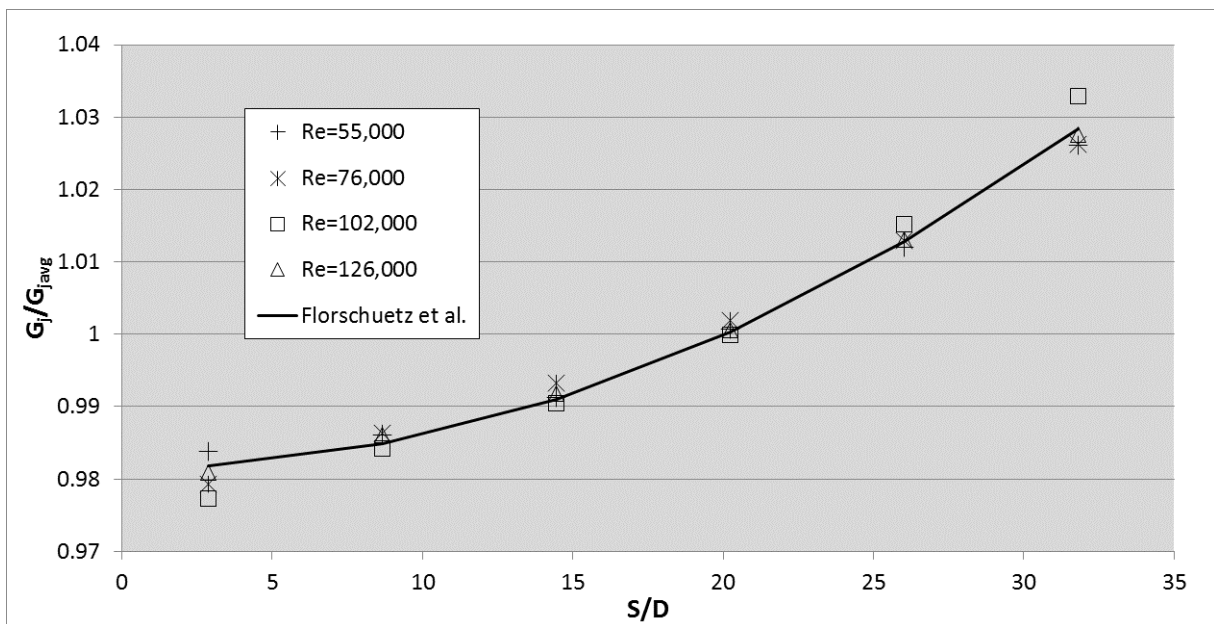


Figure 6.2: Local $G_j/G_{j,avg}$ distribution for uniform array curved target plate case

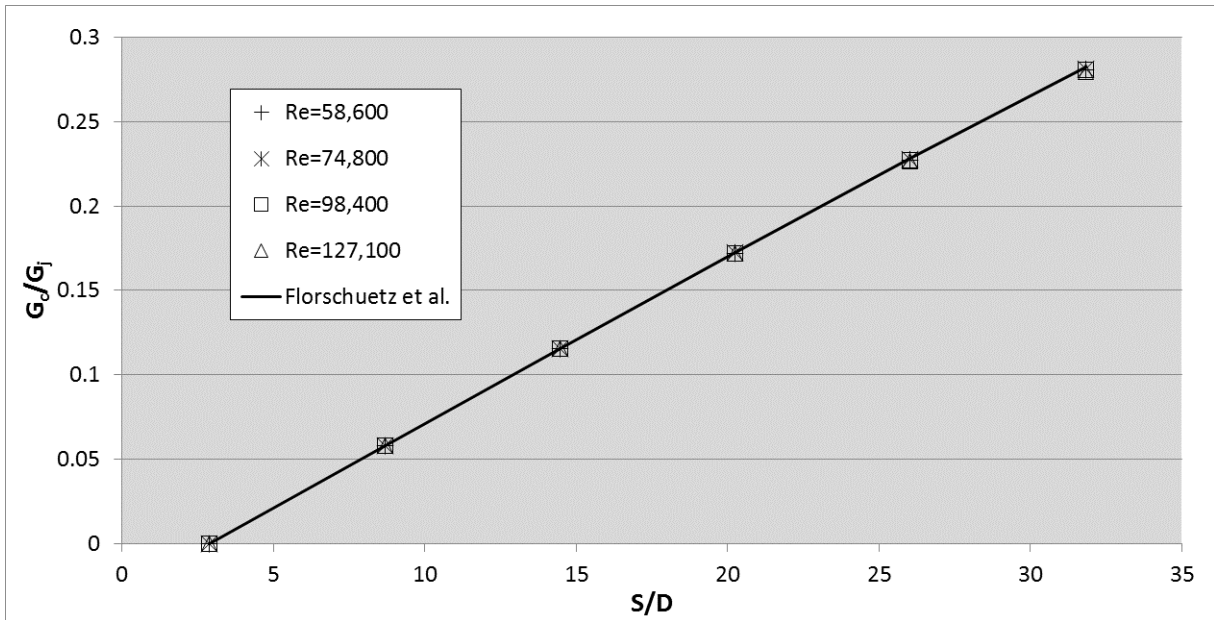


Figure 6.3: Local G_c/G_j distribution for uniform array flat target plate case

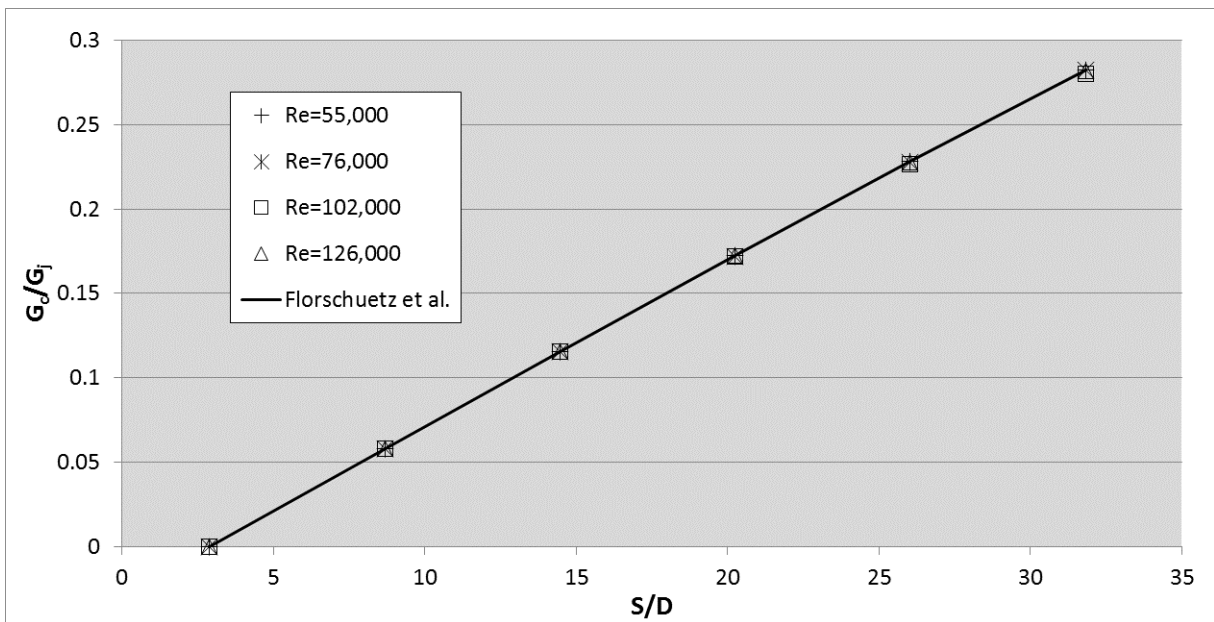


Figure 6.4: Local G_c/G_j distribution for uniform array curved target plate case

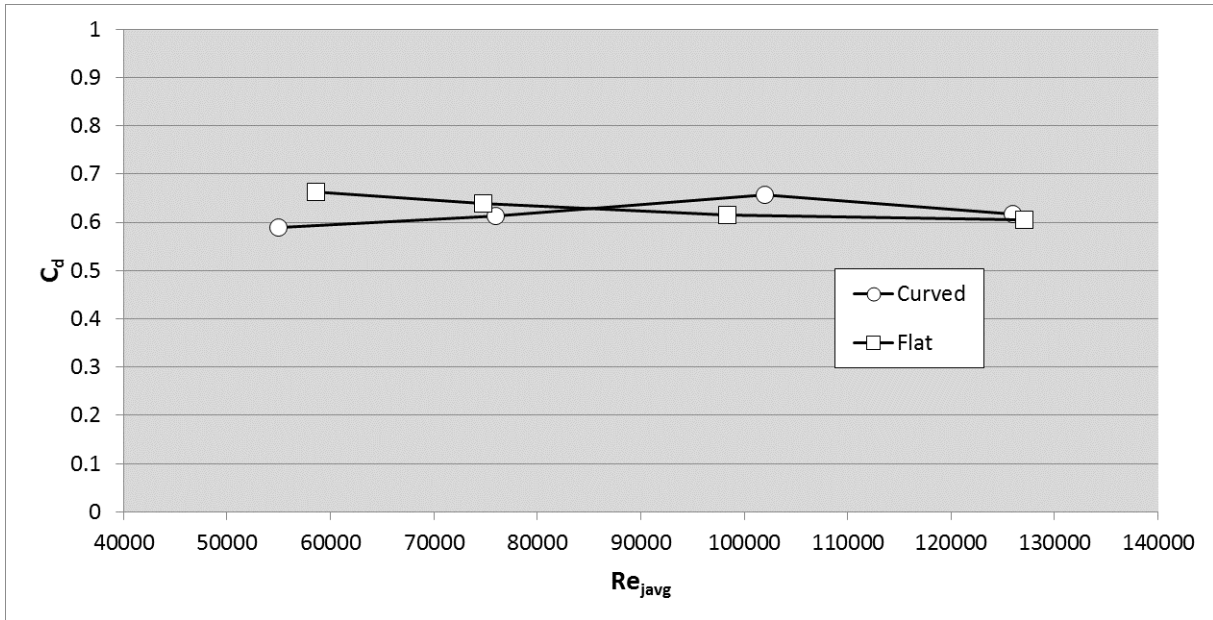


Figure 6.5: Array average discharge coefficients as a function of Reynolds number for uniform array case

The equations developed by Florschuetz et al. are also seen to agree with the measured data, as the slight variations shown in the figures are within the uncertainty for the experiment.

For all tests run, an array-average discharge coefficient was calculated and then used for the flow distribution calculations. The maximum Mach number for any of the tests was measured to be ~ 0.3 , at the last row for the highest Reynolds number runs. Therefore this method of using an array-average discharge coefficient was deemed suitable. The discharge coefficients was measured to be in the range 0.6-0.65 for all cases, as seen in Figure 6.5. As the jets were sharp-edged and had $L/D=0.21$, the discharge coefficients are considerably lower than values seen in most other literature. At these values of L/D , the jet holes are similar to an orifice plate, and by comparing these measured values to typical values in ASME PTC 19.5 [42], it can be seen that these are typical discharge coefficient values for an orifice plate geometry.

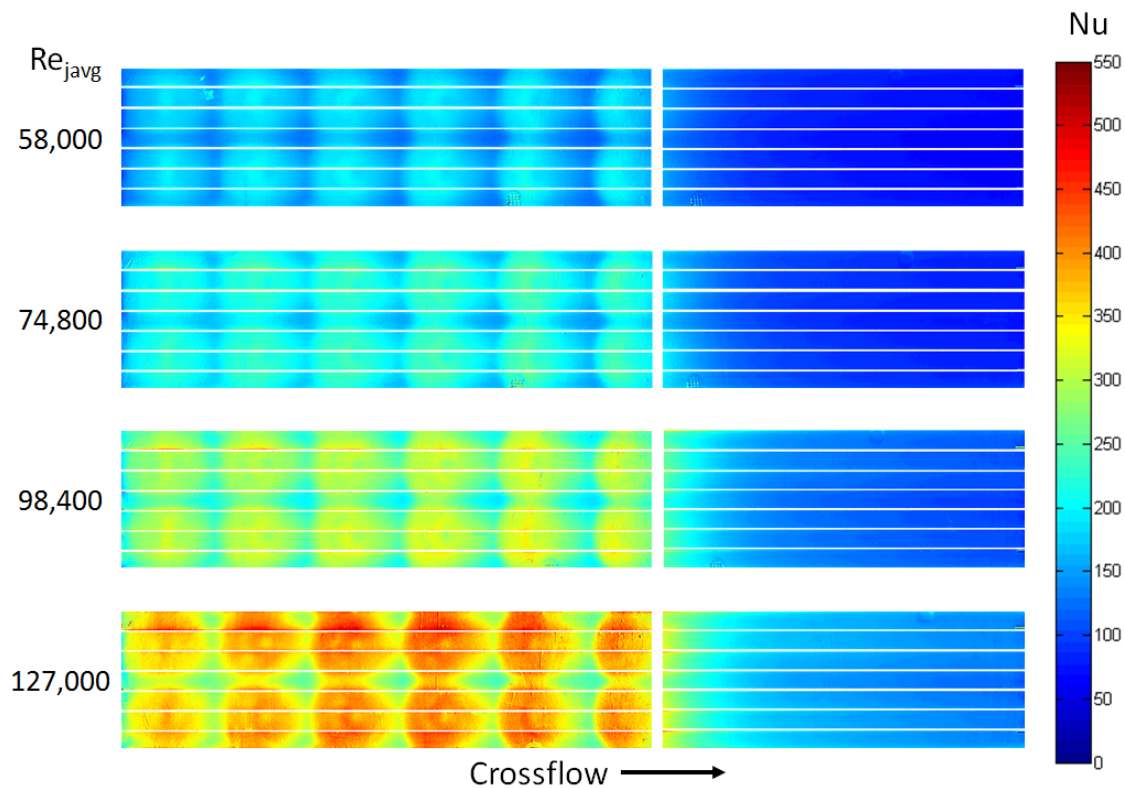


Figure 6.6: Nusselt number profiles for uniform array flat target plate case

Heat Transfer

The target wall Nusselt number profiles for all flow rates are shown in Figure 6.6 for the flat case and Figure 6.7 for the plane case. The horizontal gaps in the data are the regions in-between the heater strips which have been cropped out. For both the flat and curved cases, the trends remain constant with increased Reynolds number, as expected, with only increases in magnitudes. For both the curved and plate profiles it appears that the crossflow does not significantly affect the heat transfer on the target plate until the fourth row of jets, with the sixth row showing large deformation and the typical kidney shaped stagnation region as shown in other high crossflow studies. It is also clearly evident from these profiles that the heat transfer levels and trends are similar for both the flat and curved cases.

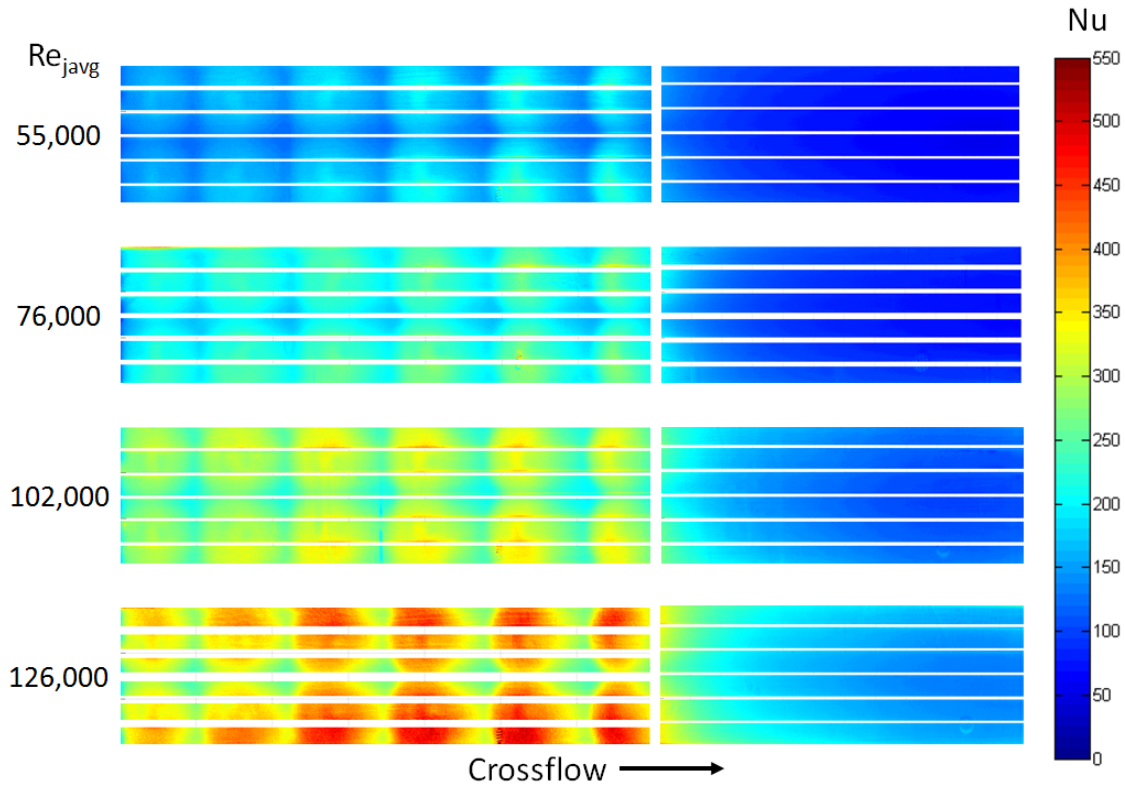


Figure 6.7: Nusselt number profiles for uniform array curved target plate case

Lateral averages for all cases were done by averaging the Nusselt profiles in the spanwise direction and plotting them in the streamwise direction. Figure 6.8 shows laterally averaged Nusselt numbers for the flat case while Figure 6.9 shows laterally averaged Nusselt numbers for the curved case. The laterally averaged values for the post-impingement area for $24.5D$ are also displayed. Similar trends and levels can clearly be seen between the flat and curved case. These figures also show that the peak stagnation Nusselt number values slightly increase in the streamwise direction. This implies that the effects from the continually strengthening jet cores in the streamwise direction, shown by the $G_j/G_{j,avg}$ plots in Figures 6.1 and 6.2, outweigh the detrimental effects of crossflow. This is not surprising as the G_c/G_j values in the channel are relatively low with a maximum of 28%.

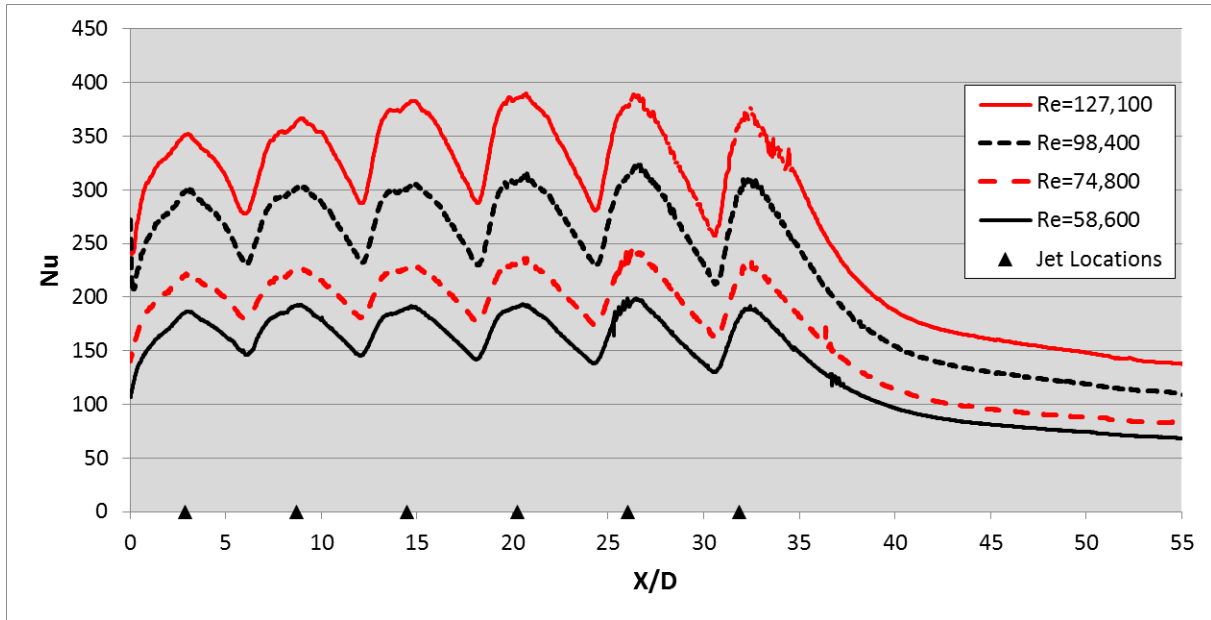


Figure 6.8: Laterally averaged Nusselt numbers for uniform array flat target plate case

However, these increasing peak values could also be caused by diffusion of the downstream jets by the crossflow, possibly due to vortex shedding, causing them to affect a larger area. Another attribute of note in these plots is that of apparent secondary peaks which can be seen on the second to fourth jet rows. It is thought that these peaks are formed by a secondary stagnation region between the crossflow and the wall jet of the downstream row, causing a horseshoe vortex to form around the upstream part of the jets in these rows.

Oftentimes, of more importance for a designer are the row averaged Nusselt number values of the array. The values for the current study are plotted and compared against values from the correlation by Florschuetz et al. [14] in Figure 6.10 at an average jet Reynolds number of 55,000 and in Figure 6.11 at an average jet Reynolds number of 100,000. In the downstream regions, the results were also compared against the Dittus-Boelter correlation to evaluate the heat transfer decay. For both flat and curved cases, the downstream regions show higher levels than those predicted by Dittus-Boelter.

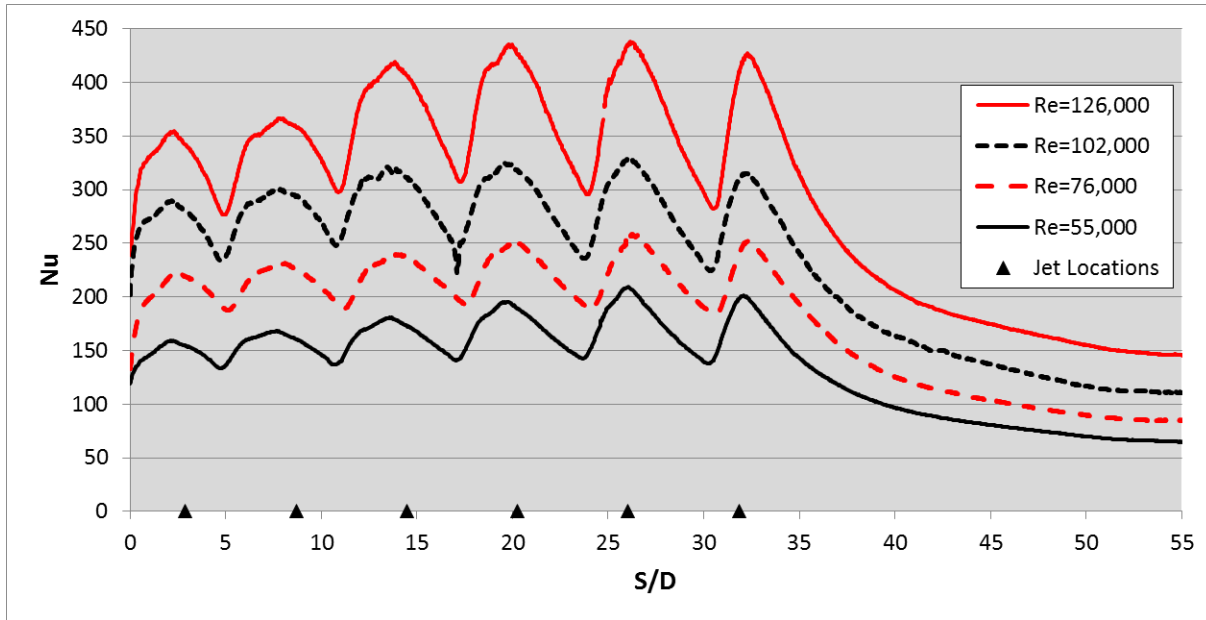


Figure 6.9: Laterally averaged Nusselt numbers for uniform array curved target plate case

Both the flat and curved cases show a downstream heat transfer level that is approximately a factor of 1.5 times that of the Dittus-Boelter prediction. These increased levels over Dittus-Boelter can be expected since the measured area is still in the developing region for the flow, and the flow in this impingement channel is expected to have increased levels of turbulence. In the impingement region, it is clear that the flat and curved cases show very similar results at both Reynolds numbers. Additionally, the $Re_{j,avg}=55,000$ flat and curved cases shows values somewhat similar to the Florschuetz prediction with all values falling within 20% of the correlation values. The trends, however, do not appear to match with the correlation. It appears that the correlation over-predicts the detrimental effects of crossflow on the heat transfer of the downstream jet rows. The $Re_{j,avg}=100,000$ cases shows similar trends except that the correlation from Florschuetz et al. appears to be under-predicting the level of heat transfer from the array with discrepancies over 30%; an expected result since these jet Reynolds numbers far exceed the limits of the correlation.

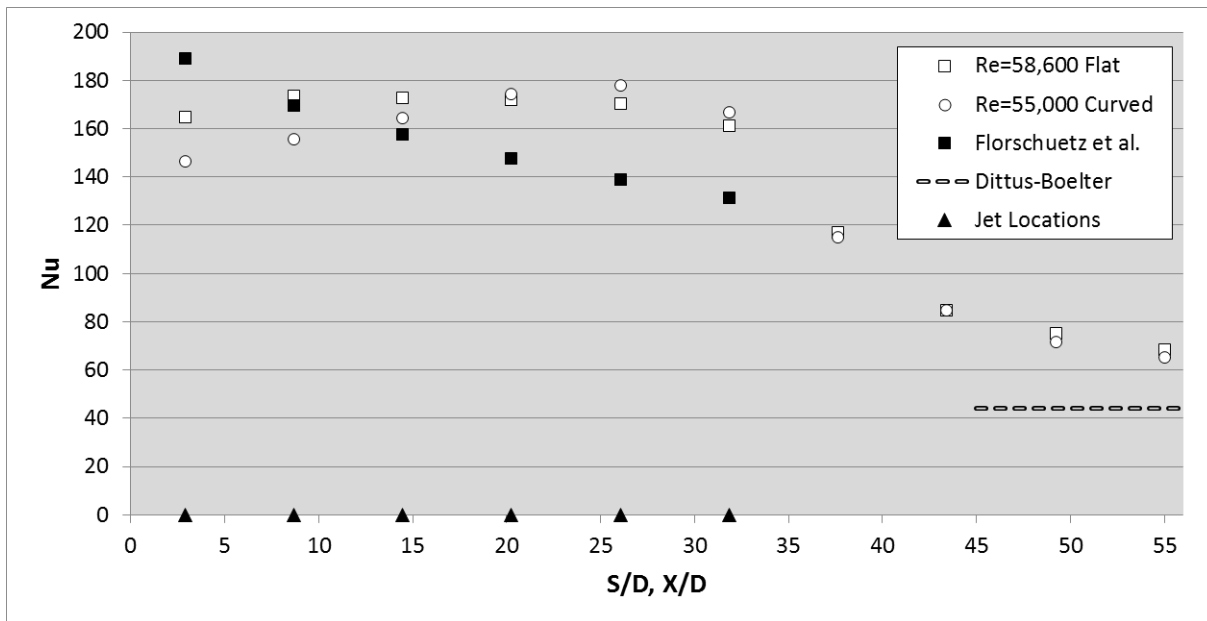


Figure 6.10: Row averaged Nusselt number comparison for uniform array at $Re_{j,avg}=55,000$

This discrepancy for the $Re_{j,avg}=55,000$ case could potentially be explained by the different L/D used compared to Florschuetz et al. The low L/D used for this experiment causes the discharge coefficients to be significantly different from those seen by Florschuetz et al, 0.6 compared to 0.8. This variation could cause significant differences in the turbulence and momentum distributions of the jets.

For another comparison, the array averaged Nusselt numbers for all cases were calculated and compared in Figure 6.12. These results show the nearly identical level and trend of Nu versus average jet Reynolds numbers for flat and curved cases. It is also evident from this graph that the Nu level from the arrays is within uncertainty to that predicted by Florschuetz et al. [14] at $Re_{j,avg}=55,000$ which is the only jet Reynolds number from the current study which falls within the scope of that tested by Florschuetz et al. From this data, it was calculated that the curved case showed to be proportional to Re raised to the power 0.92, while the plane case was proportional to the power 0.9. Florschuetz et al. predicts a value of 0.69 for this Reynolds sensitivity power.

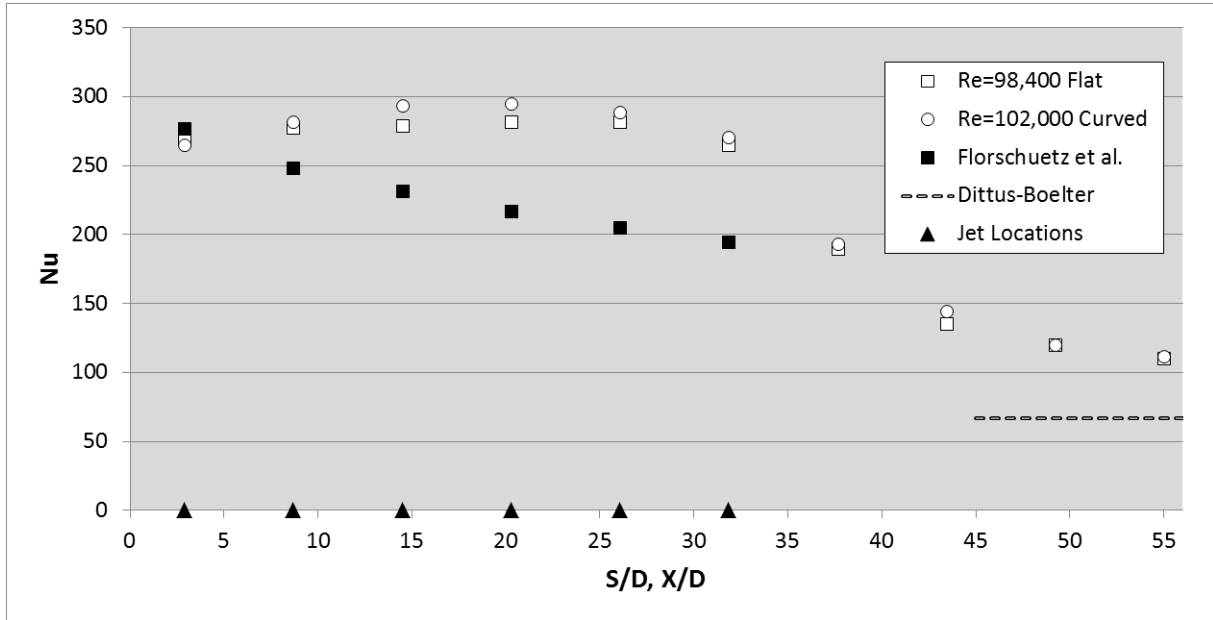


Figure 6.11: Row averaged Nusselt number comparison for uniform array at $Re_{j,avg}=100,000$

This shift in Reynolds sensitivity could be caused by several factors, including the smaller L/D values in the array mentioned perviously and the fewer number of jet rows in the study. All arrays tested by Florschuetz et al. contained 10 jet rows and therefore these arrays all had more affects from crossflow. In the current cases, crossflow levels remain low and therefore most of the jets act as independent single impinging jets. By looking at previous works on single impinging jets without crossflow, it was found that some reported Reynolds number sensitivity values of 0.8 or greater which match well with the current data.

This data clearly shows that the large radius curvature target plate does not have a significant effect on the heat transfer from the jet array. It is apparent that the radius of the target plate is too large to lead to any significant differences in the flow structures. Furthermore, the Taylor-Gortler vortices, which were hypothesized to potentially increase the heat transfer of the array, do not appear to form in the boundary layer on the target plate. The chaotic flow inside the jet array does not allow the formation of these vortices in the boundary layer.

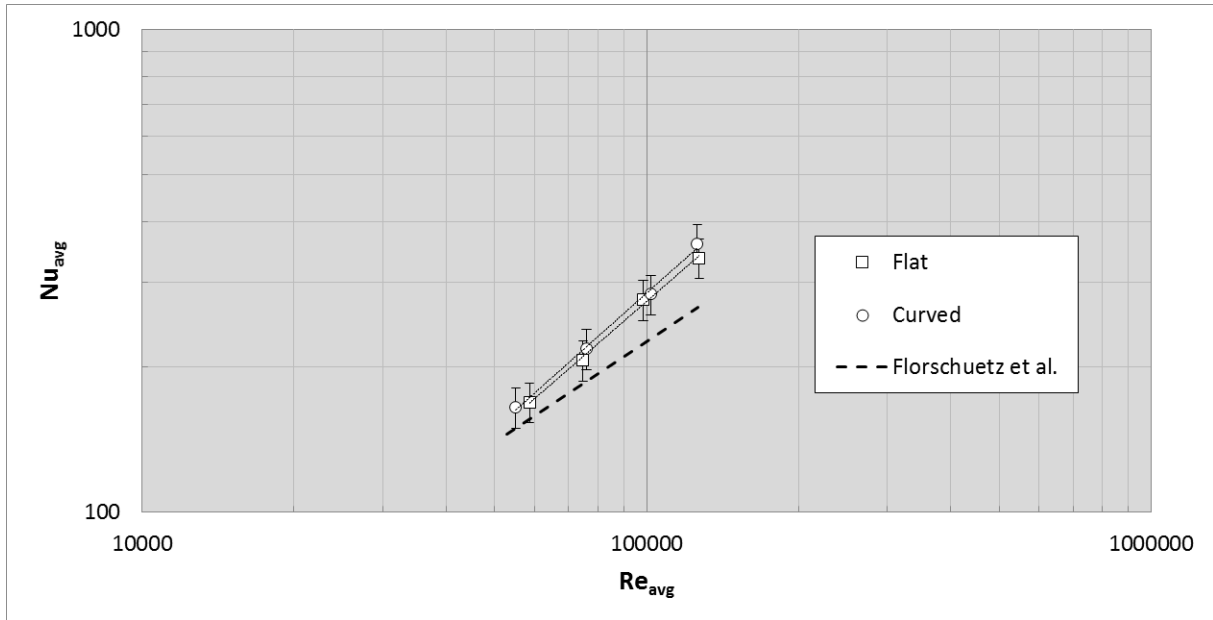


Figure 6.12: Area averaged Nusselt number comparison for uniform array

This is reflected in the work by [41], who found that once the turbulence in the mainstream flow increased from 0.2% to 3%, the Taylor-Gortler vortices were no longer seen to coalesce.

Computational Results

Alongside the experimental work, a computational model was created for the curved target plate case and ran to evaluate the ability of a steady RANS turbulence model ($v^2 - f$) to predict the heat transfer characteristics of jet array impingement on a curved target plate. The laterally averaged Nusselt number results from the CFD prediction can be seen in Figure 6.13 and 6.14. As reported by many other studies, the CFD over-predicts the stagnation Nusselt number values. Interestingly, it does appear that the CFD correctly predicts the presence of secondary Nu peaks at the second to fourth jet rows. Furthermore, the model matches the experiment in that the peak Nusselt number values continually increase from row to row in the streamwise direction. Also, the CFD predicts well the downstream shifts in the Nusselt number peaks caused by the crossflow.

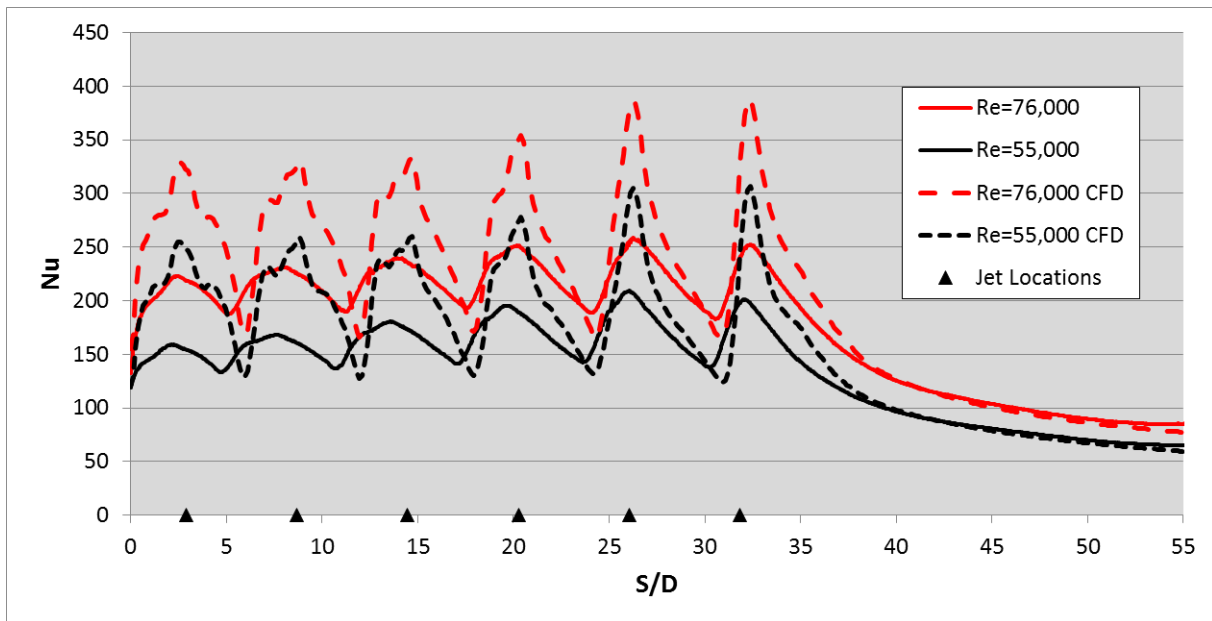


Figure 6.13: Comparison of experimental and computational results for laterally averaged Nusselt number at $Re_{j,avg}=55,000$ and $Re_{j,avg}=76,000$

The row averaged values for the CFD predictions are compared against the experimental results in Figure 6.15 and 6.16. At the lower Reynolds numbers, there is some discrepancy between the results, with the CFD over-predicting the the first row Nu values by 30% for the $Re_{j,avg}=55,000$ case and 27% for the $Re_{j,avg}=76,000$ case. Although these values decrease to 16% and 18%, respectively, by the sixth row. The higher Reynolds number runs show much closer results, with the first row Nu predictions being at 20% greater than the experiment with most values being within 10%. This shows that the CFD does not correctly predict the Reynolds number sensitivity of the Nusselt number results for the array.

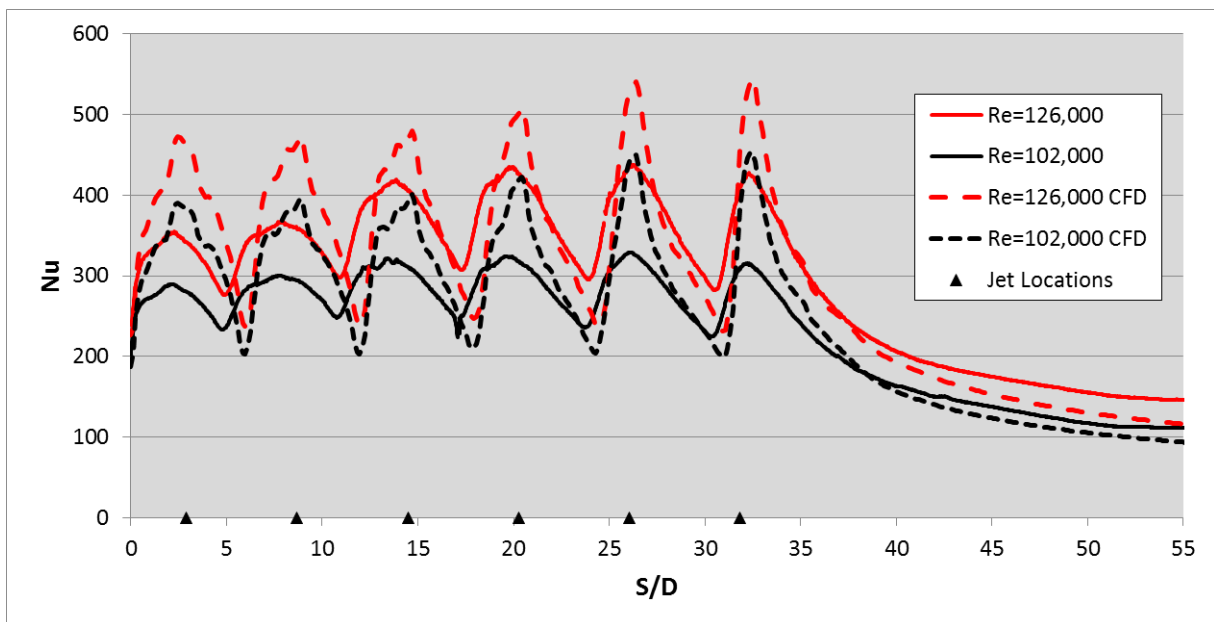


Figure 6.14: Comparison of experimental and computational results for laterally averaged Nusselt number at $Re_{j,avg}=102,000$ and $Re_{j,avg}=126,000$

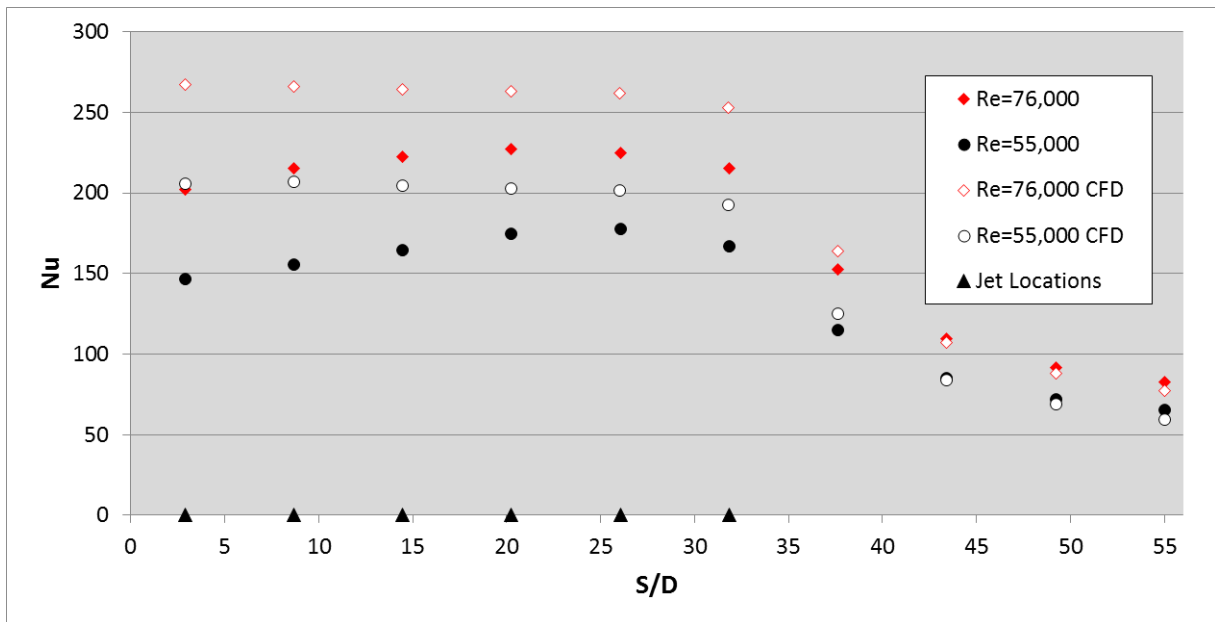


Figure 6.15: Comparison of experimental and computational results for row averaged Nusselt number at $Re_{j,avg}=55,000$ and $Re_{j,avg}=76,000$

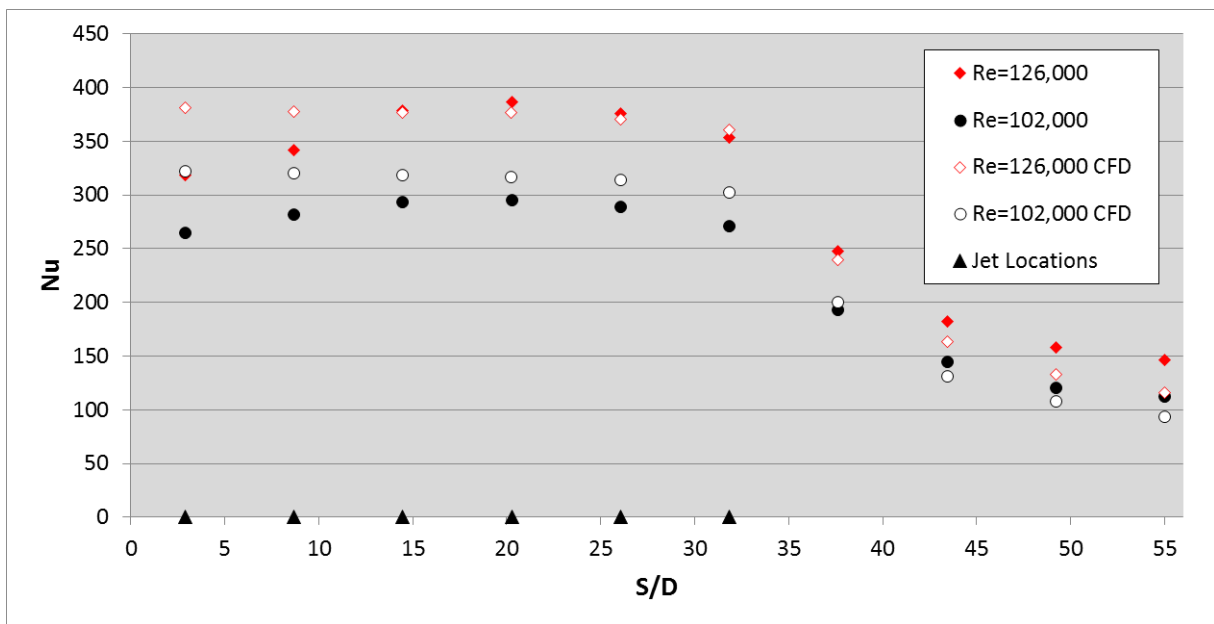


Figure 6.16: Comparison of experimental and computational results for row averaged Nusselt number at $Re_{j,avg}=102,000$ and $Re_{j,avg}=126,000$

CHAPTER 7: NON-UNIFORM ARRAY RESULTS

The non-uniform impingement array analyzed is representative of a geometry used for cooling of a gas turbine combustor. The varying geometry of the current impingement plate can be tuned and used for several reasons: non-uniform heat load on part, more efficient use of cooling air, control of flow to downstream locations. The following results show the heat transfer and pressure drop performance of the given non-uniform geometry and compare this performance with the use of two different ribbed geometries in place of several of the downstream rows.

Flow Distribution

For each run, an array-average discharge coefficient was calculated. The discharge coefficient was measured to be in the range 0.65-0.68 for all cases. These low discharge coefficients can be attributed to the small L/D of 0.16-0.29 in the present study. The static pressures measured on the jet plate, as mentioned in the previous sections, are presented in Figure 7.1 as a pressure ratio, relative to the total pressure measured in the test section plenum. These measurements were used to calculate all further flow parameters displayed in this section. These results clearly show the non-linear nature of pressure drop cost relative to flow rate, as the pressure drop of for Case 3 is approximately 30 times higher than that of Case 1 even though the flow rates are only different by a factor of approximately 3.

One important flow parameter which dictates the local heat transfer performance is the local channel mass flux to jet mass flux ratio, which is displayed in Figure 7.2. These results show nearly identical trends for Cases 1-3, which agrees with previous literature that states that the flow distribution of the channel is only a function of the geometric spacing of the impingement jet holes. There is a steady increase in crossflow build-up until row 8, at which point the gradient decreases.

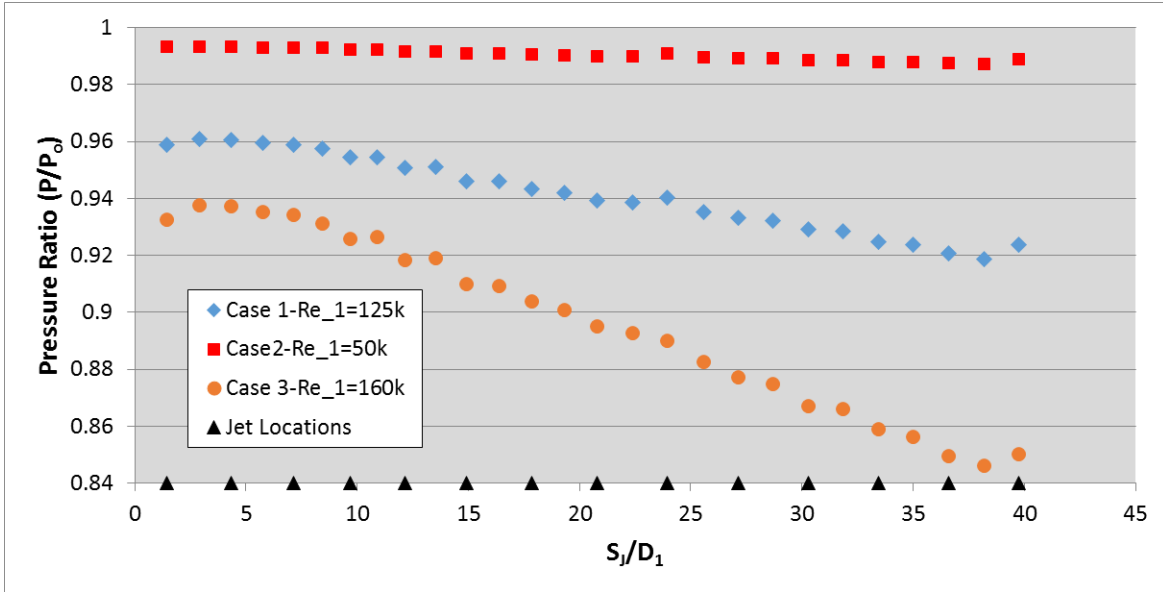


Figure 7.1: Pressure ratio profile for non-uniform array cases 1 to 3

This is due to the drop in jet diameter and the subsequent drop in jet mass flow from row 7 onwards.

The local jet mass flux to average jet mass flux ratio was also calculated in order to evaluate how the flow through individual jet rows varies in the channel; the results are shown in Figure 7.3. From this data, we can see that local jet mass flux varies by a maximum of $\sim 20\%$ relative to the average. As was described previously, information in the open literature states that the flow distribution in the channel is unaffected by varying flow rates, as is reflected in the data.

Due to the complex layout of the jet plate holes, an array-averaged jet Reynolds, as seen in other impingement literature, could not be used without using non-physical length scales and velocities. Because of this, the local Reynolds number was calculated for each row, using the local properties and jet diameter. The local jet Reynolds number distribution for each flow rate measured for case 3 is plotted in Figure 7.4. The jet Reynolds number increases from row 1-6 due to the constant jet diameter for these rows along with the pressure drop in the channel. The sharp drop in local jet Reynolds number at row 7 can be attributed to the decrease in jet diameter at this location.

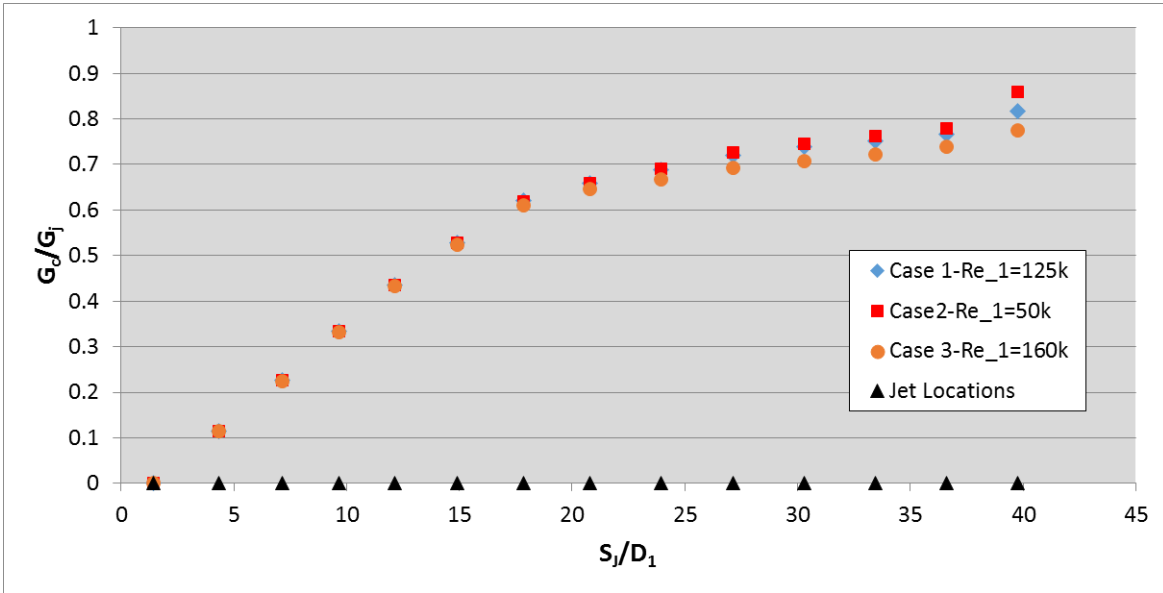


Figure 7.2: Local G_c/G_j distribution for non-uniform array cases 1 to 3

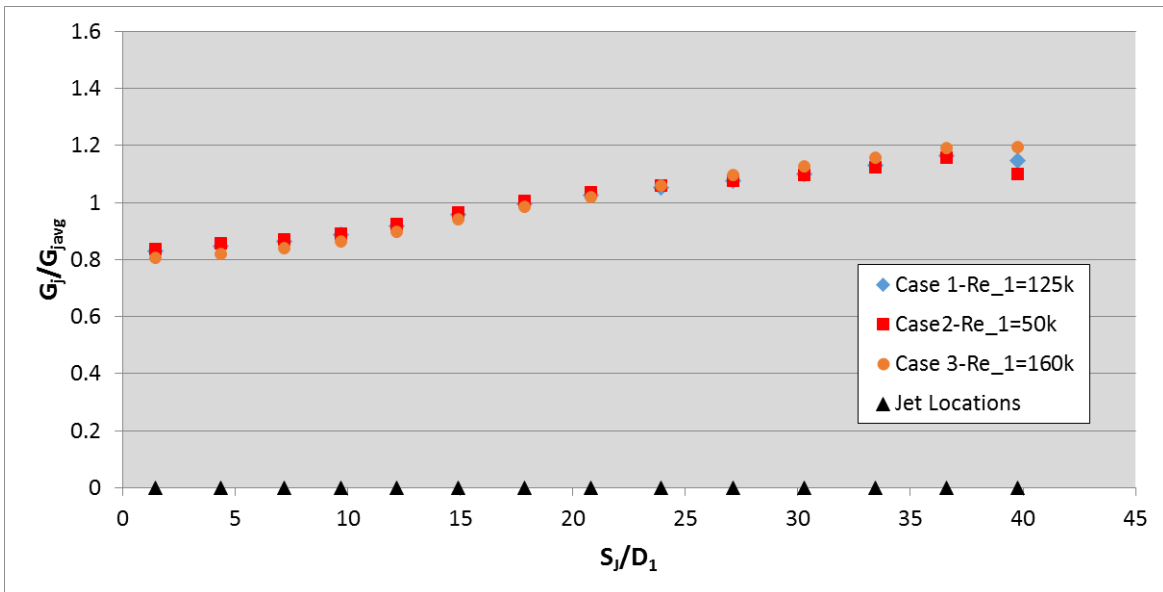


Figure 7.3: Local $G_j/G_{j,avg}$ distribution for non-uniform array cases 1 to 3

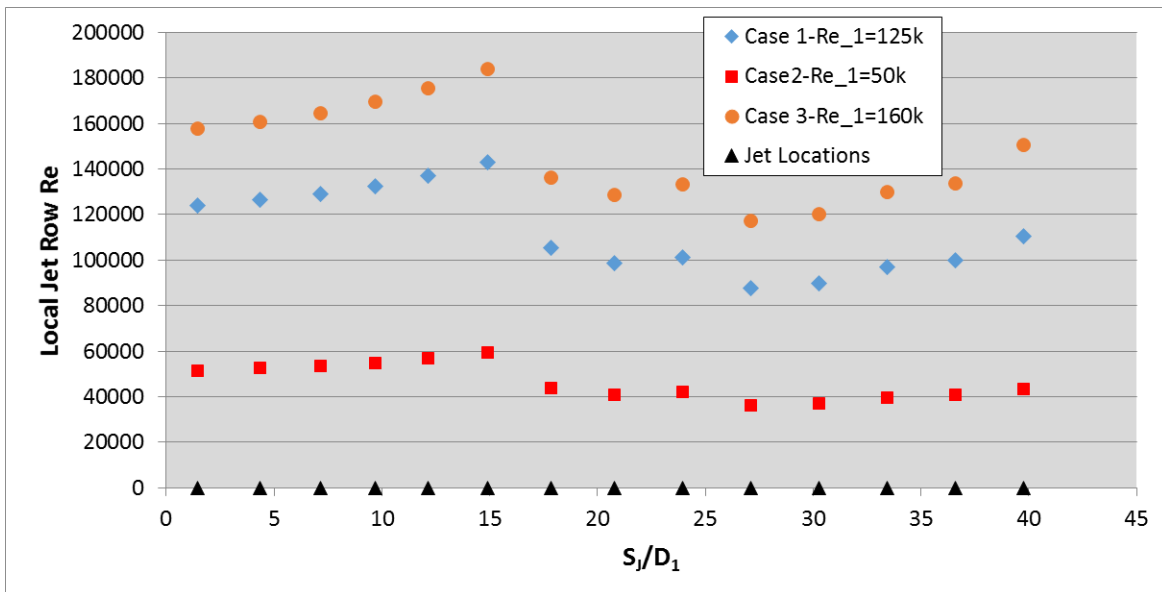


Figure 7.4: Local jet Reynolds number distribution for non-uniform array cases 1 to 3

As reported in other impingement studies, the trends in flow distribution are not affected by the Reynolds numbers.

The aerodynamic effect of blocked jets and the ribs at the downstream are presented as a pressure ratio in Figure 7.6 for Case 1, 4, 5 and 6. These test cases were run at a first row Reynolds number of 125,000. The distribution of pressure gradient (dP/dS) represents the pressure loss in the system. It is apparent that the upstream section, which included the first 9 rows of jets, of all the cases revealed a similar trend in pressure drop. This shows that the addition or removal of downstream rows does not affect the upstream rows. It is shown that pressure loss is highest for Case 1 among all the cases. Between Rib 1 and Rib 2, Rib 2 shows lower pressure drop than Rib 1. The pressure loss is least for case 4 as expected where the downstream jets are blocked and channel forms a smooth duct.

To characterize the pressure loss in the channel for cases 4-6 the friction factor is calculated and compared to that of smooth channel flow.

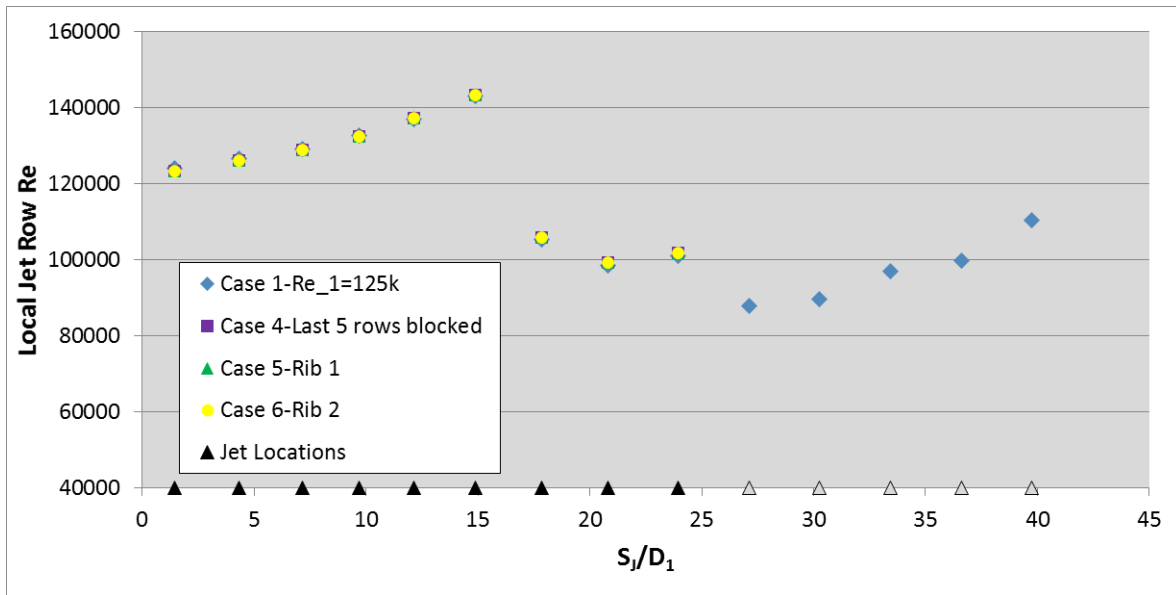


Figure 7.5: Local jet Reynolds number distribution for non-uniform array cases 1 and 4 to 6

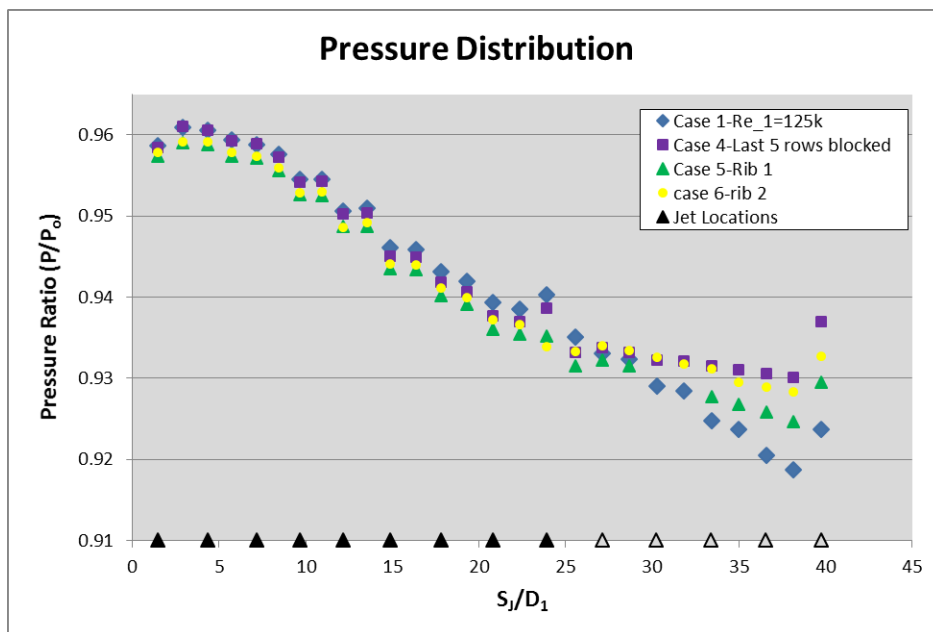


Figure 7.6: Local jet Reynolds number distribution for non-uniform array cases 1 and 4 to 6

Since the blocked jets or rib effects for the above cases took place at the downstream section of the channel, the friction factor is calculated using the pressure gradients from $S/D = 25.5$ which represents the location of the beginning of where the downstream jets are blocked. It is apparent that the addition of turbulator has an impact on pressure drop in the channel, and the 90 degree ribs will cause more pressure drop compare to the W-shaped ribs. For case 4, even though it is smooth channel flow, friction factor is still 4.95 times larger compare to the correlation which represents the friction factor in the fully developed region of a smooth pipe. The reason of this augmentation is that the channel flow is still in the developing zone and the effects from the upstream impingement jets still exist. For case 5 and case 6, there is no surprise that the friction factor augmentations are larger than case 4 since ribs play a role in increasing surface roughness.

Table 7.1: Friction factor augmentation for cases 4 to 6

Re_1	Case	f	f/f_0
125,000	4	0.01625	4.95
	5	0.03768	11.48
	6	0.029	8.75

Heat Transfer

The heat transfer on the target plate was measured for the middle three jets of the non-uniform array. The Nusselt number profiles can be seen in Figure 7.7. Crossflow appears to not have a significant effect until the 5th jet row, with the 6th row showing large deformation and a reduced stagnation region. From the 7th row onwards, the stagnation regions are difficult to distinguish. The reduction in jet hole diameter, and thus mass flow, starting at the 7th row is the cause of this.

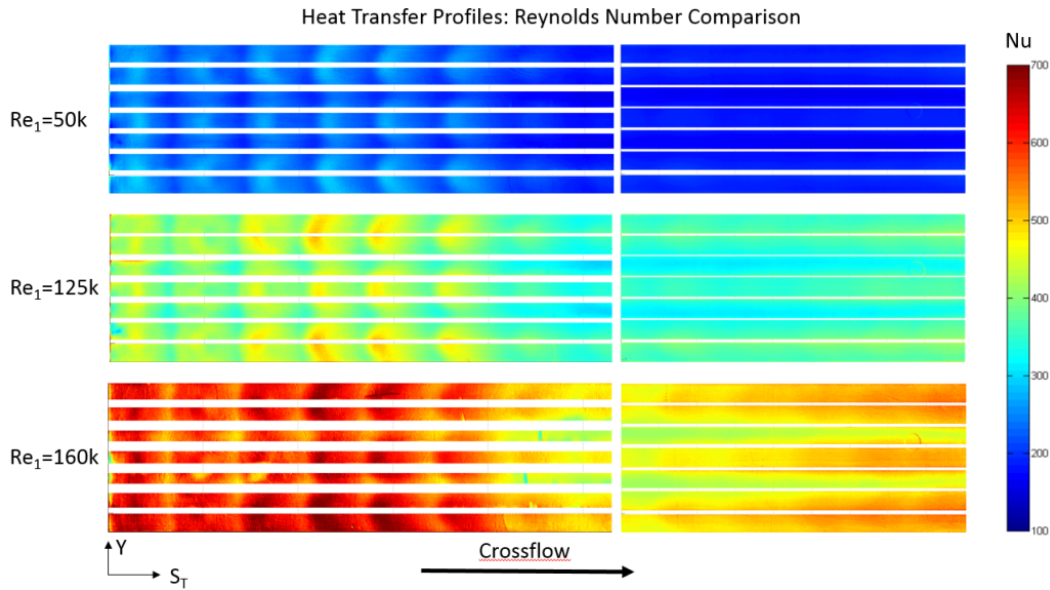


Figure 7.7: Nusselt number profiles for non-uniform array cases 1 to 3

Although the individual stagnation regions cannot be identified in the downstream area, it is interesting to note the streamwise-oriented bands of low heat transfer which form in the spanwise spaces between jets, showing a thinning of the boundary layer by the jets. This heat transfer stratification is also seen by Bailey and Bunker [15] for extended arrays.

The laterally averaged Nusselt number values for case 3 were calculated and are shown in Figure 14. It is evident from this figure that the trends in the heat transfer profile are independent of Reynolds number. This graph also shows the clear drop in stagnation point heat transfer starting at the 7th row, along with the downstream shift of stagnation points. By the 6th jet row, the stagnation point has been shifted an entire streamwise pitch downstream. Additionally, increasing Nu values are seen at the exit of the channel as caused by the high-velocity crossflow interacting with the downstream jets.

Oftentimes for large impingement arrays such as in this study, streamwise pitch averaged data are of more importance rather than fully-resolved heat transfer data for a designer. Figure 15 shows the streamwise pitch averaged data for case 3.

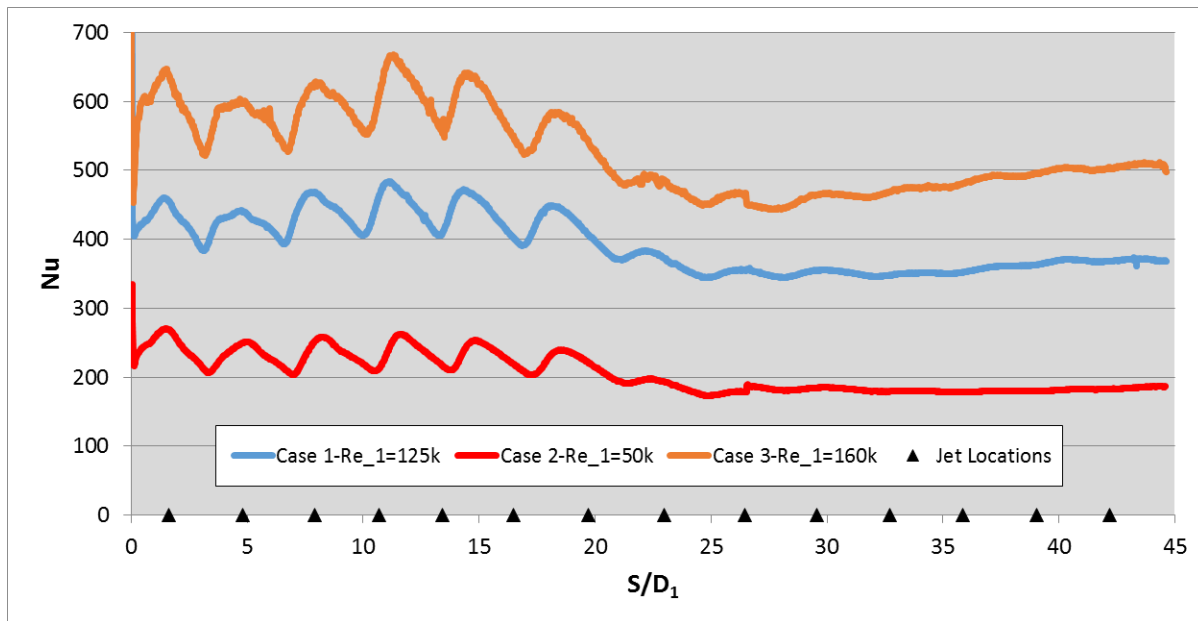


Figure 7.8: Laterally averaged Nusselt numbers for non-uniform array cases 1 to 3

From this graph, the non-monotonic behaviour of the heat transfer profile is clear. Similar behaviour is noted by Florschuetz et al. [14] and Bailey and Bunker [15] for dense arrays. Another observation is the relative uniformity in Nu throughout the domain at an elevated level. Pitch averaged results show a 25% shift from the maximum value at row 4 to the minimum value at row 9, with most values within a tighter spread. Similar uniform arrays studied by [6] show shifts of over 40% in pitch averaged Nu from the 1st to 10th rows.

The ability of established correlations to correctly predict the behaviour of this non-uniform array was also tested. The authors note a lack of impingement array data in open literature with streamwise pitch resolved results for dense arrays at the high Reynolds numbers seen in this study. Therefore, the streamwise pitch averaged results for case 2 are compared against the correlations from [14] and [15] even though the jet spacings at certain rows and Reynolds numbers may fall outside their prescribed bounds. Figure 7.10 shows this comparison at $Re_{j,1}=51,600$.

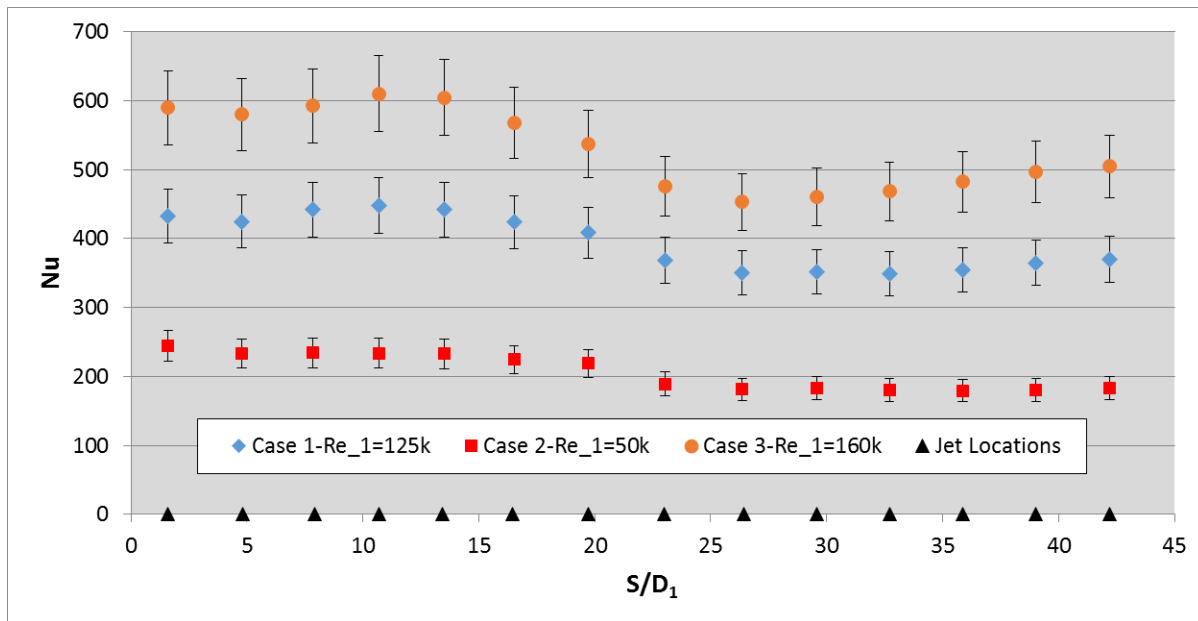


Figure 7.9: Row averaged Nusselt numbers for non-uniform array cases 1 to 3

The correlation from [14] shows agreement within uncertainty for the first 6 rows with near uniform spacings and a constant diameter, even though the X/D and Y/D fall outside of the correlations range. As noted by [12], [15] and other recent studies, the correlation from [14] over-predicts the first row heat transfer and then over-predicts the effect of crossflow in the successive rows. The comparison with [15] shows a first row error of 25% which decreases to 11% by the 6th row. This error can possibly be attributed to the $Y/D=2.6$ for these first 6 rows being below [15]s lower limit of $Y/D=3$. Downstream of the 6th row, the Z/D values in the channel exceed the limits for [14] and, as expected, this leads to erroneous predicted values from row 7 and on. Contrarily, the jet spacings from row 7-14 fall within the bounds for the correlation of [15], however the predicted Nu levels are still under-predicted by a minimum of 31%. This under-prediction is most likely an effect of the varying hole diameters disrupting the crossflow channels in the spanwise gaps between jets. Florschuetz and Tseng [5] also noted an inability of the correlation from [14] to correctly predict the heat transfer at the transition between varying jet spacings.

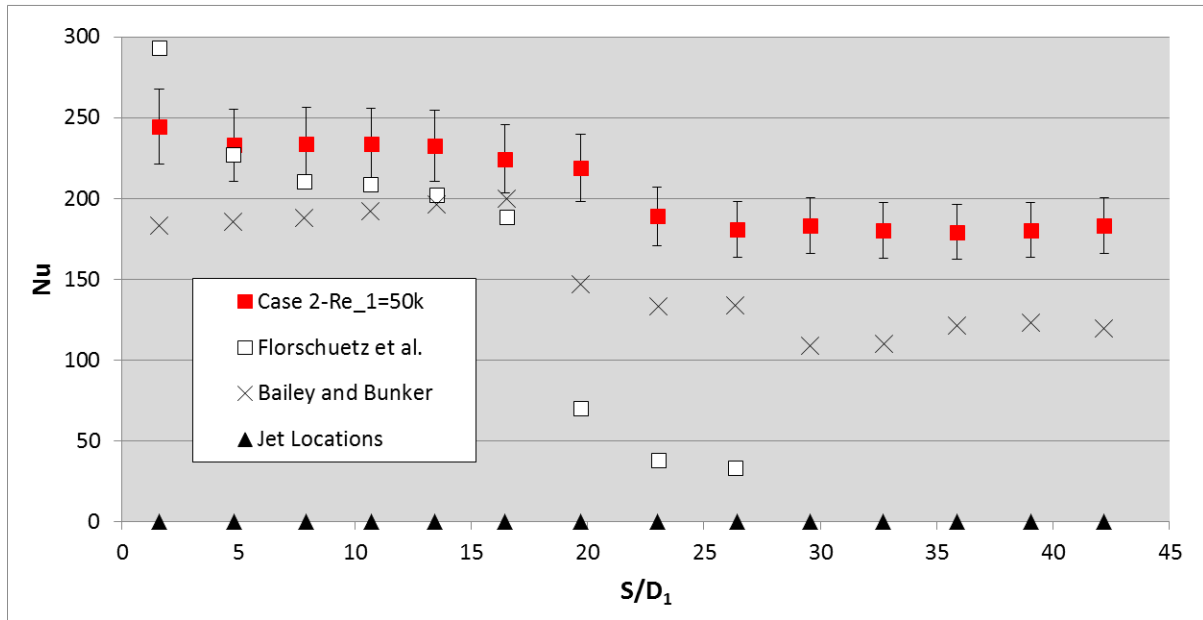


Figure 7.10: Row averaged Nusselt numbers comparison of case 2 with correlations from Florschuetz et al. and Bailey and Bunker

For case 3 at $Re_{j,1}=157,800$, although all local jet Reynolds numbers exceed the bounds for [14] and [15], it was of interest to note their predictions. This comparison is shown in Figure 17. Even though the jet Reynolds numbers are a factor of 3 higher than that designed for use with [14], the correlation is still able to predict the first six rows to within 30%. Downstream of row 6, the same non-physical results are seen as at the lower Reynolds numbers. The form of the correlation developed by [15] leads to severe under-prediction, as seen here, when extrapolating to Reynolds numbers which exceed the prescribed limits.

The actual Reynolds number sensitivity for the current work was evaluated at both the overall area averaged level as well as row-averaged level. Using the area average Nusselt number, a Reynolds number power coefficient of 0.822 was calculated, as shown in Figure 37. This value is slightly higher than the predicted values of 0.66 by Florschuetz et al. and 0.76 by Goldstein et al.

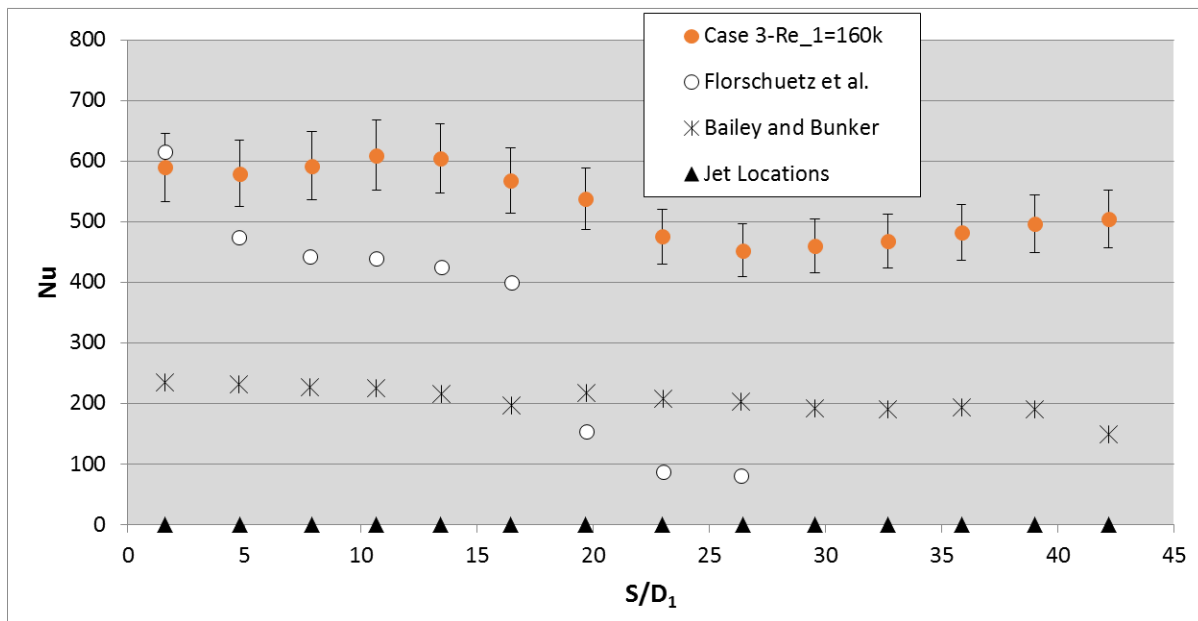


Figure 7.11: Row averaged Nusselt numbers comparison of case 3 with correlations from Florschuetz et al. and Bailey and Bunker

On a row-by-row basis, the m values are seen to vary from 0.75 at the first row to a maximum of 0.838 at row 13. As values of this power coefficient are predicted to be in the range 0.8 for wall-jets [5], the downstream rows show expected values. Note that these graphs are only meant to show the relative sensitivities of Nusselt number to Reynolds number. Although these graphs appear to show good agreement between the current data and the Florschuetz correlation, this is not necessarily the case as the correlation contains further variations based on streamwise location and amount of relative crossflow. These variations will tend to shift the given data line downwards, and away from the current test data.

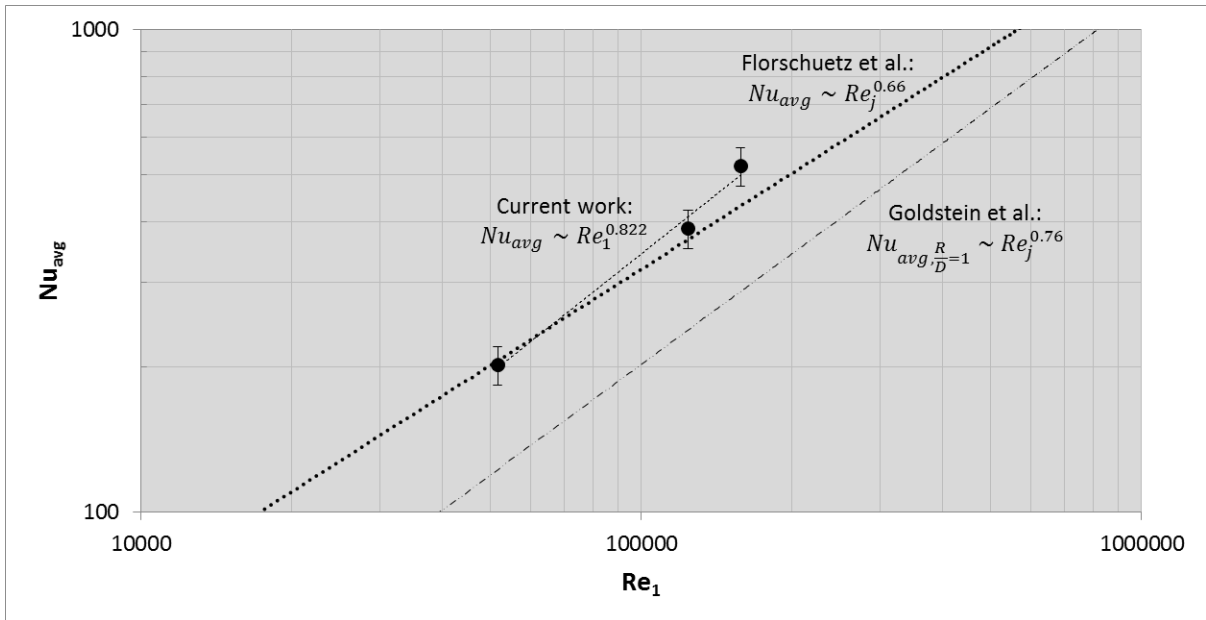


Figure 7.12: Reynolds number sensitivity of area averaged Nusselt number

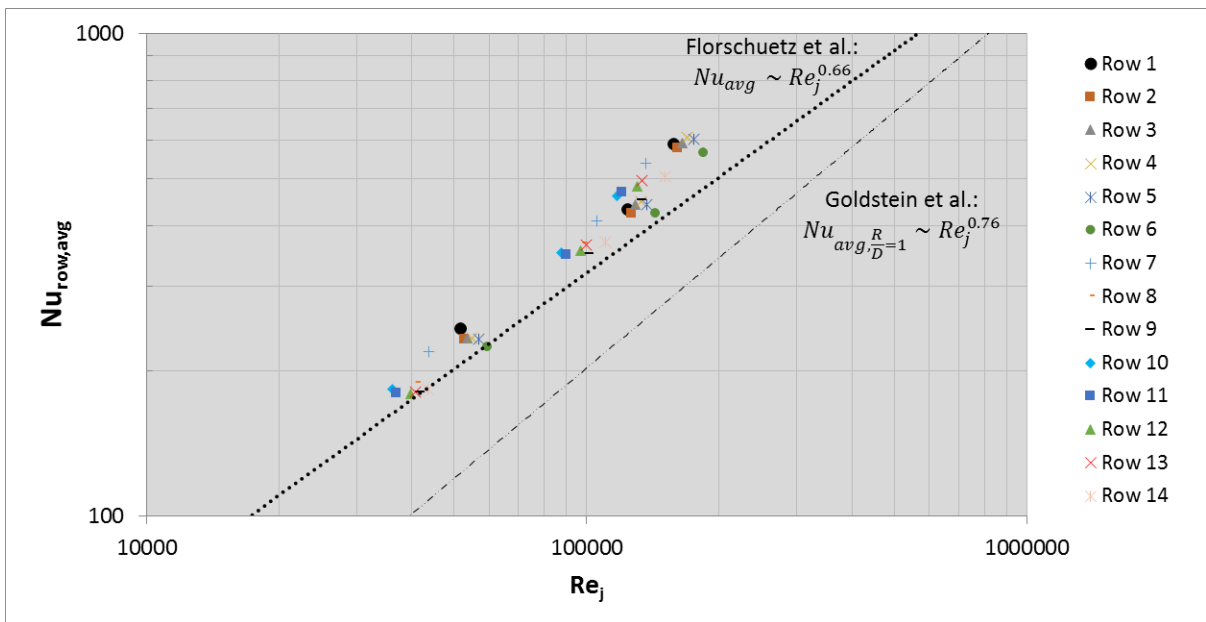


Figure 7.13: Reynolds number sensitivity of local row averaged Nusselt numbers

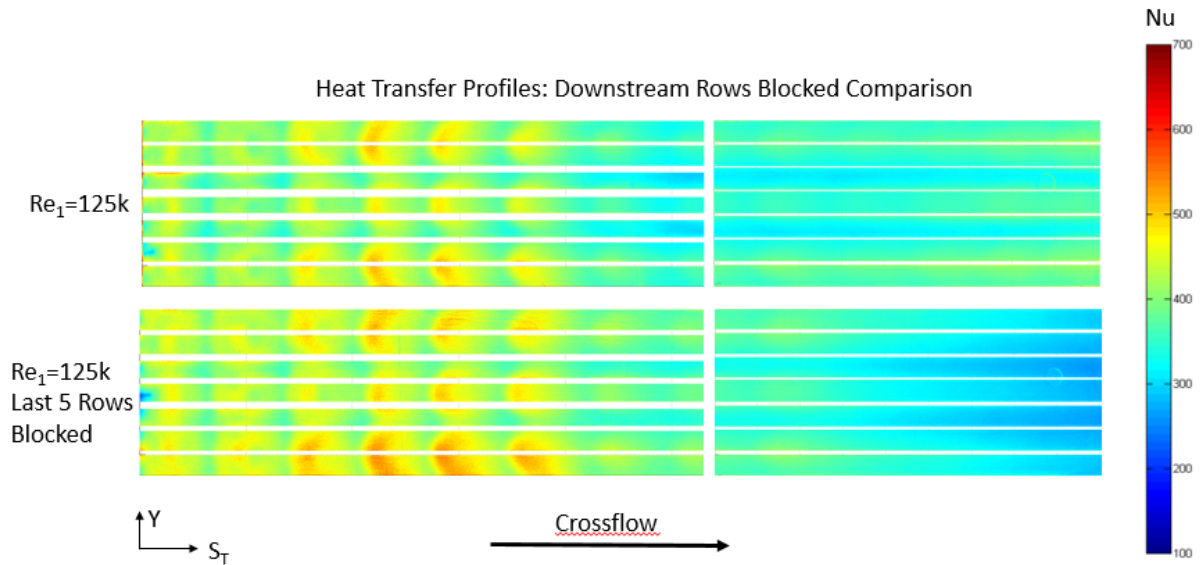


Figure 7.14: Nusselt number profiles for non-uniform array cases 1 and 4

The target wall Nusselt numbers for cases 1 and 4 are compared in Figure 7.14. These plots show how the profiles are similar where there are shared jet row locations (rows 1 to 9) with case 4 showing a steady decline in heat transfer, as expected, downstream of row 9, after which there are no more jets for case 4. These results reflect the pressure results shown in the previous section which showed matching pressure profiles, and thus flow rates, for the first 9 rows of case 1 and 4.

Figure 7.15 shows the local downstream distribution of Nusselt number contour for case 4, 5 and 6 at $Re = 125k$. With the presence of turbulators, the heat transfer is enhanced significantly compared to case 4. For the 90 degree rib (Rib 1, case 5) heat transfer is higher just downstream of the rib. This is caused by the thin boundary layer at the flow reattachment region downstream of the rib. For the W shaped ribs (Rib 2, case 6) higher heat transfer is observed just downstream of the rib tip. The vortices formed by the flow over the rib are strongest in this location and, after shedding off the rib, impinge onto the surface during reattachment and create a thin thermal boundary layer causing this region of high heat transfer.

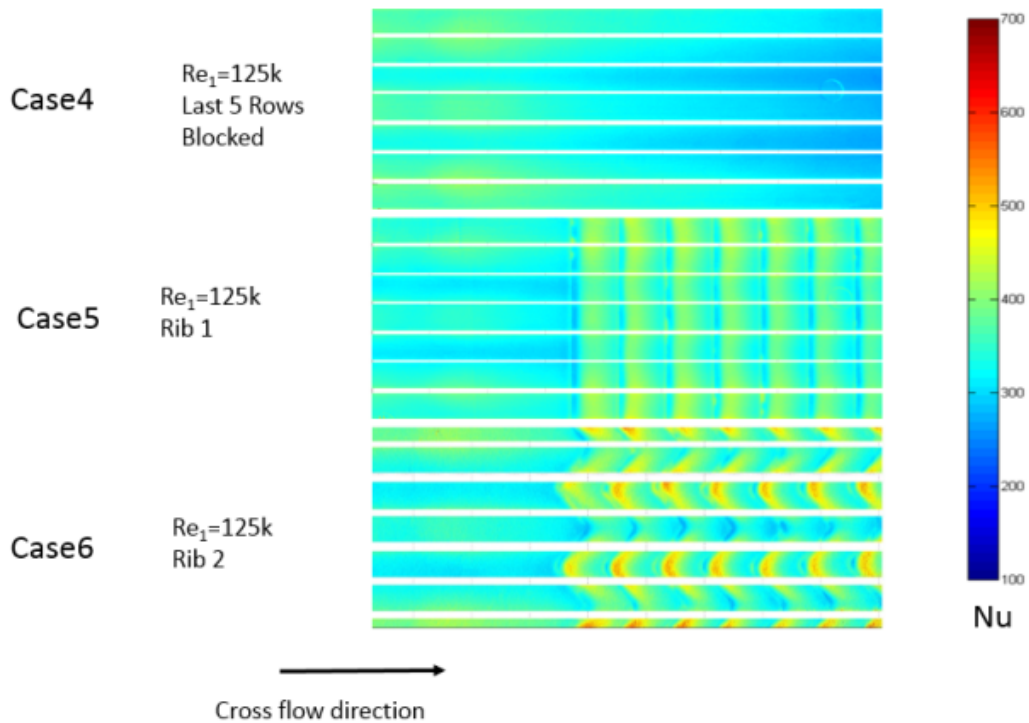


Figure 7.15: Downstream Nusselt number profiles for non-uniform array cases 4 to 6

For a more quantitative analysis of the performance of the ribs, the laterally averaged Nusselt numbers are plotted in Figure 7.16. The Nusselt number profiles for cases 1 and 4 to 6 were identical in the upstream regions and, for this reason, the graphs focus on the downstream regions. From this, it is seen that with the removal of the downstream rows, case 4 shows a drop of $\approx 25\%$ in heat transfer compared to case 1 by the exit of the channel. It should be noted that the difference in mass flow between case 1 and 4 is approximately 25% . This demonstrates the relatively low cooling efficiency of jet impingement arrays in high crossflow configurations. These graphs also show that both ribbed cases improve the heat transfer in the downstream close to a similar magnitude as in case 1, with Case 6 (W-Shaped ribs) showing slightly higher Nusselt number values. All cases are seen to have significantly higher Nu levels than that predicted by the Dittus-Boelter correlation.

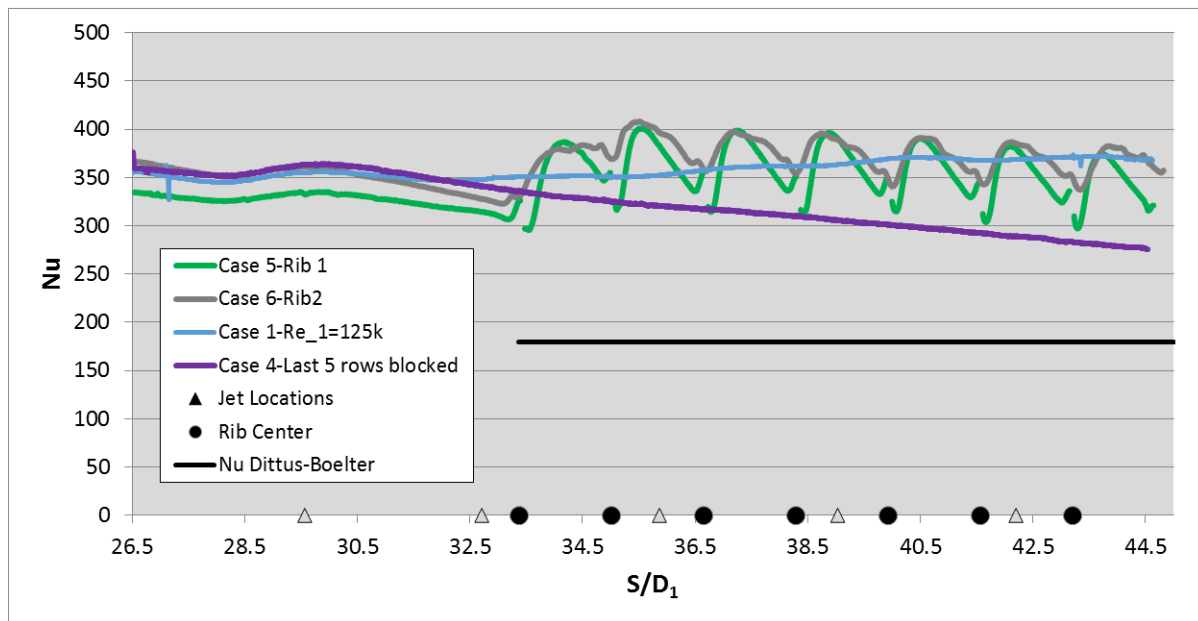


Figure 7.16: Downstream laterally averaged Nusselt numbers for non-uniform array cases 1 and 4 to 6

This is expected as the flow is highly turbulent, and in the developing region just downstream of the jets.

Rib pitch averaged Nusselt number values are provided in Figure 7.17. These plots clearly show the heat transfer enhancement from the addition of ribs onto the surface. Case 5 (90 degree ribs) gives an improvement in Nu of 18% over case 4, while Case 6 shows an improvement of 27%. By comparing these values with the friction factor values in the previous section, which show that case 6 has a 24% lower friction factor than case 5, it is clear that the W-shaped ribs of case 6 are the best option for high efficiency cooling.

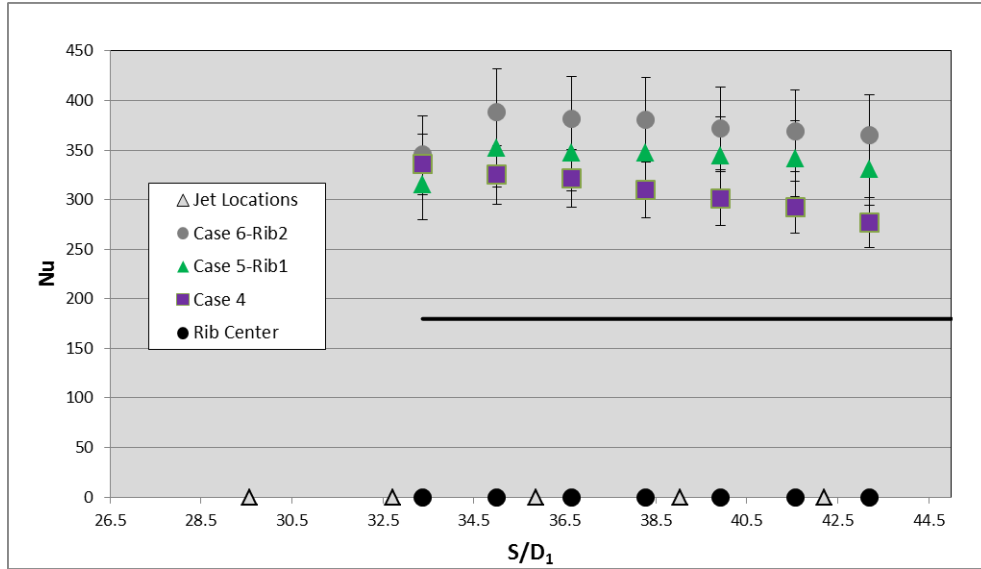


Figure 7.17: Downstream rib pitch averaged Nusselt numbers for non-uniform array cases 4 to 6

Computational Results

As with the uniform array, a computational model of the domain was run alongside the experimental tests for cases 1 to 3. The laterally averaged Nusselt number values are plotted and compared with the experimental values in 7.18. It can be seen that the CFD consistently over-predicts the stagnation Nusselt number values. This has been seen in many other past studies, most notably it is mentioned by Zuckerman and Lior [20]. It is also evident that, by approximately the 5th jet row, the CFD severely under-predicts the downstream deflection of the jets caused by the crossflow. Additionally, the CFD does not show the trend of increasing Nusselt numbers at the downstream end of the channel as the experiment does.

The computational results were further reduced to row averaged Nu values and are presented in 7.19. Eventhough the laterally averaged values showed some discrepancies between the CFD and experimental results, the row averaged values show much better agreement.

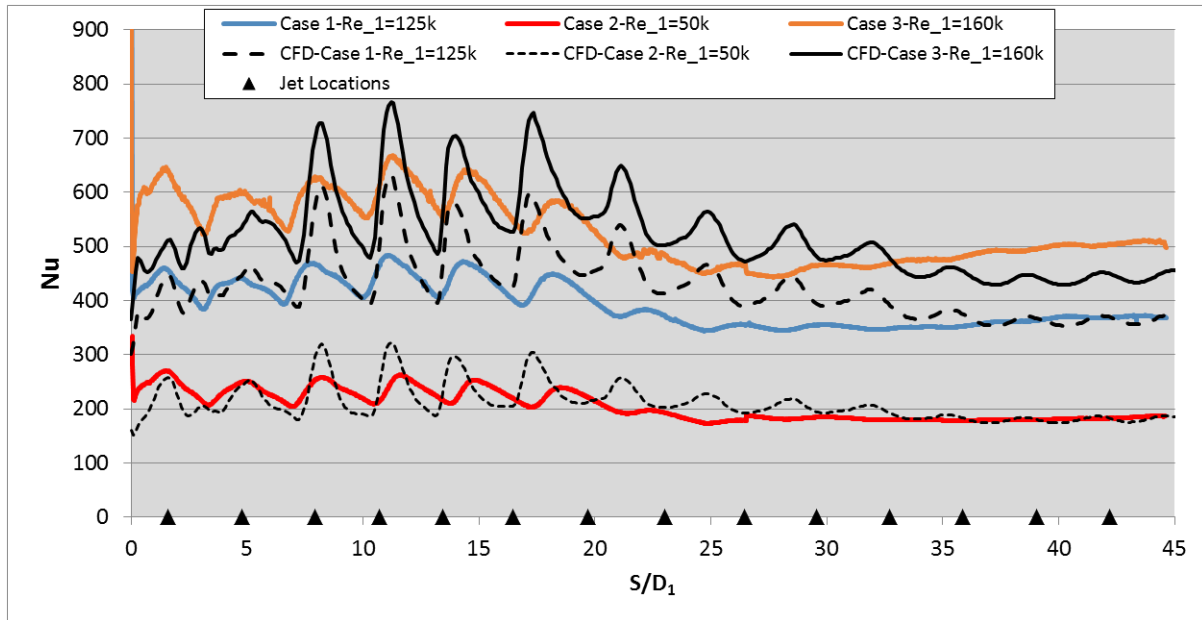


Figure 7.18: Laterally averaged Nusselt numbers comparison with CFD for non-uniform array cases 1 to 3

The maximum error is found at the first row, with approximately 20% error, however most error values fall within 10% of the experimental values. This shows that CFD can be used as an initial design tool for impingement array heat transfer calculations.

The discrepancies in the effect of crossflow seen between the CFD and experimental results led to further investigation into the flow distribution predicted by the CFD. The relevant flow parameter was determined to be the local crossflow to jet mass flux ratio, and is plotted as a comparison between experimental and computational values for case 1 in Figure 7.20. The local mass fluxes were directly measured in the CFD using planes which cut through the channel and jet orifice cross sections. These results correlate with what is seen in the Nusselt number plots. Relative to the experiment, the CFD predicts lower crossflow levels, with more pronounced differences in the downstream region. This implies that the CFD over-predicts jet flow rates in the downstream regions and under-predicts jet flow rates in the upstream region relative to the experiment.

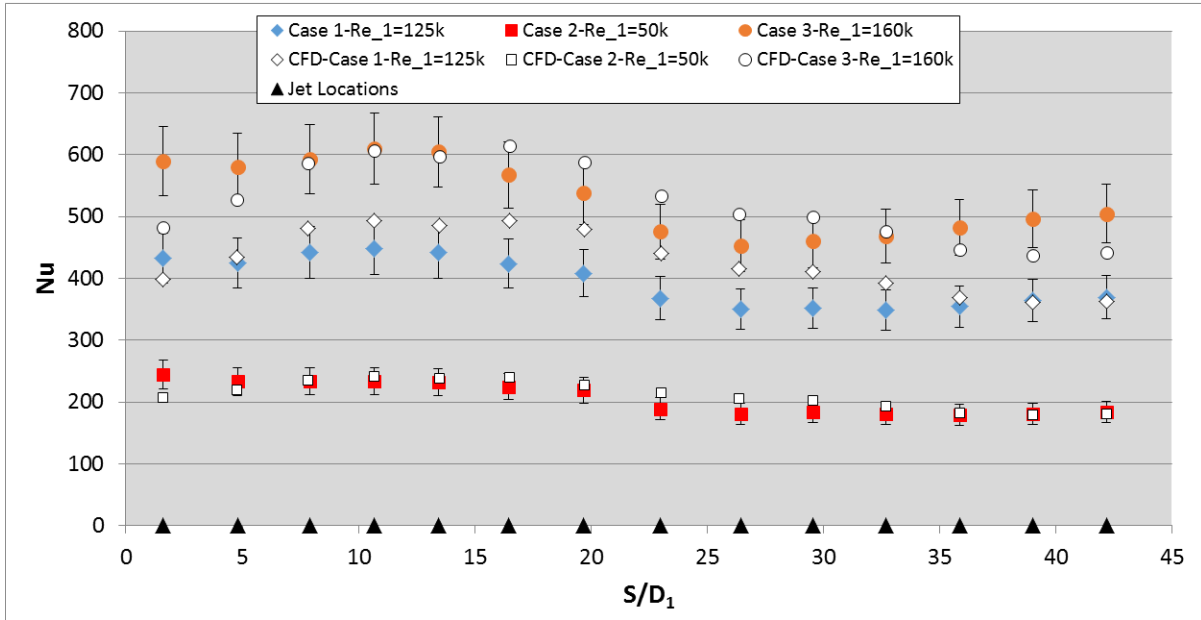


Figure 7.19: Row averaged Nusselt numbers comparison with CFD for non-uniform array cases 1 to 3

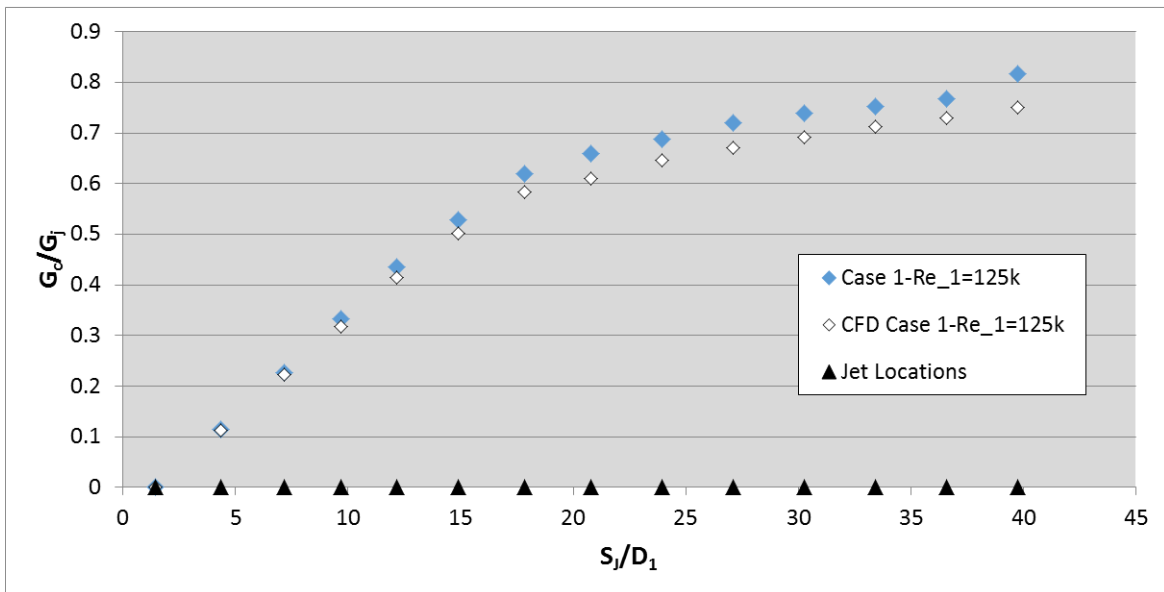


Figure 7.20: Local crossflow to jet mass flux ratio comparison between experiment and CFD for case 1

CHAPTER 8: CONCLUSION

The current work analyzed the heat transfer and pressure characteristics of two different jet impingement arrays. The first geometry consisted of a six by six array of jets with constant jet diameters and spacings. Average jet Reynolds numbers were in the range of 50,000 to 125,000. The second geometry consisted of 14 rows of jets with varying diameters and spacings. First row Reynolds numbers from 50,000 to 160,000 were tested for the non-uniform case. Both geometries impinged onto a large radius curved plate. For the non-uniform case, the effect of the removal of downstream rows was tested along with the addition of ribs onto the target surface. Several conclusions can be drawn from the observed results.

- The effect of the large radius curvature on the heat transfer and flow characteristics of the uniform array was shown to be negligible, as measured flow distributions and Nusselt number values were found to be nearly identical to that of a similar flat plate array.
- Results for the non-uniform array illustrate the applicability of tuning a jet impingement array using varying jet diameters and spacing.
- Established correlations for streamwise pitch resolved heat transfer predictions are unable to predict the heat transfer behavior for an array with varying diameters and/or spacings.
- For situations where efficient use of mass flow for cooling is priority, it has been shown that pressure drop and cooling mass flow can be reduced while maintaining high heat transfer levels by replacing downstream rows of jets with small e/H ribs. W-shaped ribs show better performance than 90 degree ribs in both heat transfer and pressure drop characteristics.
- Computational results from this study show that simulations can be used to obtain initial predictions, with streamwise pitch averaged Nu values found to be within 20% of experimental results.

LIST OF REFERENCES

- [1] J. Lee and S.-J. Lee, “The effect of nozzle configuration on stagnation region heat transfer enhancement of axisymmetric jet impingement,” *Int. J. Heat Mass Transfer*, vol. 43, pp. 3497–3509, 2000.
- [2] N. T. Obot and T. A. Trabold, “Impingement heat transfer within arrays of circular jets: Part 1-effects of minimum, intermediate, and complete crossflow for small and large spacings,” *Journal of Heat Transfer*, vol. 109, no. 4, pp. 872–879, 1987.
- [3] U. E. I. Administration, “Annual energy review,” DOE/EIA-0384(2011), 2012.
- [4] J. C. Han and S. E. S. Dutta, *Gas Turbine Heat Transfer and Cooling Technology*. Taylor and Francis, Inc.
- [5] R. J. Goldstein, A. I. Behbahani, and K. K. Heppelmann, “Streamwise distribution of the recovery factor and the local heat transfer coefficient to an impinging circular air jet,” *Int. J. Heat Mass Transfer*, vol. 29, no. 8, pp. 1227–1235, 1986.
- [6] R. J. Goldstein and J. F. Timmers, “Visualization of heat transfer from arrays of impinging jets,” *Int. J. Heat Mass Transfer*, vol. 25, no. 12, pp. 1857–1868, 1982.
- [7] J. W. Baughn and S. Shimizu, “Heat transfer measurements from a surface with uniform heat flux and an impinging jet,” *Journal of Heat Transfer*, vol. 111, no. 12, pp. 1096–1098, 1989.
- [8] N. T. Obot, A. S. Majumdar, and W. J. M. Douglas, “The effect of nozzle geometry on impingement heat transfer under a round turbulent jet,” *ASME Winter Annual Meeting: Heat Transfer*, 1979.

- [9] Y. Pan, J. Stevens, and B. W. Webb, "Effect of nozzle configuration on transport in the stagnation zone of axisymmetric, impinging free-surface liquid jets: Part 2-local heat transfer," *Journal of Heat Transfer*, vol. 114, no. 4, pp. 880–886, 1992.
- [10] K. Oyakawa, T. Azama, I. Senaha, and M. Hiwada, "Effects of nozzle configuration on impingement heat transfer," *Proceedings of ASME/JSME Thermal Engineering Conference*, pp. 377–384, 1995.
- [11] D. M. Kercher and W. Tabakoff, "Heat transfer by a square array of round air jets impinging perpendicular to a flat surface including the effect of spent air," *Journal of Engineering for Power*, vol. 92, no. 1, pp. 73–82, 1970.
- [12] D. E. Metzger, L. W. Florschuetz, D. I. Takeuchi, R. D. Behee, and R. A. Berry, "Heat transfer characteristics for inline and staggered arrays of circular jets with crossflow of spent air," *Journal of Heat Transfer*, vol. 101, no. 3, pp. 526–531, 1979.
- [13] L. W. Florschuetz, D. E. Metzger, D. I. Takeuchi, and R. A. Berry NASA Contractor Report 3217, January 1980.
- [14] L. W. Florschuetz, D. E. Metzger, and C. R. Truman NASA Contractor Report 3373, January 1981.
- [15] J. C. Bailey and R. S. Bunker, "Local heat transfer and flow distributions for impinging jet arrays of dense and sparse extent," *Proceedings of ASME Turbo Expo 2002*. ASME Paper No. GT2002-30473.
- [16] J. Park, M. Goodro, P. Ligrani, M. Fox, and H.-K. Moon, "Separate effects of mach number and reynolds number on jet array impingement heat transfer," *Journal of Turbomachinery*, vol. 129, pp. 269–280, 2007.

- [17] M. Goodro, J. Park, P. Ligrani, M. Fox, and H.-K. Moon, "Effects of mach number and reynolds number on jet array impingement heat transfer," *Int. J. Heat Mass Transfer*, vol. 50, pp. 367–380, 2007.
- [18] L. A. El-Gabry and D. A. Kaminski, "Numerical investigation of jet impingement with crossflow-comparison of yang-shih and standard k-epsilon turbulence models," *Numerical Heat Transfer*, vol. 47, pp. 441–469, 2005.
- [19] K. S. Mushatat, "Analysis of the turbulent flow and heat transfer of the impingement cooling in a channel with crossflow," *Journal of King Abdulaziz University*, vol. 8, no. 2, pp. 101–122, 2007.
- [20] N. Zuckerman and N. Lior, "Impingement heat transfer: Correlations and numerical modeling," *Journal of Heat Transfer*, vol. 127, pp. 544–552, 2005.
- [21] R. J. Jefferson-Loveday and P. G. Tucker, "Wall-resolved les and zonal les of round jet impingement heat transfer on a flat plate," *Numerical Heat Transfer*, vol. 59, pp. 190–208, 2011.
- [22] D. E. Metzger, T. Yamashita, and C. W. Jenkins, "Impingement cooling of concave surfaces with lines of circular air jets," *Journal of Engineering for Power*, vol. 91, no. 3, pp. 149–155, 1969.
- [23] R. S. Bunker and D. E. Metzger, "Local heat transfer in internally cooled turbine airfoil leading edge regions: Part i-impingement cooling without film coolant extraction," *Journal of Turbomachinery*, vol. 112, no. 3, pp. 451–458, 1990.
- [24] D. E. Metzger and R. S. Bunker, "Local heat transfer in internally cooled turbine airfoil leading edge regions: Part ii-impingement cooling with film coolant extraction," *Journal of Turbomachinery*, vol. 112, no. 3, pp. 459–466, 1990.

- [25] M. E. Taslim, L. Setayeshgar, and S. D. Spring, "An experimental evaluation of advanced leading edge impingement cooling concepts," *Journal of Turbomachinery*, vol. 123, no. 1, pp. 147–153, 2001.
- [26] M. E. Taslim, K. Bakhtari, and H. Liu, "Experimental and numerical investigation of impingement on a rib-roughened leading-edge wall," *Journal of Turbomachinery*, vol. 125, no. 5, pp. 682–691, 2003.
- [27] M. E. Taslim and D. Bethka, "Experimental and numerical impingement heat transfer in an airfoil leading-edge cooling channel with cross-flow," *Journal of Turbomachinery*, vol. 131, no. 1, pp. 1–7, 2009.
- [28] L. W. Florschuetz and H. H. Tseng, "Effect of nonuniform geometries on flow distributions and heat transfer characteristics for arrays of impinging jets," *Journal of Engineering for Gas Turbines and Power*, vol. 107, pp. 68–75, 1985.
- [29] L. Goa, S. V. Ekkad, and R. S. Bunker, "Impingement heat transfer, part i: Linearly stretched arrays of holes," *Journal of Thermophysics and Heat Transfer*, vol. 19, pp. 57–65, 2005.
- [30] R. Hebert, S. V. Ekkad, and R. S. Bunker, "Impingement heat transfer, part ii: Effect of streamwise pressure gradient," *Journal of Thermophysics and Heat Transfer*, vol. 19, pp. 66–71, 2005.
- [31] U. Uysal, P.-W. Li, M. K. Chyu, and F. J. Cunha, "Heat transfer on internal surfaces of a duct subjected to impingement of a jet array with varying jet hole-size and spacing," *Journal of Turbomachinery*, vol. 128, pp. 158–165, 2006.
- [32] E. I. Esposito, S. V. Ekkad, Y. Kim, and P. Dutta, "Novel jet impingement cooling geometry for combustor liner backside cooling," *Journal of Thermal Science and Engineering Applications*, vol. 128, pp. 1–8, 2006.

- [33] S. Mhetras, J. C. Han, and M. Huth, "Impingement heat transfer from jet arrays on turbulent target walls at large reynolds numbers," *Journal of Thermal Science and Engineering Applications*, vol. 6, pp. 1–10, 2014.
- [34] M. O. Annerfeldt, J. L. Persson, and T. Torisson, "Experimental investigation of impingement cooling with turbulators or surface enlarging elements," *Proceedings of ASME Turbo Expo 2001*. ASME Paper No. 2001-GT-0149.
- [35] C. Haiping, Z. Jingyu, and H. Taiping, "Experimental investigation on impingement heat transfer from rib roughened surface within arrays of circular jet: Effect of geometric parameters," *Proceedings of ASME Inter. Gas Turbine and Aeroengine Congress and Exhib.* ASME Paper No. 98-GT-208.
- [36] G. E. Andrews, R. A. A. Hussain, and M. C. Mkpadi, "Enhanced impingement heat transfer: The influence of impingement x/d for interrupted rib obstacles (rectangular pin fins)," *Journal of Turbomachinery*, vol. 129, pp. 321–331, 2006.
- [37] C. S. Woei, J. Y. Jena, and C. S. Fei, "Heat transfer of impinging jet-array over convex-dimpled surface," *Int. J. Heat Mass Transfer*, vol. 49, pp. 3045–3059, 2006.
- [38] R. Brakmann, L. Chen, B. Weigand, and M. Crawford, "Experimental and numerical heat transfer investigation of an impinging jet array on a target plate roughened by cubic micro pin fins," *Proceedings of ASME Turbo Expo 2015*. ASME Paper No. GT2015-42149.
- [39] W. S. Saric, "G"
- [40] J. M. Floryan, "On the g"
- [41] H. P. Wang, S. J. Olson, and R. J. Goldstein, "Development of taylor-g"
- [42] The American Society of Mechanical Engineers, ASME PTC 19.5 Flow Measurement Performance Test Codes, New York, NY: The American Society of Mechanical Engineers, 2004.

[43] R. S. Figliola and D. E. Beasley, *Theory and Design for Mechanical Measurements*. John Wiley and Sons, Inc.